Multimodal imaging and analysis of laryngeal structure and vocal fold injury

Ksenia Kolosova

Master of Science

Department of Physics

McGill University

Montréal, Québec

July 20, 2019

A thesis submitted to McGill University in partial fulfillment of the requirements of the degree of Master of Science, Physics.

ACKNOWLEDGEMENTS

I would first of all like to thank Paul W. Wiseman and Luc Mongeau for their supervision, mentorship, and patience. I have learned an incredible amount from them both throughout my projects. In addition, I have had the privilege of learning from the many people I have worked with and sought guidance from: Nicolas Audet, Sarah Aufmkolk, Taylor Bell, Sarah Bouhabel, Zixiong Cao, Robert Gagnon, Qiman Gao, Melina Jaramillo Garcia, Harrisonn Griffin, Alexei Kazarine, Nicole Y. K. Li-Jessen, Geoffroy Noel, Stephen Nuara, Nicolas Piché, Benjamin Provencher, David Rudko, Lihong Shang, Karen Hope Stone, Rui Tahara, Marius Tuznik, Huijie Wang, and Jonathan Young. I would like to thank them all for answering my unending questions and generously sharing their time and expertise. I am grateful to the Wiseman, Andrews, and Mongeau research groups for providing a productive workspace, support, and friendship. I would also like to thank Janice, Taylor, and my family, especially my mother and sister, for their unconditional support and understanding. This work was supported in part by the National Institute for Deafness and other Communication Disorders of the National Institutes of Health under award number R01DC005788, the Natural Sciences and Engineering Research Council, and the Canadian Foundation for Innovation.

ABSTRACT

Vocal communication is an important aspect of daily life for most people, and for many is required for their occupation. Conditions affecting the vocal folds, including scarring and other pathologies, may result in dysphonia and impair quality of life. When developing therapies, it is crucial to access detailed information about the tissue structure of the human larynx and of any animal models used to investigate treatments. This thesis details progress toward developing anatomical atlases and three-dimensional computer models of human and laboratory animal larynges from ex vivo microcomputed tomography images with image segmentation. Then, it describes the sequential application of magnetic resonance imaging, microcomputed tomography, and nonlinear microscopy with image analysis to a rabbit model study probing vocal fold scarring following surgery. This study proposes an imaging–analysis pipeline for animal studies involving vocal fold injury. Finally, it ties together information gleaned from these studies and outlines future directions motivated by their results.

ABRÉGÉ

La communication vocale est un outil important dans la vie quotidienne. Elle est nécessaire dans certains métiers tels que l'enseignement, ou les arts de la scène. Les affections des cordes vocales telles que les cicatrices peuvent entraîner la dysphonie et nuire à la qualité de vie. En vue du développement de thérapies efficaces, il est important de pouvoir accéder aux informations détaillées sur la structure tissulaire du larynx humain et du larynx des modèles animaux utilisés pour les études de traitements potentiels. Cette thèse détaille les progrès réalisés dans le développement des modèles anatomiques du larynx humain et du larynx des animaux de laboratoire créées à partir d'images de microtomographie aux rayons X. Elle décrit ensuite l'application séquentielle de l'imagerie par résonance magnétique, de la microtomographie aux rayons X, de la microscopie non-linéaire, et de l'analyse d'images à une étude sur les lapins portant sur la cicatrization des cordes vocales suite à une intervention chirurgicale.

TABLE OF CONTENTS

ACKNOWLEDGEMENTS ii

ABSTRACT iii

ABRÉGÉ iv

LIST OF TABLES vii

LIST OF FIGURES viii

KEY TO ABBREVIATIONS xiii

1 Introduction 1

1.1 Motivation 1
1.2 Thesis objectives 3
1.3 Thesis roadmap 3
1.4 Contributions 5

2 Background 7

2.1 The larynx 7
2.1.1 Larynx anatomy and physiology 8
2.1.2 Vocal fold microanatomy 10
2.1.3 Vocal fold wound healing and scarring 12
2.1.4 Animal studies 14
2.2 Imaging 16
2.2.1 Two-dimensional histology 17
2.2.2 Computed tomography 19
2.2.3 Magnetic resonance imaging 21
2.2.4 Ultrasound 25
2.2.5 Nonlinear microscopy 25
2.2.6 Endoscopy 29
2.3 Analysis 30
2.3.1 Image registration 30
2.3.2 Three-dimensional computer models from biological images 32
2.3.3 Quantitative fiber analysis 35

3 Materials and Methods 39

3.1 Ex vivo tissue acquisition 39

3.2 Animal study methods . . . 39
3.2.1 Injury timepoint study . . . 39
3.2.2 Treatment study . . . 40
3.3 Computed tomography (CT) . . . 40
3.3.1 CT sample preparation . . . 40
3.4 Magnetic resonance imaging (MRI) . . . 41
3.4.1 MRI sample preparation . . . 41
3.5 Nonlinear microscopy (NM) . . . 42
3.5.1 NM sample preparation . . . 44
3.6 Image analysis . . . 44
3.6.1 Image registration . . . 45
3.6.2 Segmentation . . . 45
3.6.3 3D printing . . . 46
3.6.4 Fiber analysis . . . 46

4 Creating models of laryngeal anatomy . . . 49

4.1 Imaging results . . . 49
4.1.1 Staining results . . . 49
4.1.2 Species anatomy results . . . 50
4.2 Model results . . . 51

5 Visualizing vocal fold injury in a rabbit model . . . 54

5.1 Past rabbit studies . . . 54
5.2 Imaging results . . . 59
5.2.1 Preliminary NM and CT results . . . 59
5.2.2 Injury timepoint study MRI and CT results . . . 63
5.2.3 MRI image processing . . . 66
5.2.4 Injury timepoint study NM results . . . 67
5.2.5 Quantitative fiber analysis . . . 70

6 Discussion . . . 75

6.1 Recommendations for future work . . . 78

References . . . 82

LIST OF TABLES

Table page

3–1 CT scan parameters 41

5–1 Vocal fold scarring studies, 2002-2019 56

6–1 Imaging methods comparison 78

LIST OF FIGURES

Figure page

2–1 (a) A diagram demonstrating the location of the larynx within the neck. Public domain image by Alan Hoofring, National Cancer Institute. (b) The external anatomy of the larynx. Illustration by Olek Remesz, reproduced under the Creative Commons Attribution - Share Alike 2.5 License. 7

2–2 Sagittal (left) and coronal (right) views of the larynx, identifying the hyoid bone, cartilages, and connective tissues. Reproduced from `https://www.enteducationswansea.org/`, with permission from Simon Browning. . . . 9

2–3 Elastin, collagen, and hyaluronic acid (HA) distribution in human vocal folds. Reproduced from [1], with permission from Elsevier. 10

2–4 The phases of the wound healing process, and their approximate timeline. Reproduced from [2], with permission from Elsevier. 13

2–5 Hematoxylin and eosin (H&E) stained images of canine vocal folds. The epithelium, muscle, and connective tissue structures are identifiable with this stain, as well as their changes in abnormal states. (a) shows normal vocal fold, (b) shows an injured vocal fold treated with transplanted tissue engineered vocal fold mucosa, and (c) shows an injured vocal fold with no treatment applied. The injury performed was a type II cordectomy. Reproduced from [3], under the Creative Commons Attribution 4.0 License. 17

2–6 The components of a micro-CT scanner for ex vivo samples. A source emits x-rays which are attenuated by their interactions with the specimen on the stage. The mechanical stage rotates, and images are acquired at many rotation angles for later reconstruction. The attenuated x-rays interact with a scintillation layer for conversion of the signal to visible light. A microscope objective then magnifies the image, and the signal is detected on a charge-coupled device (CCD) detector array. The type of scanner shown is a cone-beam CT scanner. Reproduced from [4], under the Creative Commons Attribution 3.0 License. 20

2–7 The pulse diagram for a RARE sequence with an echo train length of three. The initial excitation RF pulse is followed by three refocusing pulses. Three different phase encoding gradients are used, allowing readout of three lines in one iteration of the pulse sequence. Reproduced from `http://xrayphysics.com/sequences.html`, with permission from Mark M. Hammer. 24

2–8 Jablonski diagrams illustrating the energy transitions encountered in nonlinear imaging, THG (third harmonic generation), SHG (second harmonic generation), and TPE (two-photon excitation). Other relaxation pathways are not shown. Reproduced from [5], with permission from The Company of Biologists, Ltd. 26

2–9 Rigid laryngoscopy and concurrent microsurgical manipulation in a rabbit experiment. A rigid laryngoscope is inserted through the mouth, and a flexible laryngoscope is inserted through the nose. Author's picture. 29

2–10 The U-Net architecture, often used for biological deep learning image processing. The architecture is a contracting network with max pooling followed by upsampling with up-convolution. The convolution layers use rectified linear unit (ReLU) activation. The conventional contracting layers consolidate contextual information into a tractable feature map, and the following expanding network layers augment precision by improving feature localization. Reproduced from [6], with permission from Springer Nature. . 33

3–1 Diagram of the microscopy and illumination setup for the nonlinear laser-scanning setups, (a) FV1200MPE with 780 nm illumination and (b) FVMPE-RS with 1040 nm illumination. 42

3–2 Microscopy setup showing aluminum-coated mirror slide, silicone spacer made from Dragon Skin 30 (Smooth-On), glass-bottom dish containing glycerol for objective immersion, and XLSLPN25XGMP objective with refractive index correction set to 1.49 to approximate between glycerol and BABB-D solution. 44

3–3 uDISCO optical clearing process, consisting of tissue dehydration followed by immersion in BABB-D clearing medium. Images taken with stereomicroscope. The small lines delineate 1 mm spacing. 45

3–4 Straight (left) and wavy (right) fiber simulation examples, with rotation angles randomly determined uniformly between 30-60 degrees. 47

4–1 Human larynges without (left) and with (right) PTA staining for CT contrast enhancement, from the H-F scan. Clockwise from top left: 3D, sagittal, coronal, transverse views. 50

4–2 Rat and guinea pig CT. The left image shows the rat larynx, from the Rat scan. The right image shows the guinea pig larynx, from the GP scan. Clockwise from top left for each set of images: 3D, coronal, transverse, sagittal views. 51

4–3 CT images of the rabbit larynx. The left image, from the R3 scan, is taken with the Vimago. The four middle images, from the R-CS scan, show clockwise from the top left: 3D, coronal, transverse, sagittal views. The two right images show a virtual slice through the vocal fold and the cartilage from the R39HR scan. 51

4–4 3D model creation with manual segmentation from the H-F scan. (a) Manually segmented cartilages, with segmentation shown in blue, from one example plane in the transverse view. The smoothed mesh is shown in white. (b) 3D rendering of smoothed mesh from the manually segmented cartilages. . 52

4–5 Automatic U-Net segmentation results for the rabbit larynx from the R-CS scan. (a) An example automatically segmented slice in the coronal plane. The soft tissue shows high error, while muscle and cartilage are largely recognized. (b) 3D rendering of the automatically segmented slice volumes, shown as smoothed meshes. 53

5–1 Common rabbit study protocols. Injury, treatment, and analysis methods as applied in rabbit studies of vocal fold scarring. 55

5–2 Sacrifice day distribution for rabbit vocal fold scarring studies, 2002-2019. For studies with more than one endpoint, all endpoints are considered separately. The timepoint axis is logarithmic. 57

5–3 3D imaging of rabbit vocal folds with CT and NM. (a) Dissected vocal folds before (left) and after (right) optical clearing. (b) 3D renderings of CT and NM imaging of the specimen shown above. (c) CT images of a rabbit larynx from a commercial source, clockwise from left showing a 3D view, coronal virtual slice, and transverse virtual slice. This scan was acquired at 12.4 µm resolution. The location of the vocal folds is shown with a green arrow in (c). 59

5–4 Coronal vocal fold slices from histology, NM, and CT. (a) H&E staining of a rabbit vocal fold, with lamina propria outlined in black. (b) Virtual slice from NM acquired at 640 nm (x,y) by 5 µm z resolution. Top image is sliced through vocal fold, bottom image sliced through cartilage. (c) CT at 800 nm voxel size. Left image represents vocal fold and right image represents cartilage. 61

5–5 Representative images of laryngeal tissue structures visualized with NM and CT. In the NM images, resolution down to 248 nm is attained in (x,y). In the CT images, resolution down to 800 nm is attained in (x,y,z). 62

5–6 Illustration of the function anatomy dissection structure. This rabbit was treated with dexamethasone, a corticosteroid. (a) Still from a high-speed video acquisition, courtesy of Lei Xi Christina Chen. (b) Transverse view. (c) 3D view. (d) Coronal view through vocal fold location. (e) Coronal view through the arytenoid cartilages. 63

5–7 MRI and CT of rabbits sacrificed at different timepoints. At day 3, inflammation was observed with MRI at the location of the deficiency. At day 10, the asymmetry of the vocal folds is visible with both MRI and CT. At day 39, the mature scar with increased density is seen with MRI. The scarred vocal fold has a triangular shape in the coronal view, compared to the rounded healthy vocal fold. The defect shape is visible in the excised larynx CT as well as the intact rabbit CT, though for the intact animal higher resolution scanning may be desired. 65

5–8 MRI image processing. (a) Image registration between the left and right vocal folds of the rabbit sacrificed at 39 days, with the healthy vocal fold shown in greyscale and the scarred vocal fold overlaid with the Fire lookup table. (b) A coronal view of the vocal folds. (c) 3D printed model. The segmented area was created by intensity thresholding followed by manual correction. The resulting mesh was then smoothed, converted to G-code, and printed with the Prusa i3 MK3 in PLA material. The scar defect can be seen in the shape of the left vocal fold. 66

5–9 Images of a human skin tissue control slide (Tissue-Trol, Sigma-Aldrich), without (left) and with (right) an aluminum-coated coverglass below the imaging location. The autofluorescence signal increased moderately by a factor of 1.1, while the SHG signal increased by a factor of 3.0. 67

5–10 Results from optical clearing for the rabbits sacrificed at 3, 10, and 39 days. The mucosa can be observed in the pre-clearing images, while in the post-clearing images is greatly retracted due to dehydration. The right image shows a stitched image at one height, above the true vocal folds, in a healthy rabbit larynx showing the distribution of tissues within the sample. 68

5–11 Features of interest in NM scans of the rabbit sacrificed at 39 days. The x,y pixel size was 994 nm, and then z pixel size was 50 µm. (a) Elastic cartilage structure of the arytenoid cartilage. (b) Hyaline cartilage structure of the thyroid cartilage. (c) Fat tissue. Planar outfoldings in the right (d) and left (e) vocal folds. Gland tissue located above the right (f) and left (g) vocal folds. (h) Transverse view of the vocal folds, right then left clockwise. There is a potential scar location seen in the injured vocal fold, with signs of collagen disorganization and tissue contraction. 69

5–12 Spatial image correlation spectroscopy analysis demonstrated on simulated line and wave images with orientation uniformly distributed between 120-150 degrees, and a real image of tissue from the media layer of the aorta. The aortic tissue sample is shown courtesy of Meisam Asgari. The autocorrelation function was cropped and fit with a 2D elliptical Gaussian function. The 3D plot shows the fitting of the cropped image autocorrelation function (surface) with the Gaussian (points). 71

5–13 Fourier power spectral analysis demonstrated on simulated line and wave images, and a real image of tissue from the media layer of the aorta. The power spectral density (PSD) of the image was taken and cropped circularly at the center. The orientation distribution histograms shown are median-subtracted for improved visualization. The images processed with Otsu thresholding provide an estimate of fiber density. 72

5–14 CT-FIRE analysis demonstrated on simulated line and wave images, and a real image of tissue from the media layer of the aorta. The images of fibers, and the fibers as found by CT-FIRE, are shown. Histograms summarize the distribution of length, width, straightness, and angle for the extracted fibers. The average value of each of those parameters is also shown. 73

KEY TO ABBREVIATIONS

2D: two-dimensional

3D: three-dimensional

BABB-D: benzyl alcohol, benzyl benzoate, diphenyl ether

CCD: charge-coupled device

CNN: convolutional neural network

CT: computed tomography

CT-FIRE: curvelet transform – fiber extraction

DFT: discrete Fourier transform

DM: dichroic mirror

ECM: extracellular matrix

EtOH: ethanol

FFT: fast Fourier transform

FSE: fast spin echo

GRE: gradient echo

H&E: hematoxylin and eosin

HA: hyaluronic acid

ICS: image correlation spectroscopy

IHC: immunohistochemistry

IR: infrared

MRI: magnetic resonance imaging

mRNA: messenger ribonucleic acid

NA: numerical aperture

NADH: reduced nicotinamide adenine dinucleotide

NDD: non-descanned detector

NM: nonlinear microscopy

OCT: optical coherence tomography

PBS: phosphate-buffered saline

PCR: polymerase chain reaction

PEG: polyethylene glycol

PLA: polylactic acid

PMT: photomultiplier tube

PTA: phosphotungstic acid

PSD: power spectral density

PSF: point spread function

RARE: rapid imaging with refocused echoes

ReLU: rectified linear unit

RF: radiofrequency

ROI: region of interest

SE: spin echo

SHG: second harmonic generation

T1: spin-lattice relaxation

T2: spin-spin relaxation

TE: echo time

THG: third harmonic generation

TPE: two-photon excitation

TR: repetition time

uDISCO: ultimate imaging of solvent-cleared organs

WD: working distance

WF: wave fitting

CHAPTER 1
Introduction

1.1 Motivation

Vocal communication is an important part of daily and occupational life for most people. Pathologies that affect normal vocal function often result in dysphonia of varying severity and impair patients' quality of life [7]. Voice disorders affect approximately 10% of the general population [8]. People in certain occupations, such as teachers and singers, are at heightened risk for voice problems [9, 10]; in fact, the incidence of voice disorders rises to 50% in voice professionals [8]. Many voice disorders arise from changes at the tissue level of the vocal folds, which are soft tissue structures that act as the voice source in phonation by modulating air flowing from the lungs. Healthy vocal folds make efficient use of the energy available for voice production, provided by the muscles contracting the rib cage and lungs, in their vibration. Neoplastic lesions on the vocal folds form a significant group of disorders; this group includes malignant tumours, but benign lesions like nodules and polyps are much more common [11]. Another type of disorder results from scarring of the vocal folds. A scar may form following any disruption of the vocal fold tissue structure, and causes include surgical lesion excision and phonotrauma [12, 13]. A large inflammatory response to such a traumatic event may lead to an incomplete wound healing response with insufficient extracellular matrix remodeling [14]. This results in the formation of scar tissue, which has different histological features and mechanical properties than the original tissue, and consequently impairs normal vocal fold vibration.

Treatment of vocal fold injury and management of vocal fold scars remain active areas of research. There is currently no consensus on an optimal prophylactic treatment to apply following phonosurgery or vocal fold injury to prevent scar formation; neither is there a treatment considered highly effective for dissolving scars formed on the vocal folds [15]. Many

research groups around the world are testing potential treatments for vocal fold scarring at the preclinical stage. Following demonstrated safety and efficacy at the in vitro 2D or 3D cell culture stage, treatments are tested in animal models.

The differences between animal and human laryngeal anatomy and function can have a considerable impact on the utility of animal studies, as laboratory animals may exhibit a different response to injury and treatment than humans [16, 17]. Imaging can be used to gain insight into laryngeal anatomy and function, down to the specifics of vocal fold microstructure, in different species. Results from imaging studies can contribute to a clearer understanding of the limitations of each animal model, in addition to finding their niche of utility in preclinical research. This information can be used to select the most appropriate animal model available on a case-by-case basis. In current animal studies of vocal fold scarring, imaging is usually conducted with two-dimensional (2D), optical microscopy based planar histology following microtome slicing. Virtual histology methods, including (micro/nano)computed tomography (CT), magnetic resonance imaging (MRI), and microscopy image stacks, allow information to be extracted from any 2D plane of interest in intact tissue [18]. The three-dimensional (3D), volumetric information acquired from such modalities can also be used to create realistic computer models of anatomical structure for use in biomechanical simulation. Nonlinear microscopy (NM) is a desirable method for studies of vocal fold scarring as it directly visualizes second harmonic generation (SHG) emitted light from fibrillar collagen and intrinsic autofluorescence from elastin fibers [19], two important players in wound healing whose distribution and organization facilitate diagnosis of scar formation and severity [20]. The SHG imaging method however necessitates long scan times and requires small specimen sizes due to a penetration depth limitation for the excitation laser. This motivates the use of lower-resolution, faster scanning approaches that accommodate larger specimens including MRI and CT for acquisition of first-pass images. These can reveal larger-scale patterns, serve as platforms for 3D computer model creation, and inform targeted dissection of samples for NM.

1.2 Thesis objectives

This thesis works toward obtaining and processing CT images of human and animal larynges for interspecies anatomical comparison and creation of computer models. It also aims to evaluate MRI, CT, NM, and accompanying image analysis techniques as virtual histology methods for application to a rabbit vocal fold scarring study.

1.3 Thesis roadmap

The thesis begins with background information and literature review, presented in Chapter 2. Section 2.1 introduces relevant anatomy and physiological functioning of the larynx, from the gross anatomy of muscles and cartilages down to the microstructure of the vocal folds. It describes anatomical and functional implications of laryngeal pathologies, with a focus on vocal fold scarring and therapies for its treatment and prevention currently in clinical use and preclinical development. Next, Section 2.2 gives a technical background on biological imaging, outlining common modalities used in laryngology studies. It goes further in depth for the imaging modalities used in this work, namely microcomputed tomography, magnetic resonance imaging, and nonlinear microscopy. Section 2.3 surveys image analysis methods applied to the imaging modalities used in this work, ranging from image segmentation to the analysis of vocal fold extracellular matrix fibrous microstructure. It also introduces biomechanical simulation, 3D bioprinting, and microsurgical intervention planning as potential uses for data acquired in this work. By placing the imaging and analysis approaches in the wider context of preclinical and clinical laryngology, this chapter motivates the methodology decisions made in the research work.

Chapter 3 describes the sample preparation, imaging, and image analysis methods used in the research studies. Following a description of sample acquisition and animal study methods, Section 3.3 details setup and sample preparation for the three CT systems used. Section 3.4 details the MRI sample preparation and scanning parameters. Section 3.5 then describes the NM systems used for fine-detail visualization of fibers in the extracellular matrix of vocal folds, and the optical clearing sample preparation used to increase depth penetration

for imaging the tissue. Section 3.6 describes the image analysis techniques applied, namely image registration to compare vocal fold injury conditions; preprocessing and segmentation of CT images for creating 3D computer models; and quantitative analysis of fibers visualized by NM.

Chapter 4 describes acquisition of human and laboratory animal high-resolution CT images of heavy metal-stained ex vivo specimens, and the steps taken toward development of anatomical atlases and computer models by segmentation. First, anatomical results from CT images are shown, highlighting the anatomical features discerned. Then, early results from segmentation approaches are shown, commenting on the quality of the resulting models and future progress required to complete them.

Chapter 5 presents the application of MRI, CT, and NM to a rabbit vocal fold scarring study. The selection of study parameters such as sacrifice timepoint and injury method are discussed by reviewing published articles analyzing vocal fold injury in a rabbit model with or without treatment. Then, animal study results are presented, visualizing the injuries by different imaging modalities, commenting on rabbit vocal fold injury progression. The images obtained from each modality are also compared. Quantitative data analysis as applied to NM images is then shown in simulation and real images.

Finally, Chapter 6 is a discussion of results from the previous chapters, including problems encountered and suggestions for solutions. It summarizes the advantages and disadvantages of each imaging approach (Table 6–1) to help with selection of imaging modalities, and discusses the imaging and analysis pipeline applied in Chapter 5 for visualizing rabbit vocal fold injury progression. After evaluating how research objectives were met in this work, future research directions motivated by the results of these studies and others in the field are described, including improved imaging and analysis methodology for in vivo and ex vivo studies of vocal fold scarring.

1.4 Contributions

Imaging and training: Rui Tahara conducted CT imaging on the Xradia 520 Versa at the Cell Imaging and Analysis Network (Chapters 4 and 5). The author conducted CT imaging on the SkyScan 1172, with training provided by Lihong Shang at the McGill Institute for Advanced Materials (Chapter 5). Stephen Nuara conducted CT imaging on the Vimago system (Chapters 4 and 5). Marius Tuznik conducted MRI imaging on the PharmaScan at the Small Animal Imaging Laboratory of the McConnell Brain Imaging Center, Montreal Neurological Institute (Chapter 5). The author conducted all imaging presented on the FV1200MPE NM system, with training provided by Alexei Kazarine (Chapter 5). Alexei Kazarine and Angelica Gopal devised the idea of applying uDISCO optical clearing to increase penetration depth for the preliminary study (Chapter 5) [21]. Melina Jaramillo Garcia and the author conducted imaging on the FVMPE-RS NM system (Chapter 5). Robert Gagnon did sputter coating of glass to create mirror slides (Chapter 5).

Human cadaver and animal studies: Geoffroy Noel prepared and dissected the human cadaveric larynges (Chapter 4). Karen Hope Stone and Stephen Nuara were responsible for animal handling and care (Chapter 5). Rabbit vocal fold microsurgery was done by Sarah Bouhabel, Qiman Gao, and Almoaiyadbellah Rammal, with support provided by Huijie Wang (Chapter 5). Sample dissections were done by Huijie Wang, Qiman Gao, Geoffroy Noel, and the author (Chapters 4 and 5). Sample preparation with optical clearing for NM imaging, and for SkyScan 1172 CT imaging, was done by the author (Chapter 5). Staining with PTA for the Xradia 520 Versa was done by Rui Tahara (Chapters 4 and 5).

Analysis: The author and Sareh Taheri did manual subsampled segmentation of the human cartilages (Chapter 4). Benjamin Provencher at Object Research Systems conducted initial U-net segmentation of the rabbit specimen with manually segmented training data done by the author (Chapter 4). Other processing was done by the author, with in-person and online training and guidance for using the Dragonfly software provided by Nicolas Piché, Zixiong Cao, and others from Object Research Systems (Chapter 4). Model creation and

3D printing were done by the author, with 3D printer training provided by Harrisonn Griffin at the McGill Physics Makerspace (Chapter 5). The author implemented linear collagen simulations and image correlation spectroscopy (Chapter 5). The author and Taylor Bell implemented wavy collagen fiber simulations and Fourier analysis (Chapter 5). Amir K. Miri provided the wave fitting code used in a previous publication (Chapter 5) [22]. Image analysis of simulated and real fiber images was done by the author (Chapter 5).

Supervision and editing: Paul W. Wiseman and Luc Mongeau provided research supervision and edited the thesis. Partial editing of the thesis was provided by Nicole Y. K. Li-Jessen and Taylor Bell.

CHAPTER 2
Background

2.1 The larynx

The larynx is an organ composed of cartilages, muscles, and soft tissue located in the neck, shown in Figure 2–1. It is the primary phonatory organ in humans and some animals, containing the vocal folds which serve as a vibratory sound source by modulating lung airflow. The larynx also fulfills vital functions in respiration, as it is responsible for keeping the airway unblocked and preventing pulmonary aspiration [11]. These functions are facilitated by the concerted action of the specialized tissues in the larynx. An understanding of its anatomy is thus crucial to appreciate the impacts of pathological changes in voice disorders.

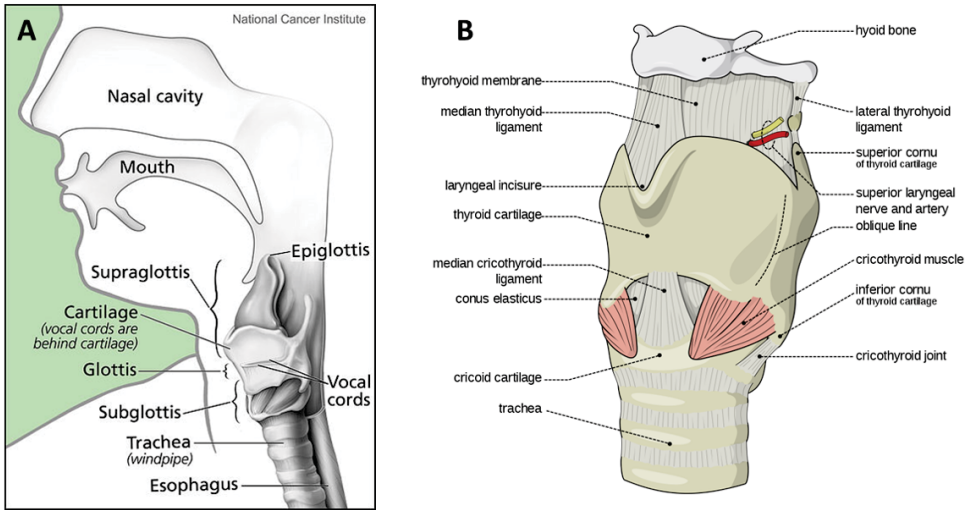

Figure 2–1: (a) A diagram demonstrating the location of the larynx within the neck. Public domain image by Alan Hoofring, National Cancer Institute. (b) The external anatomy of the larynx. Illustration by Olek Remesz, reproduced under the Creative Commons Attribution - Share Alike 2.5 License.

The human larynx undergoes changes during the lifespan, including differentiation of vocal fold tissue layers occurring through childhood and adolescence [23], and atrophy of soft tissues and ossification of cartilages in later life [11]. Pediatric laryngology is a distinct

specialty within laryngology as significant histological differences necessitate disparate treatment approaches [23]. Vocal fold nodules, among other voice disorders, are highly prevalent in children [8], motivating additional research into this area. The larynx also exhibits interspecies differences. Its gross anatomical structure, including certain cartilages and muscles, are conserved between similar species, but human phonation and vocal function are largely unique [24]. This holds implications for the selection of animal models for studying vocal disorders and testing treatments. An example of interspecies differences is the presence of macula flavae, structures implicated in vocal fold repair and development, in human and rat vocal folds but not in those of dogs, pigs, or rabbits, three common animal models for vocal fold studies [25]. Another is the absence or difference of the microstructural layers that characterize human vocal folds in laboratory species [26, 27]. The following background sections will use the mature, adult human larynx to introduce laryngeal anatomy and physiology, while laryngeal features relevant to vocal fold scarring studies in common laboratory animals will be compared and contrasted to the human larynx in Section 2.1.4.

2.1.1 Larynx anatomy and physiology

The larynx has three main functional states: swallowing, respiration, and phonation. The anatomy and functioning of the larynx as will be described in the following two paragraphs is drawn from three laryngology textbooks [11, 28, 29].

The functions of the larynx are structurally facilitated by the laryngeal cartilages connected by membranes and ligaments, shown in Figure 2–2, which are themselves postured by the intrinsic and extrinsic laryngeal muscles. The larynx is innervated by the laryngeal nerve, a branch of the vagus nerve. The laryngeal arteries supply blood, and the laryngeal veins drain into the thyroid vein. The epiglottic cartilage is situated at the top of the larynx and is attached to the thyroid cartilage, the largest cartilage of the larynx. The epiglottis, parts of the arytenoid cartilages [30], and the corniculate and cuneiform cartilages are made of elastic cartilage, while most of the other laryngeal cartilages are made of hyaline cartilage, which contains more collagen. The thyroid cartilage serves as a superior attachment

point for the ring-shaped cricoid cartilage, which itself is the attachment point for the paired arytenoid cartilages. The paired arytenoid cartilages serve as the attachment point for the true vocal folds, often referred to simply as the vocal folds. The vocal folds are formed as mucosa-covered edges of the cricothyroid ligament, which is also called the conus elasticus due to elastic components. The false vocal folds are dually attached to the posterior part of the arytenoids and to the thyroid cartilage.

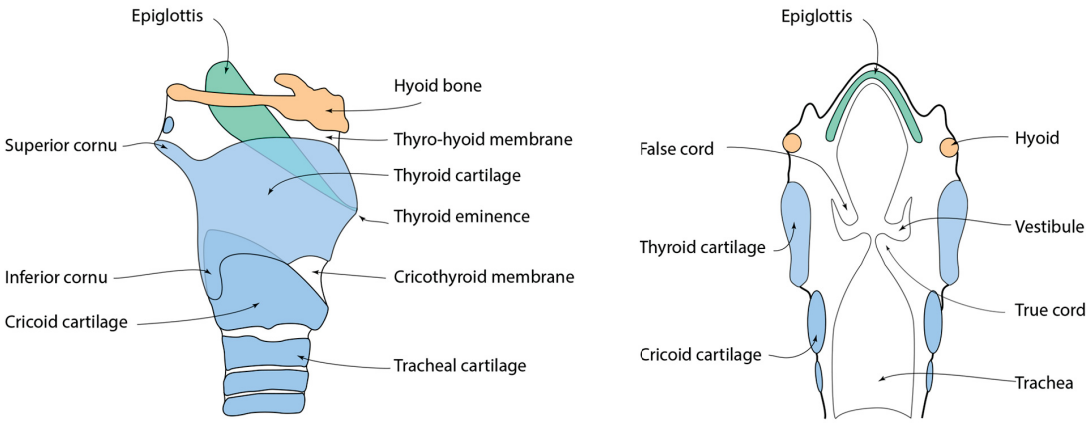

Figure 2–2: Sagittal (left) and coronal (right) views of the larynx, identifying the hyoid bone, cartilages, and connective tissues. Reproduced from `https://www.enteducationswansea.org/`, with permission from Simon Browning.

In swallowing, the epiglottic cartilage located at the top of the larynx closes the inlet into the larynx to prevent pulmonary aspiration, and within the larynx the false vocal folds also close together in a sphincteric function. The extrinsic muscles of the larynx, which attach to the tongue-involved hyoid bone, move the larynx upward during swallowing to facilitate passing of food. In respiration and phonation, the epiglottic cartilage is postured anteriorly to allow air inflow and outflow through the larynx. The intrinsic laryngeal muscles play roles in phonation and respiration, as the vocal folds must be moved together (adducted) for phonation or pulled apart (abducted) for efficient respiration. The position of the vocal folds as determined by the adductor and abductor muscles is called vocal fold posture. The posture is critical in determining phonation frequency or pitch, as lengthened vocal folds are thinner and vibrate at a higher frequency. The vocal folds are abducted by the posterior

cricoarytenoid muscle and adducted by the thyroarytenoid muscle, lateral cricoarytenoid muscle, and arytenoid muscle. In phonation the vocal fold mucosa vibrates as a mucosal wave at a frequency defined by posturing, while the intensity of sound is affected by the airflow provided by the lungs. Following sound generation by the larynx, the sound is processed in the upper vocal tract and pharynx where it is filtered by the acoustic response of the vocal tract before release.

2.1.2 Vocal fold microanatomy

Human adult vocal folds exhibit a layered structure, with each layer characterized by specific distribution and organization of extracellular matrix (ECM) components. The characteristics of the ECM components making up each layer of the vocal folds determine their bulk mechanical properties, with the distribution illustrated in Figure 2–3.

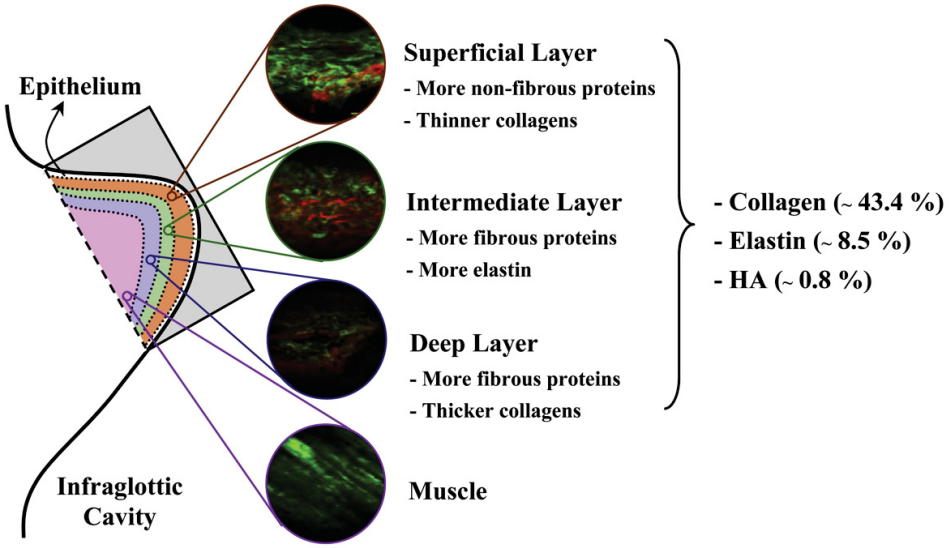

Figure 2–3: Elastin, collagen, and hyaluronic acid (HA) distribution in human vocal folds. Reproduced from [1], with permission from Elsevier.

The layered structure discussed in this paragraph is adapted from references [11, 22]. Superficially, a stratified squamous epithelium borders the air. Following a basement membrane bordering the epithelium is a highly pliable layer called the superficial lamina propria or Reinke's space, composed of hyaluronic acid with some collagen and elastin. The intermediate lamina propria beneath Reinke's space contains more fibrous collagen and elastin.

The deep lamina propria exhibits collagen organization into larger bundles. Attached to the deep lamina propria is the vocalis muscle, which is a specialized section of the thyroarytenoid muscle. The superficial layers are often called the cover or vibratory portion of the vocal fold, while the deeper layers are called the body or vocal ligament. The pliability of the vocal folds ensures that low threshold pressure is needed for phonation onset; as a result, healthy vocal folds are able to efficiently convert airflow to vibration, while under pathology this efficiency is compromised. Compromised efficiency can worsen dysfunction, as inefficient phonation can lead to additional phonotrauma, resulting in the formation of lesions including nodules, polyps, and scars.

Vocal folds experience high impact forces in normal phonation, requiring structural and elastic components to maintain structural integrity and vibratory functionality [31]. Collagen fibers are abundant in the lower layers of the vocal fold, closer to the vocalis muscle. Various types of collagen organize in different ways; some types organize into fibrillar structures, while others are non-fibrillar. In the vocal folds, collagen plays a largely structural role. Collagen distribution and organization in human vocal folds was investigated using immunohistochemistry (Section 2.2.1); type I, III, IV, and V collagen were found in the vocal folds, with type IV and V found mostly in membranous structures, fibrillar type III playing an important structural role throughout the lamina propria, and fibrillar type I providing strength to the lower layers of the lamina propria [32]. With collagen providing structural support, elastin is important in allowing the vocal folds to deform in response to mechanical stresses such as muscle posturing and vibratory motion. Like collagen, elastin is also present in fibrillar and non-fibrillar forms, with non-fibrillar elastin largely populating the superficial lamina propria layer, and elastin fibers concentrated in the intermediate and deep lamina propria [33]. Other vocal fold components include glycosaminoglycans such as hyaluronic acid and proteoglycans such as decorin and fibromodulin. These components act as determinants of viscosity and response to shear stress, in addition to regulating structure of other ECM components like collagen [34, 35]. The histological differences in vocal fold

layer components have biomechanical consequences. The upper layer vibrates freely, and the lower layer is present to absorb mechanical stresses in vibration and posturing [11].

2.1.3 Vocal fold wound healing and scarring

A trauma to the vocal folds initiates a cascade of responses. Depending on the tissue properties and the severity of the injury, this cascade is modified in timing, and it may also be left incomplete as in the case of vocal fold scarring and polyps [36, 37]. In the vocal folds, as for other tissue systems, wound healing can be simplified and described as involving three distinct phases: inflammation, ECM deposition and epithelialization, and remodeling. A typical complete wound healing cascade is shown in Figure 2–4, from the original insult through ECM remodeling to the healthy tissue end result. Acute inflammation occurs shortly after injury, triggering tissue swelling and immune cell recruitment to the wound [37]. Following this stage, fibroblasts migrate into the wound site and begin to deposit ECM components, reforming the disrupted scaffold. Some fibroblasts introduced from circulating blood differentiate into specific vocal fold fibroblast cells for synthesis of vocal fold ECM [31]. Due to the urgency of reforming a scaffold to avoid additional infection, the deposited scaffold is disorganized and may have a different distribution of ECM components as compared to the original tissue. The tissue is also contracted to minimize the size of the wound [37]. Concurrently, an epithelial layer is reformed by an influx of epithelial cells. At this point, a barrier has formed against infection, and the mechanically stiff, extracellularly disorganized tissue can be remodeled to approximate the original tissue more closely. In some cases, the tissue is successfully remodeled and original mechanical properties are recapitulated; in other cases, a scar remains. Maturation and remodeling may persist for many months as proteoglycans and glycoproteins such as decorin and fibronectin regulate ECM formation [31].

When a scar is formed, extensive cross-linking between ECM components, in addition to the greater amounts of collagen, increases tissue stiffness [31]. Such changes to vocal fold mechanical properties affect vocal fold phonation as the mucosal wave is disrupted.

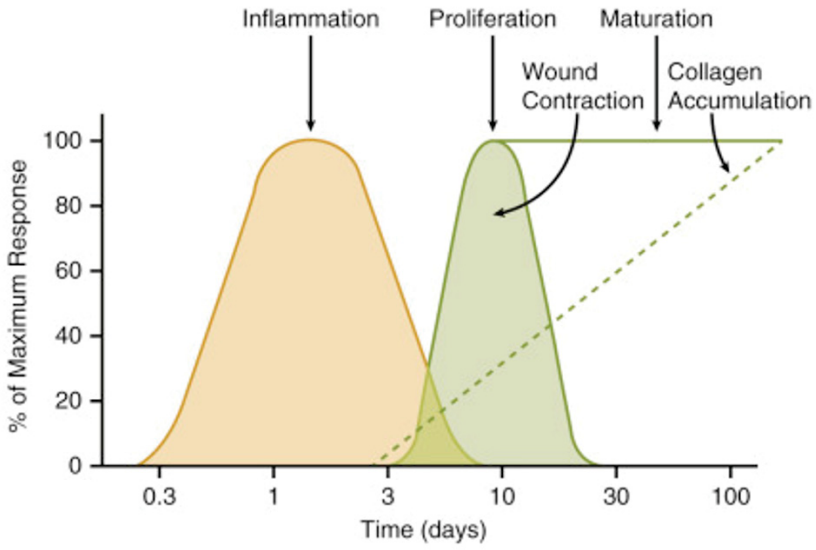

Figure 2–4: The phases of the wound healing process, and their approximate timeline. Reproduced from [2], with permission from Elsevier.

Vocal folds are also tissues that experience high levels of stresses in their normal function, which may potentially make it harder for them to remodel [37]. In fact, even following the remodeling phase vocal folds often retain their impaired mechanical properties, reducing voice quality. The section of the vocal fold composed of scar tissue is often adynamic, and in some cases the layered structure is completely disrupted. In addition to the increased amount of collagen, the disorganization of elastin also seems to play a detrimental role in the effects of scarring on vocal fold function. Elastin disorganization has been observed in human, rabbit, and dog vocal fold scarring [14, 38, 39].

Vocal fold scarring can arise in numerous scenarios in response to any disruption to the epithelium, lamina propria layers, or muscle. Examples include mechanical disruptions such as phonotrauma and endotracheal intubation, chemical disruptions such as laryngopharyngeal reflux, inflammation due to infection, and iatrogenic causes such as surgical intervention for lesion excision [13, 40, 41, 42]. Phonosurgery for excising vocal fold lesions, such as malignant tumours, can be done with a laser causing a thermal injury, or with cold instruments causing mechanical trauma [11]. The wound healing response may be different in each of

these cases. Vocal fold scars exhibit different morphologies, as they may be flat or raised, or exhibit a deficiency often characteristic of sulcus vocalis [29]. In raised and deficiency scars, the vocal folds are often unable to adduct properly in vibration, similarly to the presentation encountered with lesions like nodules and polyps; in other cases, the vocal fold layering is disrupted resulting in inefficient phonation and vocal fatigue [29].

No consensus has yet emerged for the best treatment approach for vocal fold scarring, either to apply prophylactically during vocal fold surgery or to later apply to encourage proper vocal fold remodeling. One early treatment investigated was surgical disruption of the scar [43], which may worsen outcomes [11]. Deficiency scars may benefit from medialization laryngoplasty, which can close the glottal gap to reestablish vocal fold meeting at the median [40]. Other treatment approaches include injection of autologous fat and other materials, as well as voice therapy to help patients take maximal advantage of airflow support and acoustic resonance in voice produce with the aim of reducing compensatory hyperfunction which could itself lead to additional phonotrauma as well as fatigue [11]. Injectable biomaterials can serve as a prophylactic approach, as they may be able to direct the wound healing process toward an outcome with sufficient remodeling rather than scarring. Currently, popular treatment approaches undergoing preclinical investigation include injectable biomaterials such as collagen [44], hyaluronic acid [45, 46, 47] and other hydrogels like chitosan; tissue engineering [15]; and stem cell therapy [48].

2.1.4 Animal studies

Animal studies are currently a critical preclinical component of the path to introducing novel treatments for vocal fold scarring. Animal models can provide some insight into negative and positive therapeutic implications, such as immune response and remodeling efficacy. Humans, however, have differences in laryngeal anatomy and vocal fold microstructure from common laboratory animals, and as a highly phonatory species, are unique in the amount of mechanical stress imparted regularly on the vocal folds. There is no common laboratory animal that is accepted above all others for vocal fold scarring studies; interspecies differences

require the careful selection of an appropriate animal model for each study. Each species has specific advantages and disadvantages in their similarity to human laryngeal anatomy, ease of microsurgical intervention, and cost; research groups also often choose animals that they have experience with. There are various animals used as models: small animal models in widespread use are rats and rabbits, with a recent increase in ferret models as their vocal folds are large in relation to their body size compared to rats and rabbits, facilitating surgery [49]. Larger animal models used for studying vocal fold scarring include pigs [50] and dogs [51, 52]. These studies are, however, much more expensive than small animal studies, and may be better applicable for later studies after validation in a small animal model. Vocal fold layer structure is different in morphology and ECM component distribution and organization between humans and laboratory animals; this result has been obtained from investigations involving dogs, pigs, monkeys, rats, rabbits, and ferrets [16, 49, 17]. These differences may be critical, since the disruption of normal vocal fold layer ECM components is implicated in the biomechanical impacts of vocal fold scarring. Another example of a difference between human and animal vocal fold structure is the presence of macula flavae in rats and humans, but not in rabbits, pigs, and dogs [25]. This structure is implicated in vocal fold repair, making it potentially relevant for studies of vocal fold scarring.

In addition to the difference in laryngeal structures between laboratory animal models and humans, practical challenges exist that complicate animal studies of vocal fold scarring. For example, phonosurgery on small rodents such as rats and rabbits can be challenging to accomplish as intended. One complication can be finding available surgical instruments and endoscopic equipment of appropriate size for these animals, requiring adaptation of pediatric surgical setups. Impaired endoscopic visualization can lead to the injury of components other than the vocal folds, such as adjoining cartilages [53]; analysis of cartilages instead of vocal folds can also occur following improper histological slicing and tissue identification [54], further motivating 3D imaging approaches. More recently there has been increased progress toward developing in vitro tissue models for vocal fold studies, but these are not

yet sufficiently developed to replace animal models for wound healing and treatment studies [55]. Animal models are thus still an important preclinical step for studying vocal fold scarring treatment efficacy following in vitro cell studies in 2D or 3D culture, motivating additional comparative investigations to better characterize laryngeal anatomy and physiology in humans and the animal models used in preclinical studies.

2.2 Imaging

Imaging is an integral component of most studies of human and animal laryngeal anatomy and physiology. When applied in conjunction with other methods, such as rheology to measure tissue mechanical properties [1] or induced phonation functional analysis to quantify function [56], images inform how specific tissue features influence laryngeal performance and pathology. Imaging methods such as CT, MRI, videoendoscopy, and ultrasound are widely used in clinical diagnosis and for in vivo research in humans and animals [57]. Ex vivo tissue imaging can also be done using CT and MRI, with improved image quality accorded by longer scan times and use of toxic stains or radiation doses. Other ex vivo imaging techniques lend themselves well to studies of structure and function at the molecular level, such as 2D histology and immunohistochemistry, nonlinear microscopy, atomic force microscopy, and electron microscopy [58].

These techniques are diverse in their contrast mechanisms, sample preparation requirements, resolution, and the size of samples they accommodate. The image quality of each technique is also constrained by noise sources, imaging artifacts, and spatial resolution [59]. The best imaging protocol needs to be determined for the research question at hand with the technical limitations in mind. The structure being imaged is also necessarily much more complicated than any of the image representations created by one imaging method. This motivates multimodal imaging, since the images from different techniques can be compared and combined through image fusion (Section 2.3.1) to better describe the real subject.

2.2.1 Two-dimensional histology

The method most often applied for analyzing tissues at the cellular level across biomedical disciplines is 2D histology. This method entails micron-scale slicing of tissues, followed by labeling with histological stains or antibodies to reveal morphology and provide information on molecular distribution. Following fixation to preserve the tissue and keep structures intact, the tissue is often either embedded in wax or frozen for slicing with a microtome [60]. The slice is mounted on a slide and stained with histological stains or with antibodies for biomolecules of interest, then observed with an optical microscope [60].

In studies of vocal fold scarring, 2D histology is generally used to observe the ECM, the distribution of cell types, and injected biomaterials. These goals can often be achieved with histological stains. One of the most common stains used is hematoxylin and eosin (H&E), whereby basic hematoxylin labels cell nuclei in blue and acidic eosin labels cytoplasm and ECM in shades of pink [61]. Figure 2–5 shows canine vocal folds labeled with H&E staining. This recognizable method is commonly applied in vocal fold scarring animal studies, where it is used to obtain an overview of tissue structure, characterize extent of scarring, and show localization and resorption of injectable biomaterials [62, 63, 64].

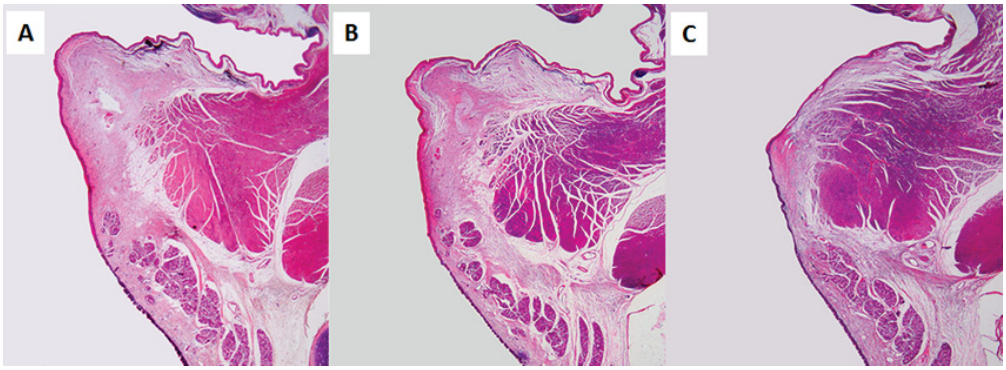

Figure 2–5: Hematoxylin and eosin (H&E) stained images of canine vocal folds. The epithelium, muscle, and connective tissue structures are identifiable with this stain, as well as their changes in abnormal states. (a) shows normal vocal fold, (b) shows an injured vocal fold treated with transplanted tissue engineered vocal fold mucosa, and (c) shows an injured vocal fold with no treatment applied. The injury performed was a type II cordectomy. Reproduced from [3], under the Creative Commons Attribution 4.0 License.

Another stain used in such studies is Masson's trichrome, of interest for connective tissue as it includes a fiber stain in its combination of dyes [65, 62, 66]. Picrosirius red is a dye more specifically targeting collagen [64, 67]. As redistribution of elastic fibers is another expected marker of scarring, stains for elastic fibers such as Verhoeff's van Gieson staining [62] and orcein [64] are also employed. Glycosaminoglycans, such as hyaluronic acid, can be stained with Alcian blue [63]. Histological stains are not specific because they target a chemical property of biomolecules of interest that may also be exhibited by other molecules. When higher specificity is desired, it is possible to target specific biomolecules with antibodies in an immunohistochemical approach [68]. The primary antibody for the biomolecule can be conjugated directly to an enzyme that catalyzes the deposition of a chromogen, or to a secondary antibody that is conjugated to such an enzyme or fluorophore [68]. Protein distribution is then observed with an optical microscope. In vocal fold scarring studies, collagen [64] and hyaluronic acid [69] are common targets.

Useful information on tissue composition may be obtained from 2D histology, but these methods have limitations. The requirement of cutting the tissue into thin slices makes it a destructive method, prohibiting subsequent application of other types of analysis on the tissue. The slicing process introduces artifacts such as deformations, which make reconstructing 3D information unfeasible, resulting in the loss of 3D information. Finding the location of interest is also non-trivial, requiring serial sectioning. Serial sectioning, staining, and imaging are labor-intensive and time-consuming, and the small sample size requirements make accurate sectioning difficult and error-prone. In response to these challenges, many researchers have moved toward 3D virtual histology approaches. In virtual histology, 3D images are acquired using methods such as NM, MRI, and CT, applying virtual slicing to obtain 2D information at any location in the specimen [70]. As histological focus transitions to virtual histology, it is important to compare evolving volumetric virtual histology methods with traditional, more widely accepted planar methods [71]. Virtual histology can also

provide information to inform targeted slicing for 2D histology, reducing some of the burden imposed by serial sectioning [72].

2.2.2 Computed tomography

Computed tomography (CT) reconstructs x-ray projections over many angles to create tomographs, or 2D cross-sectional slices of a 3D object. The most common contrast mechanism used for CT, absorption contrast, is based on differential x-ray attenuation between tissues. X-ray attenuation is determined by tissue density and composition; high density materials, such as metal and bone, absorb x-rays very well, causing a high attenuation [59]. The effective atomic number of the material also greatly impacts CT imaging, with high-atomic number materials corresponding to high x-ray attenuation [73]. There is an exponential relationship $I = I_0 e^{-\mu x}$ between the incident x-ray intensity I_0 and attenuated x-ray intensity I, modified by the linear attenuation coefficient μ of the material and the distance x from the source [74]. An x-ray detector is used to detect the attenuation, forming a projection image. Following acquisition of x-ray projections, these images must be reconstructed into tomographs using back projection, requiring sufficient angular sampling over at least 180° [75].

X-ray illumination is most often provided by an x-ray tube in a laboratory setup. In this system, electrons are accelerated across a high voltage before they interact with a tungsten anode, producing a broad energy spectrum of x-rays [74]. The energy of the x-rays can be increased by using a synchrotron source if available. Synchrotron sources improve safety for in vivo imaging by decreasing the radiation dosage required for the same image quality [76]. For ex vivo scanning, synchrotrons improve image quality while minimizing scanning time [77, 78]. Microcomputed tomography systems have much higher resolution capability than clinical CT. This arises from the small focal spot of micro-CT x-ray tubes reducing blur from the source, as well as the addition of microscope optics [79]. A diagram of a typical ex vivo micro-CT system is shown in Figure 2–6. In vivo micro-CT systems are similar except for the sample placement, as the stage is stationary while the imaging system rotates.

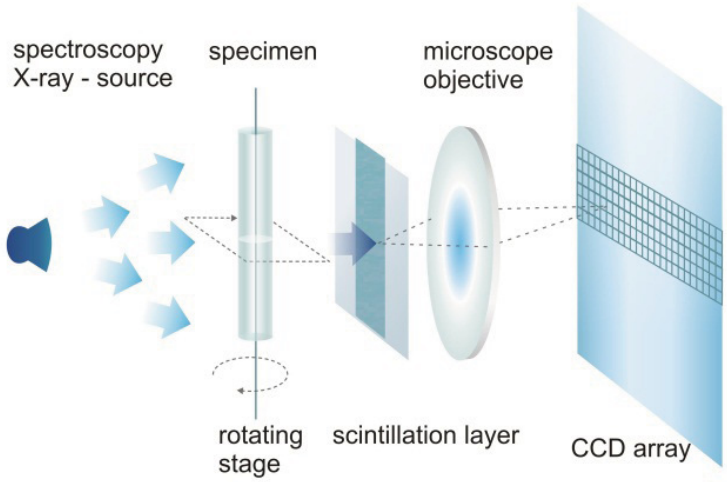

Figure 2–6: The components of a micro-CT scanner for ex vivo samples. A source emits x-rays which are attenuated by their interactions with the specimen on the stage. The mechanical stage rotates, and images are acquired at many rotation angles for later reconstruction. The attenuated x-rays interact with a scintillation layer for conversion of the signal to visible light. A microscope objective then magnifies the image, and the signal is detected on a charge-coupled device (CCD) detector array. The type of scanner shown is a cone-beam CT scanner. Reproduced from [4], under the Creative Commons Attribution 3.0 License.

For in vivo CT imaging of the larynx, it is advantageous that the vocal folds are directly bordered by air. The very low x-ray attenuation of air makes it easy to see the border of the vocal folds [80], and this contour can be examined for the detection of lesions given sufficient resolution. The acquisition time requirements are very low compared to MRI, thereby minimizing movement artifacts from swallowing and breathing [81]. Clinical CT has been used for imaging vocal tracts, even without contrast agents, for both research and clinical purposes [82, 83]. Of interest to vocal fold scarring studies, micro-CT has been used to observe fibrosis [84] and to characterize injectable hydrogels [85].

Stains

Mineralized tissues are readily observed with absorption contrast CT in vivo and ex vivo due to their large x-ray attenuation from their high effective atomic weight [86]. Absorption imaging of softer tissues is challenging due to the low contrast they provide, and often requires contrast-enhancing staining. For in vivo CT, contrast agents must be non-toxic with high

x-ray absorption. Iodine is commonly used as it meets these criteria, and is often introduced by intravenous injection. It however shows fast renal clearance, especially in small animals. For small animal in vivo micro-CT, contrast agents like iodine or metals can be delivered via nanoparticles to slow clearance [80]. For ex vivo CT, options for contrast agents are more diverse as they include toxic agents. Ex vivo specimens can be stained by immersion. Alternatively, contrast agents can be introduced by vasculature perfusion, depending on the desired contrast result [87, 88]. The toxic agent phosphotungstic acid (PTA) has been found to produce very effective contrast in ex vivo soft tissue imaging [89, 90, 91], though iodine is also used. We recently applied PTA stain to visualize submicron details in rabbit vocal folds [21]. Another consideration when choosing stains is whether the stain will need to be removed for further analysis such as histological staining or label-free nonlinear microscopy. Iodine is considered reversible and PTA is often considered to be irreversible [92], though one study has explored PTA stain reversal with chemical agents [93]. The PTA stain has also been shown to be compatible with immunohistochemical analysis, circumventing the issue of stain removal for this method [94, 95].

Phase contrast

The x-ray contrast described so far arises from x-ray attenuation, which changes the amplitude of the beam. However, as the x-ray electromagnetic waves are sensitive to refractive index changes, it is also possible to observe their phase lag as they traverse the specimen [96]. Phase contrast imaging provides much higher density contrast in soft tissues than attenuation-based imaging [96]. Human vocal folds were recently imaged with synchrotron phase contrast imaging, achieving resolution down to 650 nm and successfully visualizing vocal fold microstructure [97].

2.2.3 Magnetic resonance imaging

Magnetic resonance imaging (MRI) investigates internal structures by taking advantage of the magnetic properties of hydrogen's proton: the hydrogen atom induces a small magnetic field because of the proton's quantum spin. Nuclei in a strong static magnetic field are

perturbed by a weak oscillating magnetic field, and then emit an electromagnetic signal that has a frequency characteristic of the magnetic field at the nucleus; this is the process of nuclear magnetic resonance [59]. In an MRI scanner, a large magnetic field is generated by a superconducting electromagnet made of coils of superconducting wire in which electric current moves very quickly [59]. A radio frequency (RF) pulse can induce changes in proton spin alignment. A pair of RF pulses produces a spin echo (SE); gradient echo (GRE) uses one RF pulse followed by gradient reversal, allowing the observation of different relaxation properties [98]. In both cases, as the hydrogen atoms rotate past measurement coils, they induce an electric current corresponding to their magnetic moment. Because this process uses non-ionizing radiation, safety concerns related to the ionizing x-ray radiation required for CT are eliminated for in vivo imaging. The main safety concern lies in the strong magnetic field, which attracts ferromagnetic materials. Patients with non-removable ferromagnetic materials, including pacemakers and certain implants, cannot be scanned [99]. Clinical MRI scanners usually have a magnetic field strength up to 3 T, while small animal MRI increases up to 7 T; it may, however, be safe to use higher magnetic fields up to 20 T, which will dramatically increase the quality of images acquired from this modality in the future, although the impact of high field strength on tissue heating is important to evaluate [100].

In MRI, the pulse parameters determine the type of contrast obtained in the image, two important ones being repetition time (TR) and echo time (TE). The variety of possible pulse sequences makes MRI a versatile technique for the observation of multiple tissue properties. The TR corresponds to the time lag between applied RF pulses. The time lag between pulses allows the longitudinal magnetization to recover. The TE corresponds to the time lag between the applied RF pulse and the signal's peak; this corresponds to the electrical signal induced by the hydrogen atoms [101]. The signal equation, $S = k\rho(1 - e^{\frac{-T_R}{T_1}})e^{\frac{T_E}{T_2}}$, depends on these two pulse parameters to determine the weighting, or contrast mechanism; namely T1 or T2 for SE sequences. For example, with low TR, T2 weighting dominates,

leading to the T2 signal approximation $S = k\rho e^{\frac{T_E}{T_2}}$ [59]. The signal is also modulated by $k\rho$, corresponding to spin density effects.

The three most common MRI weightings are T1-weighting, T2-weighting, and proton density-weighting. Using a short TR and TE, the scan is considered T1 weighted, as T1 corresponds to the spin-lattice relaxation as the longitudinal magnetization recovers [59]. In this process, the measured signal decreases as protons realign with the scanner's magnetic field; the fastest ones to realign give the highest signal. The T1 weighting provides strong signals for fat and for paramagnetic contrast agents, among which gadolinium is most frequently used. Using a long TR and TE, the scan is T2-weighted, corresponding to spin-spin relaxation as transverse magnetization is decreased [59]. In this process, the protons rotate asynchronously; the slowest ones to dephase produce the strongest signal for this weighting. The T2 weighting visualizes water content. Using a short TE and a long TR results in proton density weighting, with signal determined by the proton density in the tissue [101].

The measurement acquired by MRI is in k-space, requiring the transformation of the image to the spatial domain using an inverse 2D or 3D Fourier transform. The k-space data acquisition of MRI is exploited in RApid imaging with Refocused Echoes (RARE) sequences, also called fast spin echo (FSE) sequences; this type of sequence was applied in our study of rabbit vocal fold injury, described in Chapter 5. This sequence is a modification of the normal spin echo sequence, made faster by acquiring multiple k-space lines per repetition. One example pulse sequence diagram for RARE is shown in Figure 2–7. In the conventional SE sequence, a 90° excitation RF pulse is applied, followed by a 180° refocusing pulse to refocus the transverse magnetization into an echo. The echo is subsequently measured and displayed in the readout [101]. In the RARE sequence, following a 90° excitation multiple 180° refocusing pulses are applied, resulting in a train of spin echoes [101]. A different phase encoding gradient is applied for each echo. Each echo can then be applied as a line in k-space, speeding up the scan time by a factor of the echo train length compared to a conventional spin-echo sequence with one refocusing pulse [101].

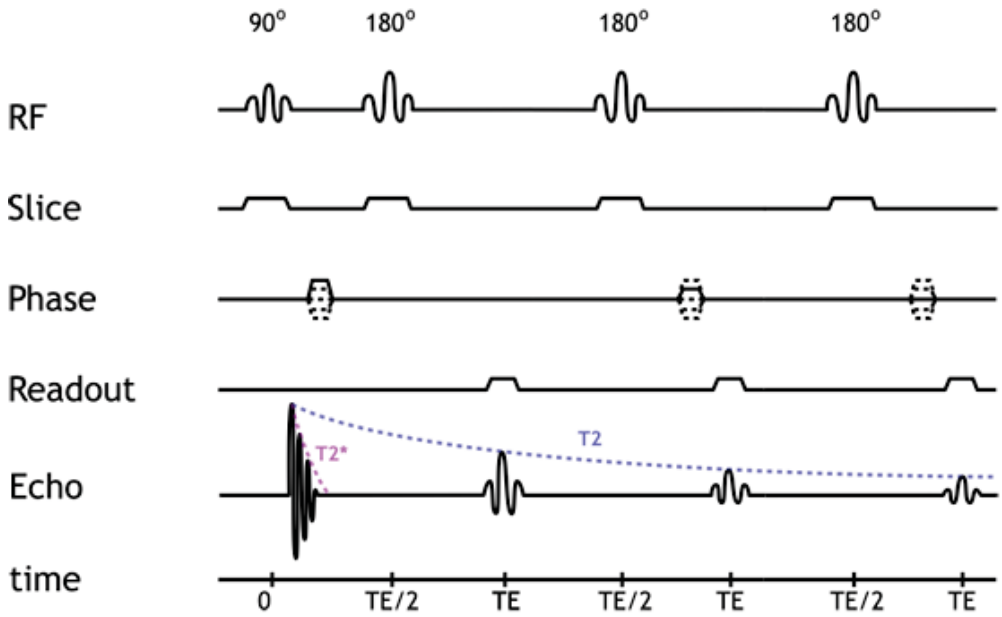

Figure 2–7: The pulse diagram for a RARE sequence with an echo train length of three. The initial excitation RF pulse is followed by three refocusing pulses. Three different phase encoding gradients are used, allowing readout of three lines in one iteration of the pulse sequence. Reproduced from `http://xrayphysics.com/sequences.html`, with permission from Mark M. Hammer.

Prior to MRI scanning, the scanner must be calibrated, and the patient or ex vivo sample must be adequately prepared. Calibration of the scanner involves addressing the inhomogeneity of the magnetic field: in the shimming process, the field homogeneity is adjusted by sending small currents through imaging and shim coils [98]. For in vivo and ex vivo scanning, contrast agents can be introduced. The most frequently used agent is the paramagnetic substance gadolinium, which can be injected for in vivo imaging [11]. Ex vivo samples can be stained by immersion, or the contrast agent can be introduced by perfusion [102]. Ex vivo samples must be situated in avoidance of air pockets or bubbles, which can show up in the scan as susceptibility artifacts. The samples can also be immersed in MRI-inert media to eliminate any background signal contributed by their immersion medium. Two substances often used are Fomblin [103] and the perfluorocarbon substance Fluorinert [104]; Fluorinert has been found to be compatible with 2D histology analysis [105]. For in vivo imaging, a consideration is that required scan time is usually longer than for CT. In laryngeal

MRI, movement artifacts, such as swallowing and respiration, can degrade image quality; shorter scan times or scan gating can mitigate these effects [11]. In preclinical laryngology, MRI with and without contrast agents has provided promising results, visualizing scars in ferrets [103] and rats [104], implanted polyethylene glycol in dogs [103], fat grafts in ferrets [103], phonation posture to validate a thyroplasty intervention in rabbits [102], and vocal fold hydration state under systemic dehydration in rats [106].

2.2.4 Ultrasound

Ultrasonic imaging employs high frequency sound waves to visualize tissue features by measuring changes in acoustic impedance of tissues. These sound waves are emitted by a piezoelectric transducer placed near the tissue of interest, and acoustic waves return to the transducer following absorption, reflection, and scattering of the signal [107]. The time delay and amplitude of the signal is used to form an image of the internal structure [107]. There has been success in visualizing laryngeal features including vocal fold nodules [108], characterizing vocal fold motion [109], and estimating vocal fold displacement velocity [110]. Ultrasound is minimally invasive and inexpensive so it can be employed as a first-pass method to characterize pathology, but it is limited in penetration depth and structure resolution, and current ultrasound systems in widespread clinical use are usually not capable of three-dimensional imaging.

2.2.5 Nonlinear microscopy

The nonlinear regime of optical microscopy has proved to be a useful way to probe tissue structure in cultured cells and tissue slices. For virtual histology, the increased penetration depth afforded by the infrared (IR) wavelengths used in conjunction with the targeted imaging of endogeneous fluorophores and harmonophores make nonlinear microscopy (NM) a very appealing method [111]. In optical microscopy, the objective lens focuses an excitation laser beam to the sample plane [112]. It also collects emitted fluorescence, which is filtered from the excitation light and observed with a detector [112]. The properties of the objective lens

including magnification, working distance, and numerical aperture must be adapted to the research question at hand [112].

A specialized form of light microscopy is fluorescence microscopy, which uses fluorescent dyes or proteins to investigate the localization and dynamics of small biological molecules including proteins and nucleic acids [113]. In transfected cell culture studies or transgenic animal studies, a fusion protein can be made linking the protein of interest to a fluorophore, which is then expressed by cells [113]. For tissue studies in non-genetically modified animals, fluorescent molecules are most often introduced with an antibody targeting a biomolecule of interest conjugated with a fluorescent dye as in immunofluorescence, closely related to the immunohistochemistry method discussed in Section 2.2.1 [113]. Tissues also exhibit autofluorescence due to natural sources of fluorescence endogeneous to the tissue. These include NADH, elastin, and other substances which can be observed with fluorescence microscopy [19]. In single-photon fluorescence microscopy, one photon is absorbed for each excitation by a fluorophore, and a slightly lower-energy photon is emitted due to a thermal loss called the Stokes shift [113]. The energy diagram for this transition is depicted in Figure 2–8a. Since one photon is absorbed and one photon is emitted, this is deemed a linear process.

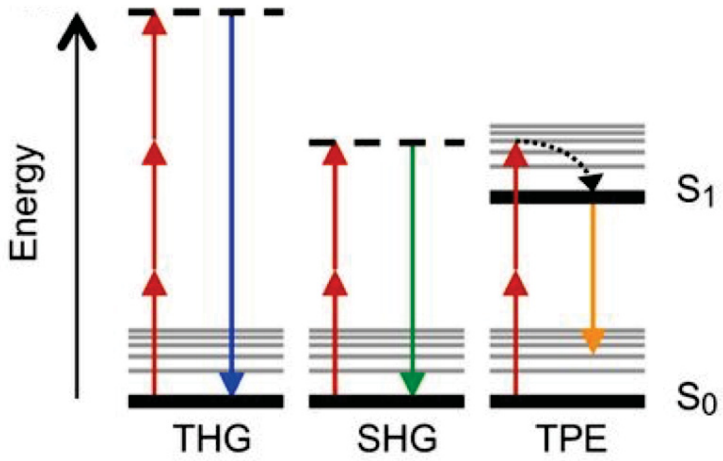

Figure 2–8: Jablonski diagrams illustrating the energy transitions encountered in nonlinear imaging, THG (third harmonic generation), SHG (second harmonic generation), and TPE (two-photon excitation). Other relaxation pathways are not shown. Reproduced from [5], with permission from The Company of Biologists, Ltd.

The use of higher-energy pulsed laser illumination enables the nonlinear optical regime since the optical properties of a material can change under the illumination of the high intensity laser beam. In nonlinear microscopy, pulsed lasers are used to achieve short high peak energy intensities. Nonlinear microscopy systems are usually laser-scanning microscopes similar to confocal microscopes, but generally do not use a pinhole as the low probability of nonlinear events confines the excitation to the focus of the Gaussian laser beam [114]. Two typical nonlinear microscopy setups are shown in Figure 3–1. There is increased interest in light-sheet illuminated nonlinear systems for faster large-sample imaging [115]. In the nonlinear regime, a power series expansion $P = \chi^1 E(t) + \chi^2 E^2(t) + \chi^3 E^3(t) + ...$ is used to calculate polarizability [111]. This equation represents the nonlinear relationship between material susceptibility χ and the time-dependent electric field $E(t)$ of the laser light. χ2 is the second-order susceptibility, which corresponds to the second harmonic generation (SHG) process, in which two photons are annihilated and one photon is released [116]. This process occurs in dense noncentrosymmetric structures [116]. Energy conservation prescribes that the released photon has twice the energy of the incident photons, thus doubling the frequency and equivalently halving the wavelength as shown in Figure 2–8b. The polarization of the laser greatly impacts results, motivating the use of circular polarization to reduce bias in-plane [116]. SHG is also preferentially emitted in the forward direction due to phase-matching conditions, though a low proportion of backward emission occurs under certain configurations, and backscatter can allow backward detection [116]. If only backward detection is available on a nonlinear microscopy system, signal enhancement has been demonstrated by placing the sample on a metal-coated slide to reflect photons back into the objective [117]. In two-photon fluorescence, a third-order susceptibility process, two photons from the laser excite a molecule to produce one fluorescence photon after a delay; the same logic holds for the process of three-photon fluorescence [111]. As in single-photon fluorescence, thermal energy loss results in the Stokes shift, as shown in Figure 2–8d. The polarization of the laser does not affect this incoherent process, and the emission is volumetrically isotropic.

The Stokes shift of fluorescence means that for an equal excitation wavelength, the second harmonic generated signal will have a slightly lower wavelength than the two-photon fluorescence, allowing both signals to be imaged simultaneously with separate detectors following beam splitting [118]. Third-harmonic generation (THG) corresponds to a third-order nonlinear susceptibility $\chi 3$ process and it is produced by refractive index transitions with sizes similar to the beam focus [5]. THG results in one photon with three times the energy of the incident photons, as shown in Figure 2–8c. Other third-order nonlinear processes, such as coherent anti-Stokes Raman spectroscopy and stimulated Raman scattering, are also utilized in bioimaging when chemical sensitivity is desired [119]. Other higher-order processes are under investigation for potential biomedical spectral imaging applications [120].

Biological intrinsic sources of nonlinear phenomena greatly motivate the use of NM in virtual histology. Fibrillar collagen of type I and type III has a high second-order nonlinear susceptibility, making SHG bioimaging highly useful for investigating ECM in healthy and diseased tissues label-free [116]. Nonlinear microscopy has been applied to vocal folds in several studies using SHG of collagen [22, 121, 122, 21]; collagen alignment has been found to be correlated with stiffness, providing potential insight into tissue mechanics [122]. Microtubules, structurally polar structures made up of joined tubulin dimers, are another potential biological source of SHG [123]. In NM virtual histology, samples must be prepared to a certain thickness due to penetration depth limitation, which is also addressed using optical clearing [124]. The method is theoretically light diffraction limited corresponding to spatial resolution approximately half of the emission wavelength, but reaching the diffraction limit in practice is increasingly improbable deeper within the sample as light scattering and aberrations increase and useful signal decreases.

Optical clearing

Optical clearing describes a group of methods used to improve the penetration depth of visible light by decreasing lateral scattering in the sample. The application of optical clearing methods allows thick tissue volumes to be observed for 3D analysis or later virtual sectioning

at locations of interest. Numerous optical clearing methods have been developed, with two important classes formed by aqueous and solvent-based methods [124, 125, 126]. In solvent-based methods, the tissue is preprocessed by dehydration and delipidation then immersed in a medium matching the refractive index of the dehydrated tissue. The dehydration step leads to tissue shrinkage, which is advantageous for visualizing larger structures. Anisotropic shrinking may however distort tissue morphology, and it must be taken into account when analyzing images of the cleared samples. The optical clearing method selected in this study and applied in our recent work [21] is uDISCO, an inexpensive, accessible solvent-based method developed for high fluorescence preservation [127]. New optical clearing methods continue to emerge, improving parameters such as fluorescence preservation and labeling efficiency [128].

2.2.6 Endoscopy

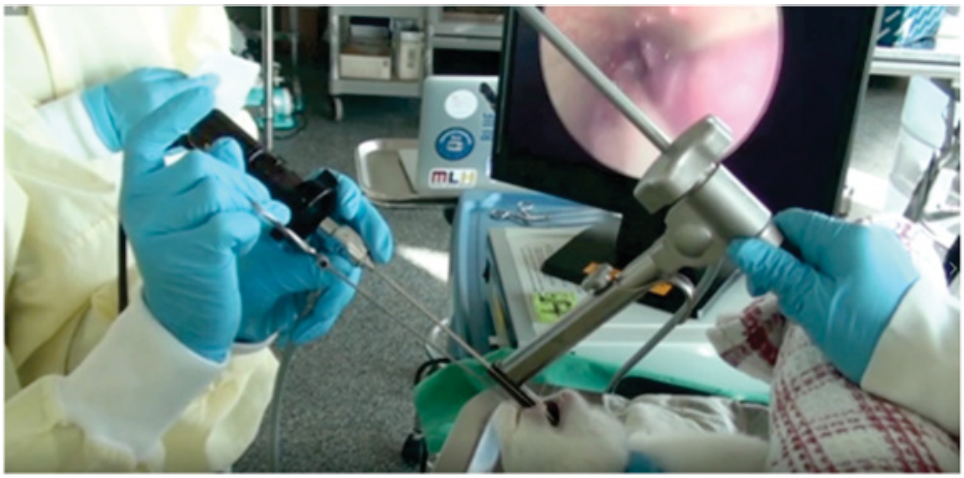

Figure 2–9: Rigid laryngoscopy and concurrent microsurgical manipulation in a rabbit experiment. A rigid laryngoscope is inserted through the mouth, and a flexible laryngoscope is inserted through the nose. Author's picture.

Laryngeal endoscopy, or laryngoscopy, is used widely in laryngological practice and research. As shown in Figure 2–9, this involves the insertion of an endoscopic probe through the mouth or nose into the throat of the patient to assess the health and function of the vocal folds and other laryngeal tissues [28]. Videostroboscopy can also be employed to visualize

vocal fold vibratory characteristics and obtain information on the mechanical properties of healthy or diseased vocal folds [28]. Standard laryngoscopes contain either an eyepiece or an optical camera, and can visualize lesions such as tumours, nodules, and scarring on the surface of the vocal folds. Abnormal lesions must often be biopsied for analysis. As a biopsy is an invasive surgical procedure, it is of interest to better characterize the lesion in situ to determine whether intervention is necessary. New endoscopic probes are being developed that can acquire information at depth, visualizing the subsurface extent of a lesion and identifying lesions that are not readily visible. One imaging method often applied in these probes is optical coherence tomography (OCT) [129]. OCT is a Michelson interferometer-based method, and the contrast mechanism relies on spatial variations of refractive indices. Traditional OCT has been applied ex vivo for tracking of vocal fold injection in real time [130], in vivo for high-resolution visualization of nodules, cysts, and vocal fold sulcus [131], and polarization-sensitive OCT has shown promise in scar localization [132]. OCT endoscopes have also been developed; they have successfully visualized vocal fold paralysis [133], scar, nodules, and papilloma [134].

Multiphoton or nonlinear endoscopy is also an area of active research and development. As discussed in Section 2.2.5, this modality can specifically visualize changes in fibrillar collagen and autofluorescent entities like elastin fibers, which can be markers of disease states. Successful imaging with multiphoton endoscopes has been demonstrated in tissue sections [135], live animal kidney imaging [136], and other applications [137]. Current challenges facing this method include slow scan times and loss of signal in depth penetration; these will need to be remedied with developments from adaptive optics and other engineering fields.

2.3 Analysis

2.3.1 Image registration

Comparing images is a commonplace concern, as multiple images of the same specimen are often acquired with different modalities or under different conditions, or it is of interest to compare two samples. To facilitate comparison, it is necessary first to place both images

onto a common coordinate system. The process of finding the correct geometrical transformation to align the images anatomically is called image registration. Image registration can be used to bring images into alignment from different modalities, modified sample preparation or imaging parameters in the same modality, or with a template from an anatomical atlas for comparison [138]. In this process, a reference image is kept static while the other image is mobile and undergoes a transformation. Common components of transformations are translation, rotation, and resizing; rigid transformations are used if imaging scales are trusted, but a more generally affine, nonrigid transformation can be applied if scaling or skew are suspected in the dataset [138, 139]. Non-affine, or deformable, transformations can be used when affine approaches fail, though they are more computationally intensive. The transformation must be optimized to maximize the similarity between the two images. This optimization problem requires a cost function, which can be chosen based on the known similarity between the images, such as whether the images are taken with the same method. Many cost functions exist, though intramodal registration usually uses the sum of squared differences function $SSD = \frac{1}{N}\sum_{i}^{N}|A(i) - B'(i)|^2$, while intermodal registration often uses mutual information $MI(A, B') = H(A) + H(B') - H(A, B')$ based on the Shannon entropy equation H; additional cost functions also exist [59, 140]. The best fit can then be found iteratively by minimizing the cost function. Following fit optimization, the quality of the registration is often also qualitatively evaluated using anatomical landmarks.

Many biomedical applications exist for image registration. Images in the same modality must be compared following sample preparation manipulations either on the same sample or another, such as changes in fixation or staining method; within one specimen, intramodality registration may be done between images taken before and after a treatment intervention. Another example of intramodal image registration is comparison with an anatomical atlas depicting a generic healthy specimen. Intermodal registration also has many applications, for example finding a 2D view in 3D data, such as finding the location of a 2D histology slice [141]. Following image registration, image fusion can also be applied; image fusion describes

combining two images to display aggregated information [142]. As different imaging methods hold complementary information due to differing contrast mechanisms, the combination of two modalities can consolidate this information; this is commonplace with positron emission tomography, which is often combined with MRI or CT of the same patient [139]. Within one modality, image fusion can solve problems arising from suboptimal imaging systems; for example, several orientations of the same sample suffering from localized aberrations can be combined into one improved image [142].

2.3.2 Three-dimensional computer models from biological images

Virtual histological images of the larynx in humans and animals are now routinely created from CT scans of the larynx [143]. The vocal fold layers can be delineated by CT and MRI imaging [144], and high-resolution micro-CT resolves muscle fibers in human vocal folds [97]. There is also a wealth of information available on the anatomical features of the larynx [11, 145, 29, 28]. Such image sets contain valuable information that can be used to create highly realistic computer models, which can later be used for simulation, bioprinting, or surgical planning.

Image stacks must be processed to create high-quality models, following the acquisition of high-quality images. They must be segmented and refined. Segmentation is often done manually or semi-automatically with the aid of various softwares, including ITK-SNAP [146], 3DSlicer [147], and Dragonfly (Object Research Systems). The segmentation of some structures can be expedited by using intensity thresholding, or histographic segmentation using datasets processed by filtering with edge-enhancement or other criteria. These first-pass methods are effective in laryngeal image segmentation for clearly delineated structures such as cartilages, requiring minimal to moderate post-processing [143]. When higher specificity is desired, the accuracy of these methods breaks down and manual segmentation must be applied, entailing the identification and labeling of regions of interest by an expert. This is a tedious, time-intensive, and expensive process, especially for high-resolution datasets

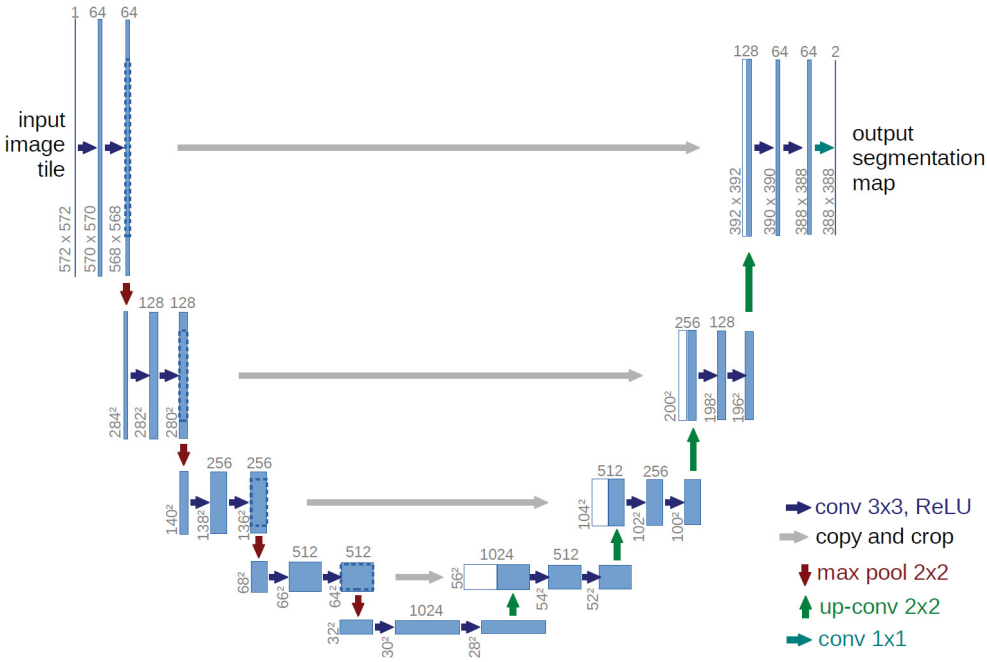

Figure 2–10: The U-Net architecture, often used for biological deep learning image processing. The architecture is a contracting network with max pooling followed by upsampling with up-convolution. The convolution layers use rectified linear unit (ReLU) activation. The conventional contracting layers consolidate contextual information into a tractable feature map, and the following expanding network layers augment precision by improving feature localization. Reproduced from [6], with permission from Springer Nature.

which may exceed 1000 individual slices. One option to expedite this process is supervised automated segmentation. This approach requires the manual labeling of a training dataset, which is used to train a supervised machine learning algorithm that can be applied to segment the unlabeled images. The advent of deep learning and convolutional neural networks (CNN) has revolutionized image processing, as CNNs show remarkable accuracy in image classification and segmentation tasks compared to other machine learning methods [148]. The application of such approaches is facilitated by imaging processing softwares such as Dragonfly, which introduce a manual segmentation and visualization front-end to deep learning software packages like Tensorflow [149, 150]. The network architecture often used in biological image segmentation is the U-Net architecture shown in Figure 2–10 [6], with the more recent development of volumetric U-Nets capable of integrating 3D information [151].

Following segmentation, a mesh can be generated and smoothed as required to create a 3D model amenable to further analysis.

Solid models are useful in applications such as biomechanical simulations, bioprinting, and surgical planning. Computational fluid dynamics models of airflow and finite element analysis of deformable structures using softwares such as ANSYS and COMSOL have long been performed to improve understanding of phonatory function for normal and pathological states. Studies however commonly use 2D environments or simplified 3D vocal folds and vocal tract geometries; left-right symmetry is also often an assumption in mechanical studies with simulation vocal folds [152]. In current studies, it is more commonplace to extract airway geometry from CT or MRI scans [153]. Increasingly, simulations link fluid, structure, and acoustic interactions into a single simulation incorporating feedback from each of these mechanical systems [154]. These complicated simulations can benefit from microstructural images that provide a better approximation of structural components and organization. Improved computational resources are making such computational complexity more feasible. Another application of volumetric computational models is bioprinting, a growing area of research and development that entails the printing of realistic scaffolds and cell architectures for functional studies. Microstructural imaging with high-resolution CT and nonlinear microscopy can be used to design realistic scaffolds. Bioprinting has already been used to create a realistic liver model by introducing human hepatocytes in a matrix [155]. There are multiple potential applications of bioprinting within laryngology. It can be used to conduct preclinical studies of treatment interventions in a more realistic setting than conventional in vitro 2D and 3D cell culture; for medical training using realistic printed models; and patient-specific models can be used in pre-operative planning. Another eventual application for bioprinting may be for creating a personalized bioprinted larynx for a laryngectomy patient [156]; this is however a complicated venture as the larynx is a dynamic, multifunctional organ with much higher complexity for regeneration than other organs with more structural roles [157]. Image-guided surgery is another potential application, as structural information

prior to surgery allows a surgery to be planned and practiced. Images can be acquired during surgery and aligned with prior higher resolution images to gauge progress [158, 159].

2.3.3 Quantitative fiber analysis

In studies of vocal fold scarring, it is of interest to obtain quantitative information about the rearrangement of ECM fibers in scarred tissue, as their morphology and distribution give insight into the extent and severity of scarring. Images of these fibers can be obtained with SHG microscopy of fibrillar collagen [160, 122] and when possible simultaneous two-photon autofluorescence of elastin fibers [19], or 2D histology targeted to collagen or elastic fibers. Fiber imaging was also recently demonstrated in high-resolution phase contrast micro-CT [97]. Quantitative approaches expedite and objectify analysis compared to qualitative image observation, and can introduce interesting information not readily visible qualitatively, such as predicting mechanical properties [161, 122]. Several common approaches will be outlined below.

Image correlation spectroscopy

Image correlation spectroscopy (ICS) is a spatial-domain fluorescence fluctuation analysis technique [162]. It uses fluctuations in the intensity recorded in pixels composing fluorescence microscopy images to extract molecular information by calculating a correlation function fit with a model describing parameters in the image [163]. For SHG images of collagen fibers, ICS has been applied to extract information including fiber density [164, 165], thickness [164, 165, 166], length [164, 165], and pore size for a matrix [165, 166]; as well as to extract tensor element ratios in linearly polarized SHG imaging [164] and predict mechanical properties [161]. It has also been applied to autofluorescence images of elastin [161].

The autocorrelation $g(\xi, \eta)$ of an image $i(x, y)$ can be used to quantify the degree of similarity in the signal with spatial lag increase, shown in the following equation from [163]. The fluctuations δi of the intensity are calculated by subtracting the image mean intensity from each pixel intensity, and brackets $\langle\rangle$ represent a spatial average of correlation over the image [163].

$$g(\xi,\eta) = \frac{\langle \delta i(x,y)\delta i(x+\xi, y+\eta)\rangle}{\langle i(x,y)\rangle^2} \tag{2.1}$$

The spatial autocorrelation is often calculated using an alternate computational path applying the discrete 2D fast Fourier transform (FFT) of the image, with results equivalent to the previous formulation; FFT^{-1} corresponds to the inverse fast Fourier transform, and FFT^* is the complex conjugate [163].

$$g(\xi,\eta) = \mathrm{FFT}^{-1}\{\mathrm{FFT}[\mathrm{Image}] * \mathrm{FFT}^*[\mathrm{Image}]\} \tag{2.2}$$

Once the autocorrelation function has been calculated, it must be fit with an appropriate fitting equation, incorporating the Gaussian point spread function (PSF) and potentially spatial elements specific to fiber images. In an early application of ICS to fiber images, the autocorrelation function was fit with a circular 2D Gaussian function, where 2σ corresponded to the correlation radius ω and was linked to fiber size scale, and $(2\sigma)^2$ was linked to the pore size. Low-pass filtering was found to be a useful preprocessing technique, and the application of this analysis pipeline was validated in simulations and collagen gels polymerized at varying pH [166]. Later studies have used an elliptical 2D Gaussian fit, obtaining a measure of skew calculated as the ratio of the axis standard deviations related to fiber length, and a measure of angular orientation from the rotational fit [165, 161]. Other modifications have introduced an analytical calculation of expected fiber correlation convolved with a Gaussian [167], as well as modifications taking into account polarization due to the biases introduced by linear polarization SHG [164, 168].

Fourier analysis

The 2D Discrete Fourier Transform (DFT) of an image provides spatial frequency information, which can be analyzed to obtain information on orientation and alignment. In one study, orientation was extracted using the direction of alignment of high amplitudes, as this direction is perpendicular to the preferred orientation in the image domain [169]. In another study, the variability of the 2D DFT magnitude was used to quantify disorder within sheets of collagen fibrils in corneal tissue [170]. Fourier analysis has also been applied to investigate scarring in a hamster cheek pouch model, in which the spectral density was converted to an orientation distribution to determine fiber direction and alignment [160].

Wave fitting

A wave fitting algorithm to extract fiber geometrical properties was developed to analyze SHG images of human vocal fold scar [22]. This method is highly applicable to the wavy, crimped collagen fibers often observed in tissue images as fibers are fit to a periodic function. After fibers are selected either manually or with the aid of an edge detection filter, they are fit using nonlinear least squares to a Fourier function or a sine wave [22]. The orientation of the fiber is determined by creating an ellipse with a Prony series to enclose the fitted function, and calculating its rotation from a reference axis [22]. The process yields the period and amplitude of the crimping shape of the fibers, as well as their orientation.

Curvelet transform – fiber extraction

The Curvelet Transform – FIbeR Extraction (CT-FIRE) method provides direct fiber fitting, from which parameters such as straightness and alignment can then be analyzed over the fiber population [171, 172]. This method employs preprocessing using a curvelet transform for denoising. In this filter, the image is decomposed into a set of wavelet bands, and each band is analyzed with a ridgelet transform [173]. Following denoising, fiber extraction begins with a thresholding of potential fibers. Nucleation points are then introduced at high-likelihood points, with likelihood calculated by measuring distance from each potential

fiber to a no-fiber space [171]. The nucleation points are extended, then pruned and processed based on direction, length, and distances between the fibers [171]. This results in a population of fitted fibers, over which parameters of interest can be analyzed. CT-FIRE has been applied to SHG images of dog, pig, and rabbit tissue section to probe vertical collagen alignment and straightness [122]. Dog and pig tissues exhibited vertical gradients of collagen alignment and straightness, while this was not observed in the rabbit tissues; it was also found that the introduction of strain increased both the alignment and the straightness of collagen in their tissues [122].

Forward-backward analysis

Another source of information on fiber thickness is derived from the differential forward and backward emission of SHG. Though SHG is preferentially emitted in the forward direction, local properties of the collagen can lead to backward emission and backscatter [116]. In one study, collagen thickness in collagen gels was accurately determined with atomic force microscopy, and the SHG forward-backward ratio was found to correspond to collagen thickness [174]. In another study, the forward-backward ratio was calculated for SHG images of cartilage and bone, and was successfully predicted with numerical simulation [175]. On systems equipped with forward and backward detection, the forward-backward ratio may thus be found to provide reliable local fiber thickness information.

CHAPTER 3
Materials and Methods

3.1 Ex vivo tissue acquisition

Two human larynges were obtained from the Strathcona Gross Anatomy Laboratory, McGill University, with ethical approval for the study granted by the McGill Research Ethics Board File 307-1218. One human larynx was preserved with the Thiel salt-based, minimal formaldehyde soft embalming procedure [176], and one human larynx was preserved with the Floppy phenol-based soft embalming procedure [177]. The rabbit larynx for ex vivo stained CT was acquired from a commercial source and fixed in 4% paraformaldehyde (PFA). The uninjured control New Zealand White rabbit larynx for ex vivo magnetic resonance imaging, guinea pig larynx, and rat larynx were obtained after sacrifice following unrelated laboratory studies involving no manipulations to the larynx, and were fixed in 4% PFA.

3.2 Animal study methods

Results are presented from two studies conducted as part of the McGill Comparative Medicine and Animal Resources Centre (CMARC) Protocol 2014-7556.

3.2.1 Injury timepoint study

Three New Zealand White rabbits were obtained from Charles River Laboratories. Animals were anesthetized, their vocal folds were located with rigid endoscopy, and they underwent unilateral vocal fold injury with biopsy forceps. Surgical endoscopic video was recorded for subsequent comparison with experimental results (see Figure 2–9). One rabbit was sacrificed at each timepoint: 3, 10, and 39 days post injury. The rabbit sacrificed at 39 days was imaged with the Vimago CT directly following sacrifice. Larynges were excised and fixed in 4% PFA.

3.2.2 Treatment study

New Zealand White rabbits were obtained from Charles River Laboratories. Animals were anesthetized, their vocal folds were located with rigid endoscopy, and they underwent a unilateral vocal fold modified microflap surgery. They then underwent vocal fold injection with either a treatment hydrogel (chitosan, collagen, or glycol chitosan) or a saline control. Rabbits were all sacrificed at 42 days post injury, and treatment outcome was investigated with either functional analysis or imaging. For the imaging study, larynges were excised following sacrifice and fixed in 4% PFA.

3.3 Computed tomography (CT)

Imaging with the Xradia 520 Versa (Zeiss) X-ray microscope was performed by Rui Tahara at the Cell Imaging and Analysis Network, McGill University. Images were reconstructed with XMReconstructor software (Zeiss). Imaging with the SkyScan 1172 (Bruker) X-ray microscope was performed by the author, trained by Lihong Shang, at the McGill Institute for Advanced Materials. Images were reconstructed with NRecon software (Bruker). Imaging with the veterinary grade Vimago CT (Epica Medical) was performed by Stephen Nuara at CMARC. For all CT images shown, imaging conditions led to absorption contrast, and scan parameters are listed in Table 3–1.

3.3.1 CT sample preparation

Contrast enhanced samples were stained with phosphotungstic acid (PTA) following recommended protocols for soft tissue staining [91]. First, samples were passaged into ethanol to a final concentration of 70%. Then, they were stained with PTA dissolved in 70% ethanol with constant agitation on a nutator. Incubation times and PTA concentration were determined based on sample size.

For scan times exceeding one hour, samples were imaged in agarose or 70% ethanol. For scan times shorter than one hour, some stained samples were still imaged in solution as the increased contrast allowed sufficient visualization of the sample. For unstained samples undergoing a short scan, excess moisture was removed and samples were placed in an imaging

tube which was closed or covered with a laboratory sealing film to prevent the specimen from dehydrating during the scan.

Table 3–1: CT scan parameters

Sample	Scanner	Voltage	Current	Filter	Voxel	Stain	Solution
H-F	Xradia	80 kV	85 µA	LE5	33 µm	2.5% PTA; 14d	70% EtOH
R-CS	Xradia	60 kV	82 µA	LE3	12.39 µm	1% PTA; 10d	70% EtOH
R47FA	Xradia	60 kV	82 µA	HE1	26 µm	1% PTA; 13d	agarose
GP	Xradia	60 kV	82 µA	HE1	15.02 µm	1% PTA; 7d	agarose
Rat	Xradia	60 kV	82 µA	LE2	15.02 µm	1% PTA; 7d	agarose
R39LR	Xradia	60 kV	82 µA	LE5	11 µm	1% PTA; 4d	agarose
R39HR	Xradia	60 kV	82 µA	LE5	0.7 µm	1% PTA; 4d	agarose
R1-L	SkyScan	55 kV	181 µA	Al 0.5	11.63 µm	none	air
R2-L	SkyScan	51 kV	192 µA	Al 0.5	11.45 µm	none	air
R3-L	SkyScan	62 kV	161 µA	Al 0.5	11.97 µm	none	air
R3	Vimago	80 kVp	60 mA	none	150 µm	none	intact

3.4 Magnetic resonance imaging (MRI)

Magnetic resonance imaging was conducted at the Small Animal Imaging Laboratory, part of the McConnell Brain Imaging Centre at the Montreal Neurological Institute. Imaging was performed by Marius Tuznik working with David Rudko. The instrument used was the Pharmascan (Bruker) small animal MRI scanner with an actively shielded 7 T magnet. The coil was chosen depending on specimen size: a 22 mm diameter coil for samples in 15 mL conical tubes, and a 35 mm diameter coil for samples in 50 mL conical tubes. Both were birdcage volume coils for radiofrequency reception and transmission.

Test scans were acquired at 300 and 200 µm isotropic resolution to optimize imaging parameters. Final scans were conducted at 100 µm isotropic resolution using a three-dimensional Turbo spin echo RARE sequence with repetition time 2000 ms, echo time 67.21 ms, echo train length 12, flip angle of 180°, and one average.

3.4.1 MRI sample preparation

Samples were placed in 15 mL or 50 mL conical tubes depending on their size, and padded with gauze inside the tube to minimize motion during scanning. A vitamin E capsule was fixed with tape to the outside of the sample tube at a predetermined location for easy

determination of sample orientation in acquired images. The tube was also padded with gauze when inserted into the coil for a snug fit. Samples were immersed in either phosphate-buffered saline (PBS) or Fluorinert FC-40 solution during scanning, and stored in PBS.

3.5 Nonlinear microscopy (NM)

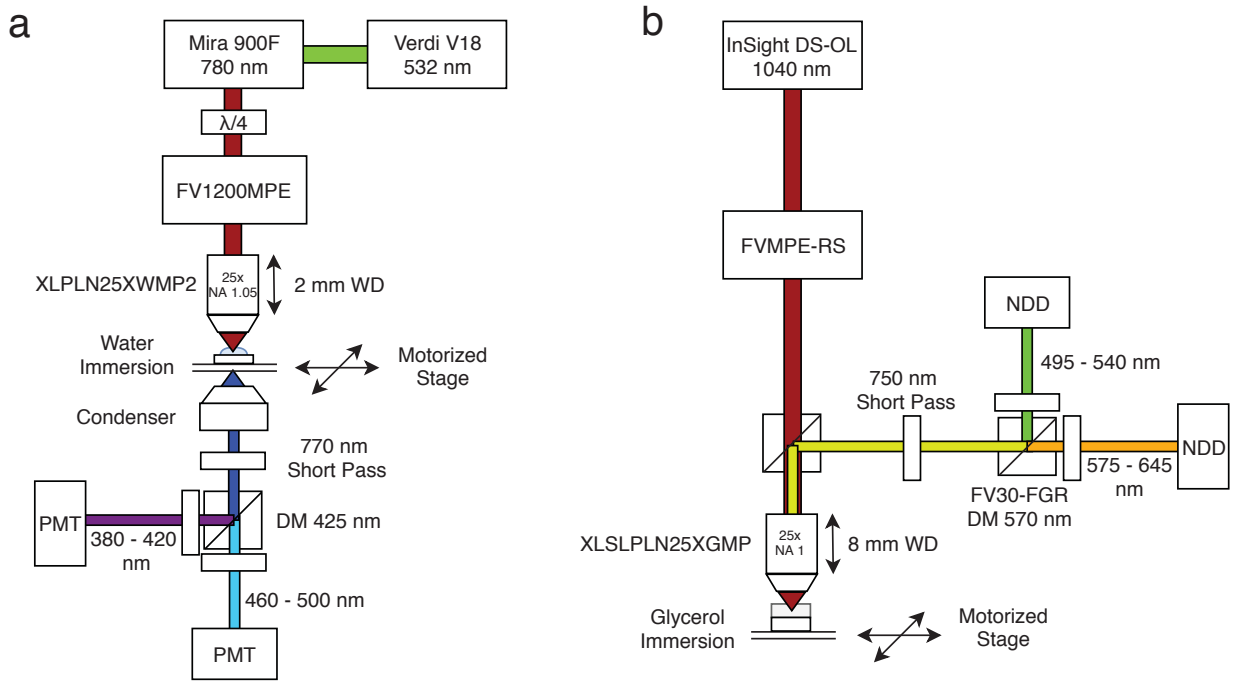

Figure 3–1: Diagram of the microscopy and illumination setup for the nonlinear laser-scanning setups, (a) FV1200MPE with 780 nm illumination and (b) FVMPE-RS with 1040 nm illumination.

Imaging of small optically cleared samples was performed using a modified multiphoton laser scanning microscope with the FV1200MPE base (Olympus). The Mira 900F Ti:Sapphire laser (Coherent), pumped by the 532 nm Verdi V18 laser (Coherent), provided 780 nm excitation. Excitation polarization was adjusted by a non-mechanical quarter-wave plate, and was kept circular for SHG imaging to ensure that collagen fibril detection was not biased by fiber orientation in the sample focal plane. Laser power was modified using a custom LabVIEW program, measured before the objective, and adjusted between 60 and 100 mW depending on the sample. The objective was a water-immersion, 1.05 NA 25x magnification XLPLN25XWMP2 (Olympus), with a working distance (WD) of 2 mm. For

samples immersed in solvent-based optical clearing solution, the objective was adjusted to its maximum positive correction collar position. Image size, magnification, PMT voltage, gain, and offset were manipulated in the Fluoview software (Olympus) and optimized for each sample. Emission was collected in the forward direction, and excitation light was filtered out with a 770 nm shortpass filter. A dichroic mirror (DM) split the emission light for simultaneous detection with two photo-multiplier tubes (PMTs), detecting transmission SHG signal through a 380 - 420 nm band pass filter and two-photon autofluorescence through a 460 - 500 nm band pass filter.

Imaging of larger optically cleared samples was performed using the FVMPE-RS (Olympus) at the Douglas Research Centre's Molecular and Cellular Microscopy Platform, an Olympus Discovery Center. The InSight DS-OL (Spectra-Physics) provided excitation at 1040 nm. The objective used was the glycerol-immersion, 1 NA 25x magnification XLSLPLN25XGMP (Olympus), with a working distance of 8 mm and refractive index correction capability of 1.33 to 1.52. Laser and scan parameters were controlled in Fluoview software. Emission was collected in the backward direction, and excitation light was filtered out with a 750 nm shortpass filter. The FV30-FGR filter cube was used, with a 570 nm dichroic mirror split the emission light for simultaneous detection with two non-descanned detectors (NDDs). Reflectance SHG signal was collected through a 495 - 540 nm band pass filter and two-photon autofluorescence was collected through a 575 - 645 nm band pass filter. To increase the signal due to a high proportion of SHG being emitted in the forward direction, a mirror was made by sputter coating glass with aluminum at approximately 80 nm thickness using the Auto 306 Cryo Evaporator (Edwards) at the Center for the Physics of Materials facility. The setup used on the FVMPE-RS microscope is shown in Figure 3–2.

For visualization of a large region of interest, the motorized stage was used to set up image mosaic acquisition. Z-stacks were acquired at each position of interest in the image plane, and full images were stitched with Fluoview. Images were visualized in 3 dimensions

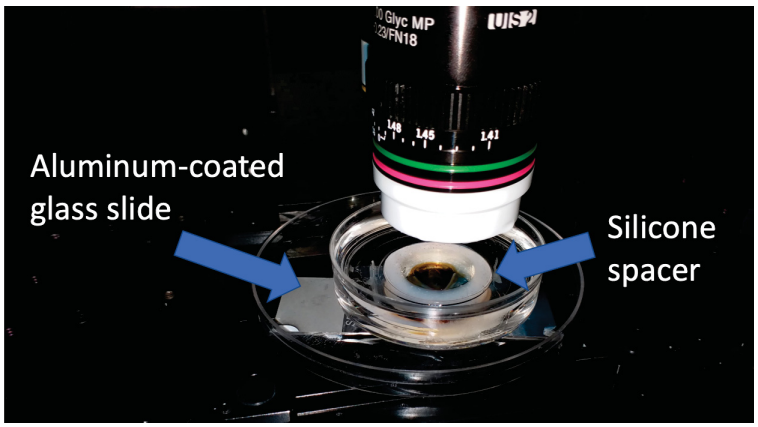

Figure 3–2: Microscopy setup showing aluminum-coated mirror slide, silicone spacer made from Dragon Skin 30 (Smooth-On), glass-bottom dish containing glycerol for objective immersion, and XLSLPN25XGMP objective with refractive index correction set to 1.49 to approximate between glycerol and BABB-D solution.

using the Fiji ImageJ platform [178, 179], Imaris software (Bitplane), and Dragonfly software (Object Research Systems).

3.5.1 NM sample preparation

Samples were dissected to the appropriate size considering the working distance of the objective, then optically cleared to increase the imaging depth of the nonlinear microscopy. Optical clearing was conducted following the uDISCO solvent-based clearing protocol [127], illustrated in Figure 3–3. Samples first were dehydrated in a series of 24-hour tert-butanol incubations: 30%, 50%, 70%, 80%, 90%, 96% in distilled water, then 100%. They were then immersed in BABB-D solution, containing benzyl alcohol, benzyl benzoate, and diphenyl ether mixed at a ratio of 1:1:10; and α-tocopherol at 0.4% by volume. For microscopy, samples in BABB-D solution were placed in a chamber consisting of a glass slide, a silicone spacer or sealing putty [180], and a glass coverslip.

3.6 Image analysis

Dragonfly software version 4.0 (Object Research Systems) was used for image registration, segmentation, and mesh creation, in addition to rendering and virtual sectioning. The software is free for non-commercial use, and can be downloaded at `https://www.theobjects.com/dragonfly/`.

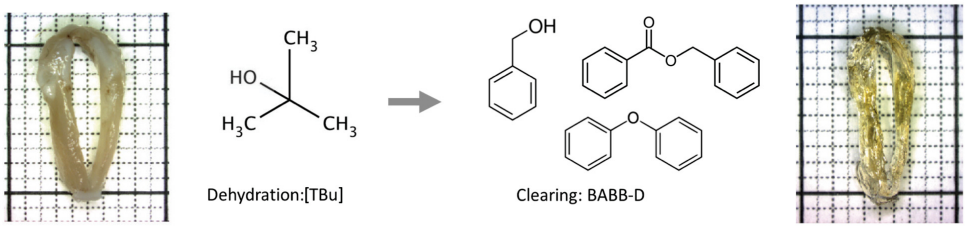

Figure 3–3: uDISCO optical clearing process, consisting of tissue dehydration followed by immersion in BABB-D clearing medium. Images taken with stereomicroscope. The small lines delineate 1 mm spacing.

3.6.1 Image registration

The Dataset Registration tool was used for image registration. To accelerate automatic registration, fixed and mobile image datasets were cropped and a mask was applied to the fixed dataset to isolate the sample from the background. The mobile dataset location was also adjusted using the Move tools to approximate the correct orientation in relation to the fixed dataset. Registration was performed allowing for rotation with an initial step of 10° and smallest step of 0.001°, and translation with an initial step of 0.05 mm and smallest step of 0.0005 mm. Intramodal image registration was performed using the sum of squared differences (SSD) cost function, and intermodal registration used the mutual information (MI) cost function. The mobile dataset was interpolated linearly.

3.6.2 Segmentation

Thresholding and histographic segmentation were explored as first-pass segmentation approaches, but did not allow differentiation between tissue types in stained, high-resolution CT images. Slices from downsampled images were manually segmented using a combination of the Smart Grid and Brush tools to create a 3D model of the laryngeal cartilages from the human CT image. For segmentation of additional structures of interest, a machine-learning based approach was followed, requiring training of a classifier with manually segmented image slices. To create training data, regions of interest (ROIs) were created for each tissue type of interest. The Deep Learning Tool was applied with a U-Net architecture [6]. Following segmentation, meshes were created from ROIs with the Generate Contour Mesh tool,

smoothed with Laplacian smoothing, and decimated. For presentation in an anatomical atlas format, text annotations were added to segmented ROIs.

3.6.3 3D printing

3D printing was done using the Prusa i3 MK3 fused-filament printers at the Physics Makerspace. The material used for printing was polylactic acid (PLA). The geometry (.stl) for a 3D printed silicone mold for creating a chamber on a glass slide is available for download: `https://a360.co/2UGYqYl`.

3.6.4 Fiber analysis

Extracellular matrix (ECM) fibers visualized with nonlinear microscopy and representative simulation images were quantitatively analyzed using four methods previously applied in similar studies. The implementations of simulations and two image analysis methods, image correlation spectroscopy and Fourier analysis, are available with documentation detailing use and required packages at the following source: `https://github.com/ksenk/fiber-simulation-and-analysis`.

Simulated fiber images

Simulated fibers were implemented in Python 3.6. Linear fibers were created in 2D with an anti-aliased line function. Wavy fibers to simulate collagen crimping were created in 2D using a sine function, with defined amplitude, period, starting coordinate, length, thickness, and rotation angle. Aliasing was mitigated for the wavy fibers by creating fibers with a thickness greater than 1 prior to image filtering with a Gaussian kernel. Then, the image was sampled to create a final simulated image. Simulated images were analyzed with the same methods as real images. Example simulations are shown in Figure 3–4.

Image correlation spectroscopy

An implementation of generalized image correlation spectroscopy (ICS) was written in Python 3.6 following [167, 163, 181]. Autocorrelations were calculated with a fast-Fourier transform method. Autocorrelation fitting to a 2D elliptical Gaussian was then implemented, omitting the central white noise containing zero lag value. This fit allowed extraction of

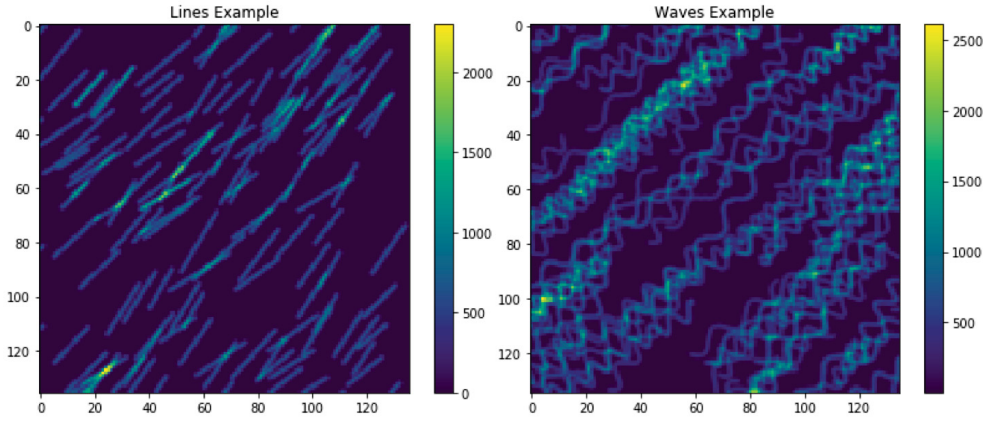

Figure 3–4: Straight (left) and wavy (right) fiber simulation examples, with rotation angles randomly determined uniformly between 30-60 degrees.

the amplitude, major and minor axis standard deviations, and rotation angle. Skew was calculated as the ratio of the axis standard deviations. Fit was assessed using the mean squared error.

Fourier analysis

Fourier analysis was implemented in Python 3.6 following an approach used to quantify scarring in hamster cheek pouches from SHG imaging [160]. Otsu's thresholding method was applied on the original image to estimate fiber density. Following Fourier transformation, the resulting power spectral density was converted to polar coordinates to evaluate orientation. The orientation distribution was then used to calculate fiber direction and directional variance, varying from perfect alignment at 0 to random organization at 1.

Wave fitting

The wave fitting (WF) method used a MATLAB script written by Amir K. Miri [22]. First, fibrils were either automatically detected with edge detection (Canny or Prewitt) or manually selected then pruned. Segments were then fitted with nonlinear least squares to a one-term Fourier model. If the Fourier fit for a segment was inadequate as calculated by the 95% confidence interval, the segment was fitted to a simple sine function. These fits allowed

extraction of the period and amplitude of the component. Fiber orientation was determined by rotation from the horizontal axis of the image.

Curvelet transform – fiber extraction

Curvelet transform followed by fiber extraction (CT-FIRE) was applied using MATLAB implementation downloaded from `https://loci.wisc.edu/software/ctfire` [171, 172]. The image was preprocessed with a curvelet transform filter. Then, potential fibers were thresholded with Otsu's method to obtain a binary image, and nucleation points were calculated using a distance transform based on the distance from each potential fiber to an empty location. The distance transform ridges were used to develop fiber trajectories extending the points. Pruning and postprocessing of fibers were applied based on direction, length, and distances between fibers. Alignment and straightness were extracted for direct comparison with a recent study applying this software to study vocal fold scarring in pig, dog, and rabbit tissue sections [122].

CHAPTER 4
Creating models of laryngeal anatomy

The objective of this chapter was to obtain high-resolution volumetric information on the structure of cartilaginous and connective tissue in the larynx for various species to provide an anatomical atlas, and evaluate feasibility of creating 3D computer models incorporating soft tissue from these images. In this chapter, results are shown from absorption-contrast CT images of the PTA-stained larynges of four species: human, rat, guinea pig, and rabbit.

4.1 Imaging results

The scan parameters for the CT images shown can be found in Table 3–1.

4.1.1 Staining results

Because of the requirement of obtaining sufficient constrast to visualize vocal folds and their underlying structure, it was important to explore the impact of staining on contrast. As the vocal folds are soft tissue, they did not provide sufficient intrinsic contrast for absorption CT imaging to obtain images of microstructure, though high-resolution information on human vocal fold microstructure has been obtained with phase contrast synchrotron CT [97]. Figure 4–1 shows absorption CT of the human larynx with and without staining. The human larynx specimens were imaged immersed in 70% ethanol to retain sample hydration and avoid movement blurring caused by dehydration during the long scan times. The images on the left show the CT scan of an excised human larynx without staining. The cartilages have high intrinsic x-ray attenuation as they are dense tissue containing high atomic number elements. It is possible to observe features of the cartilages with this intrinsic absorption contrast, such as the high degree of ossification visible in the morphology of this specimen's thyroid, arytenoid, and cricoid cartilages. The soft tissues however showed very low contrast in relation to the surrounding solution. Phosphotungstic acid (PTA) was chosen as a stain to increase the absorption contrast of soft tissue in CT images. On the right, the

human larynx is shown following 14 days of staining with 2.5% PTA. The contrast of the soft tissues was greatly increased, with the structure of the true and false vocal folds visible in the coronal view. Within the vocal folds it was possible to determine the epithelium and distinguish vocal fold layer structure. The improved contrast was thus appropriate for the goal of creating improved realistic models incorporating soft tissue features.

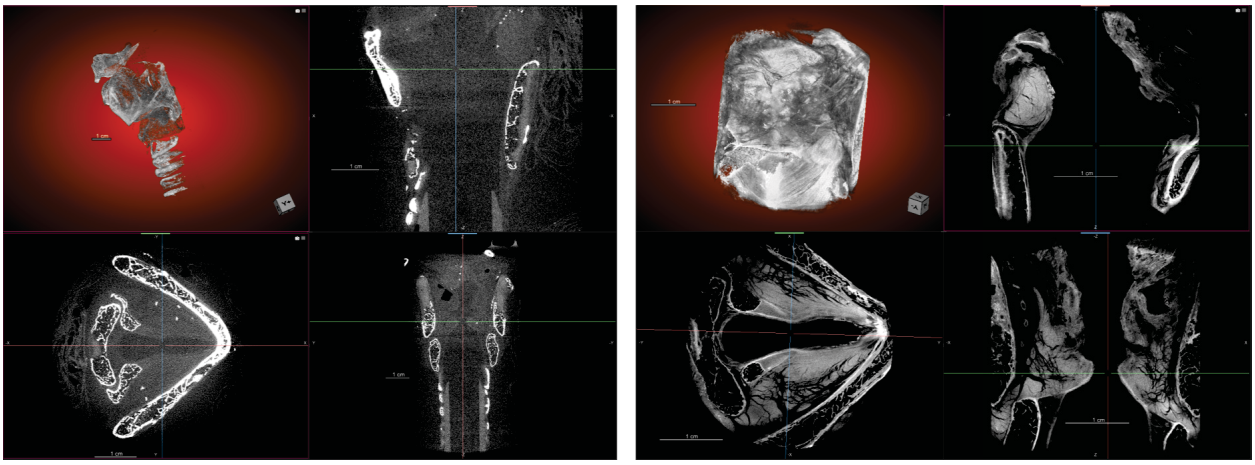

Figure 4–1: Human larynges without (left) and with (right) PTA staining for CT contrast enhancement, from the H-F scan. Clockwise from top left: 3D, sagittal, coronal, transverse views.

4.1.2 Species anatomy results

The smaller size of the rabbit, guinea pig, and rat larynx made it possible to obtain high-resolution images of the entire specimen within a reasonable scanning time. The results for the rat and guinea pig scans are shown in Figure 4–2. The cartilages, muscles, and soft tissues of both animals were clearly made visible due to the enhanced absorption contrast provided by PTA staining. The cartilages of these animals did not show the ossification seen in the human larynx, as expected for the age.

Rabbit larynges were also imaged, as a rabbit animal model was used for studying vocal fold scarring. The CT results for rabbit larynges are shown in Figure 4–3. The image on the left shows the location and orientation of the larynx within the animal prior to dissection. The center image shows the gross anatomy of the rabbit larynx, with clear visualization of cartilages, muscles, and soft tissues. This scan was originally used for measuring the size of

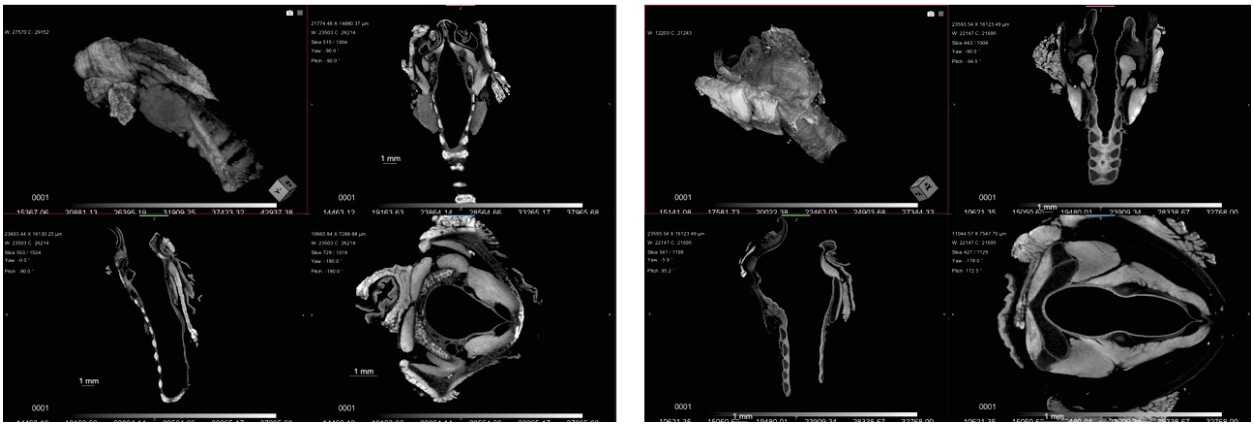

Figure 4–2: Rat and guinea pig CT. The left image shows the rat larynx, from the Rat scan. The right image shows the guinea pig larynx, from the GP scan. Clockwise from top left for each set of images: 3D, coronal, transverse, sagittal views.

the vocal folds to evaluate the dissection method used for the preliminary imaging study [21]. Higher-resolution scanning was done on a dissected vocal fold sample, which was capable of visualizing epithelium thickness, lamina propria layers with some fibrillar structures, blood vessels, and muscle fibers with PTA-enhanced x-ray contrast.

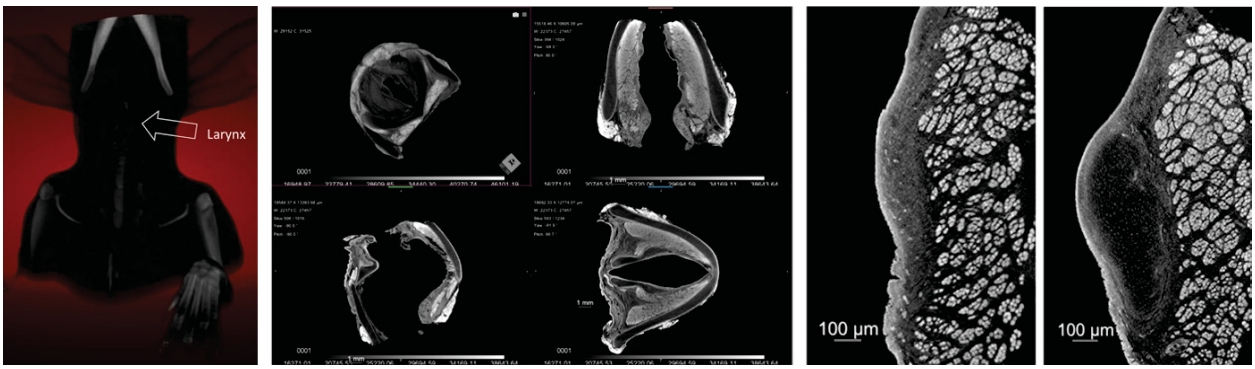

Figure 4–3: CT images of the rabbit larynx. The left image, from the R3 scan, is taken with the Vimago. The four middle images, from the R-CS scan, show clockwise from the top left: 3D, coronal, transverse, sagittal views. The two right images show a virtual slice through the vocal fold and the cartilage from the R39HR scan.

4.2 Model results

Segmentation of the images was required to create models. The initial segmentation approach tested was intensity-based segmentation due to its speed and ease of use. Features of interest were however too similar in intensity for the PTA contrast-enhanced samples,

meaning this technique did not provide accurate results. Manual segmentation of the entire images at their full resolution would be a time-intensive process, as images were between 1000-2000 slices isotropically. To create a model of the human cartilages, manual segmentation was done on an 8-fold downsampled image, with a transverse slice shown in Figure 4–4a. Following segmentation, a mesh was created to form a 3D model, shown as the white outline on the segmented image. A 3D rendering of the smoothed mesh is shown in Figure 4–4b.

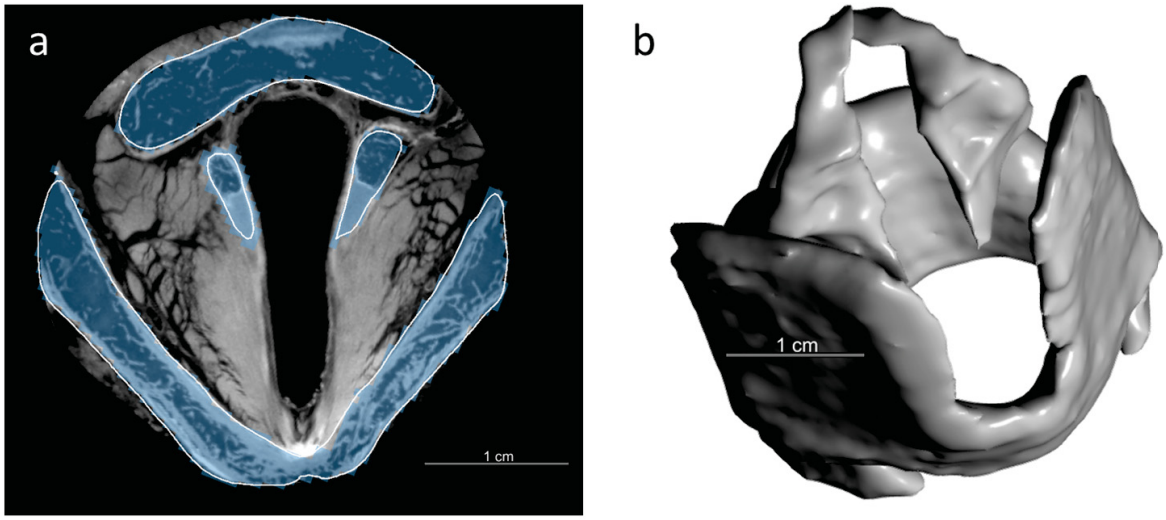

Figure 4–4: 3D model creation with manual segmentation from the H-F scan. (a) Manually segmented cartilages, with segmentation shown in blue, from one example plane in the transverse view. The smoothed mesh is shown in white. (b) 3D rendering of smoothed mesh from the manually segmented cartilages.

Manual segmentation was also used to create segmented training data to attempt automatic segmentation of the images. Results from automated deep learning segmentation with a U-Net architecture performed on 50 central slices, with 4 slices entered as training data, are shown in Figure 4–5. These slices can be corrected and used as input into another round of automated segmentation. Increasing the number of slices will require additional extensive computational resources.

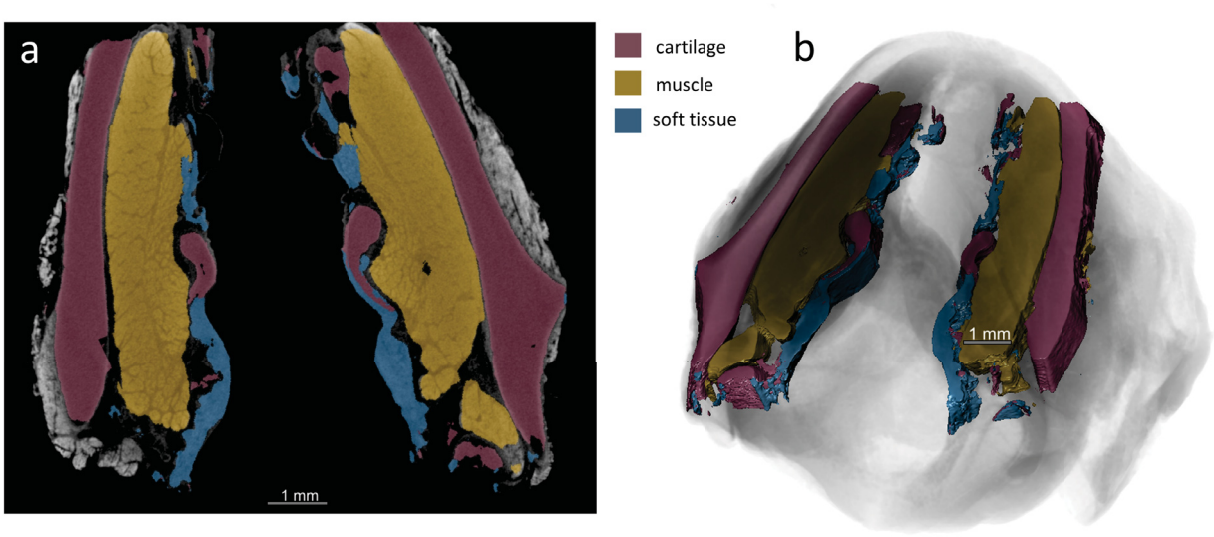

Figure 4–5: Automatic U-Net segmentation results for the rabbit larynx from the R-CS scan. (a) An example automatically segmented slice in the coronal plane. The soft tissue shows high error, while muscle and cartilage are largely recognized. (b) 3D rendering of the automatically segmented slice volumes, shown as smoothed meshes.

The results shown demonstrate the feasibility of segmenting high-resolution CT images of larynges for creation of computational models. Improved segmentation will facilitate more realistic computational simulations and bioprinting approaches. Segmented tissue structures, in combination with information from mechanical studies such as rheology, enable the creation of realistic structures for fluid-structure-acoustic analyses. These can be used to simulate the feedback between fluid pressures, structural deformations, and the energy in the acoustic response in the process of phonation.

CHAPTER 5
Visualizing vocal fold injury in a rabbit model

Information from studies of laryngeal anatomy, including the information presented in the previous chapter, can inform the development of animal models of vocal fold scar and motivate study design improvements. Many studies have been undertaken to characterize the effectiveness of various candidate treatments for vocal fold scarring, including injectable biomaterials and tissue engineering approaches; topical medicines such as growth factors and steroids; and cell therapy. Some treatments are developed to scaffold or promote proper vocal fold wound healing to recapitulate healthy extracellular matrix structure and limit fibrosis; others are meant to aid remodeling of already scarred tissue. Small animal models including rats [27], ferrets [49], and rabbits are used to evaluate immune response to the treatment, and as an initial indicator of efficacy in treatment or prevention of vocal fold scar. Rabbits are often chosen because they have larger vocal folds than rats, facilitating phonomicrosurgery. They continue to be a frequently used small animal model, selected in over 30 vocal fold injury studies published since 2002.

5.1 Past rabbit studies

Rabbit studies of vocal fold scarring typically have a timeline similar to that shown in Figure 5–1, consisting of an initial injury, a treatment applied either immediately after injury or following scar development, and treatment efficacy assessed with imaging, biochemical, or mechanical methods.

To examine the existing literature, 36 studies of rabbit vocal fold scarring (with or without treatment) published from 2002 up to March 2019 were found by searching the Google Scholar database with keywords including “vocal fold”, “scarring”, and “rabbit”/“leporine”. The study design shared in these publications is summarized in Table 5–1. The table shows the year and citation of the publication; instrumentation (Injury type) used to create the

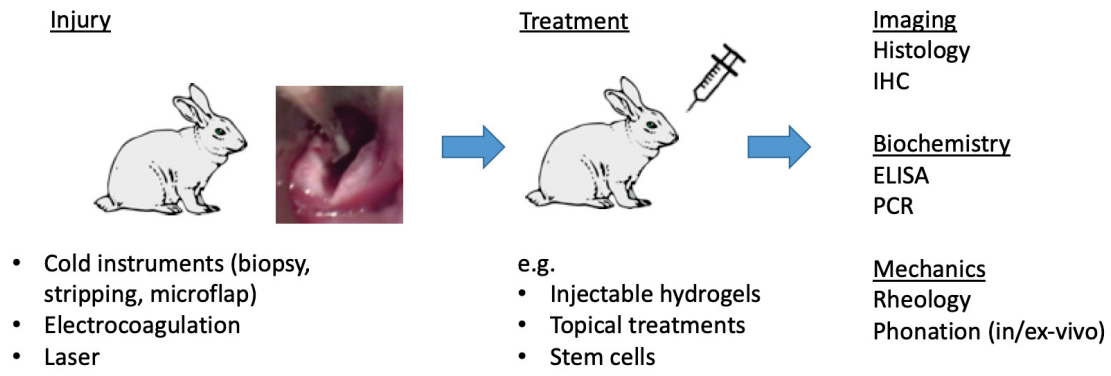

Figure 5–1: Common rabbit study protocols. Injury, treatment, and analysis methods as applied in rabbit studies of vocal fold scarring.

injury; sacrifice timepoints (Endpoint); the timepoint at which treatment is initiated or immediately (Imm) if treatment was conducted on the same day as injury (Tx day); the number of animals involved (#); whether vocal folds were injured unilaterally (1) or bilaterally (2); treatment type (Tx) broadly classified into injectable hydrogel (hydrogel), cell therapy (cell), tissue engineering (tissue), and other named approaches; and analysis methods broadly classified into histology (Hist), immunohistochemistry (IHC), rheology or rheometry (Rheol), biochemical methods including enzyme-linked immunosorbent assays, mRNA levels, PCR, and fluorescence in situ hybridization, and functional analysis with in vivo or ex vivo phonation (Phon). One study [182] also used atomic force microscopy to investigate collagen ultrastructure.

The goal of collecting the methodology used in the literature was to identify a predominant scarring model and analysis pipeline applied in rabbit studies of vocal fold injury and treatment. The literature search, however, revealed a wide diversity in methodological choices, complicating the comparison of results between studies. Most of the studies incorporating treatment reported success of their treatment method in their animal model. However, the lack of unified comparison metrics means that the effectiveness and drawbacks of treatment methods cannot be readily compared objectively with each other, contributing to fragmentation in the field.

Table 5–1: Vocal fold scarring studies, 2002-2019

Year	Citation	Injury type	Endpoint	Tx day	#	Side	Tx	Hist	IHC	Rheol	Biochem	Phon
2002	[183]	3 mm microforceps	1,3,5,10,15 days	n/a	11	1	none		X			
2002	[38]	3 mm biopsy forceps	60 days	n/a	11	1	none	X		X		
2002	[184]	2 mm microcup forceps	20 weeks	10 weeks	20	2	hydrogel	X				
2003	[185]	3 mm biopsy	60 days	n/a	10	1	none		X			
2004	[186]	3 mm microforceps	6 months	n/a	18	1	none	X		X		
2004	[69]	3 mm forceps biopsy	3,5,10,15 days	n/a	28	1	none		X		X	
2004	[187]	3 mm microforceps	6 months	imm	20	1	growth factor	X		X		
2005	[65]	microcup forceps	12 hours and 1,3,5,7,10,14,21 days	n/a	32	1	none	X				
2005	[188]	stripping	1,5,7,10,14,21 days	n/a	18	1	none	X			X	
2005	[189]	2 mm Jako cup forceps	21-24 days	imm	33	2	hydrogel	X		X	X	
2006	[190]	2 mm Jako cup forceps	1,3,5,10 days	imm	22	2	hydrogel				X	
2006	[191]	2 mm Jako cup forceps	20-21 days	imm	42	2	hydrogel			X	X	
2007	[192]	microcup forceps and microscissors	4 weeks	imm	11	1	cell	X	X	X	X	
2008	[193]	1 mm microforceps	2,4,8,24,48,72 hours	n/a	30	2	none				X	
2008	[194]	2 mm Jako cup forceps	1,3,5,10,21 days	imm	25	2	hydrogel				X	
2008	[195]	2 mm forceps biopsy	5 months	imm	20	2	cell, hydrogel	X	X			
2009	[196]	3 mm microforceps	10 days	imm	20	1	vitamin A	X				
2009	[197]	2 mm microcup forceps and microscissors	4 weeks	imm	10	2	cell	X		X		
2010	[67]	2 mm x 2 mm puncture wound with knife	3,7 days	imm	12	2	steroid	X				
2010	[63]	1.5 mm microcup forceps	3 months	imm	11	2	cell	X	X	X	X	
2011	[198]	2 mm Jako cup forcep	6 months	imm	12	2	hydrogel			X	X	
2012	[199]	3 mm microflap	2 weeks	n/a	10	1	none	X	X		X	
2013	[200]	2 mm microcup forceps and microscissors	3 months	imm	40	2	cell, hydrogel	X		X	X	
2013	[66]	microflap	7,30,90 days	imm	37	2	fibrin glue, sutures	X				
2014	[201]	electrocoagulator	8 weeks	imm	24	2	tissue	X			X	X
2014	[56]	3 mm microflap	0,1,3,5,7,30 days	n/a	30	1	none					X
2014	[202]	2.1 µm Holmium:YAG laser	4 weeks	n/a	8	1	none	X				X
2015	[203]	1.5 mm microcup forceps	3 months	imm	16	2	cell	X	X	X	X	
2016	[64]	40 mA electrocoagulation	6 weeks	imm	20	1	cell	X				X
2016	[62]	resection using Beaver blade	4 weeks	imm	8	1	tissue	X				X
2016	[53]	Hartmann ear forceps	18,21 months	3 months	74	2	cell	X				
2018	[204]	1 mm microforceps	9 months	imm	13	1	tissue	X				X
2019	[205]	980 nm diode laser	7 days	n/a	22	2	none	X				
2019	[206]	2 mm cup forceps	5,21 days	imm	54	1	hydrogel	X		X		
2019	[207]	1.5 mm microcup forceps and microscissors	2,4,24 days	imm	31	2	cell	X			X	
2019	[182]	2 mm biopsy forceps	6 months	3 months	12	1	cell	X	X			

Figure 5–2 shows the distribution of endpoints in studies examining vocal fold scarring with and without treatment. A disperse distribution is expected in early timepoints shorter than several weeks, as some studies investigate early wound healing responses such as inflammation. However, the dispersion of treatment study endpoints from several weeks to 21 months shows that no universally accepted endpoint emerges for testing the scarring prevention effectiveness of treatments. This signifies that different studies are testing their treatments at varying stages of scar maturity and levels of ECM remodelling.

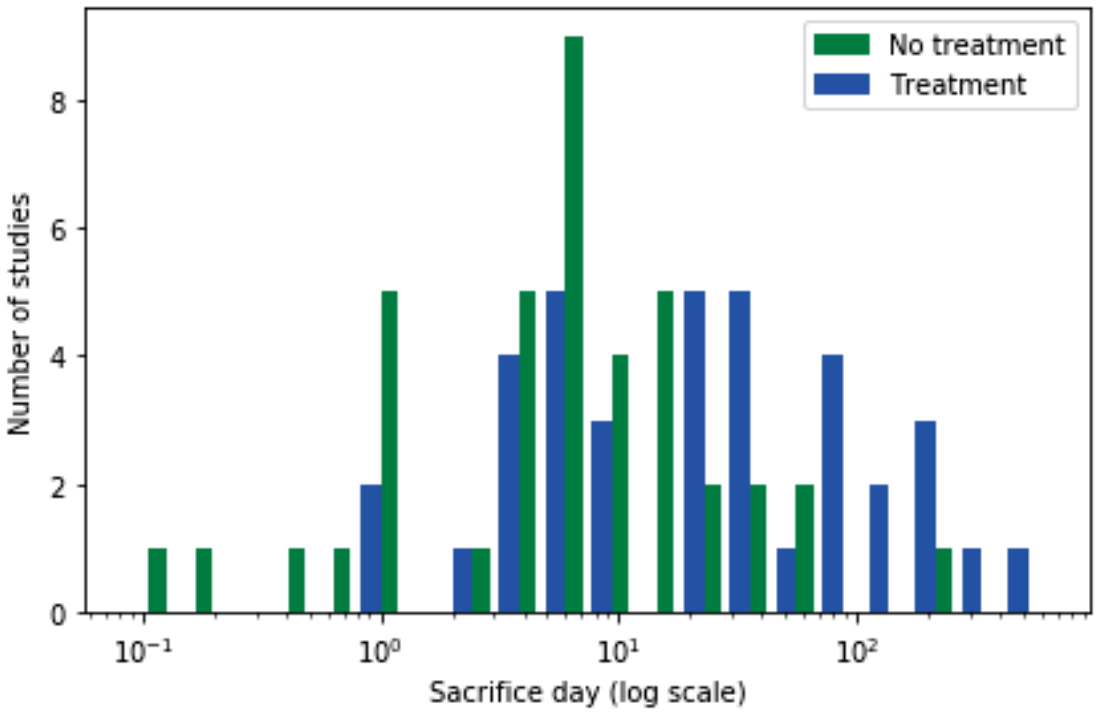

Figure 5–2: Sacrifice day distribution for rabbit vocal fold scarring studies, 2002-2019. For studies with more than one endpoint, all endpoints are considered separately. The timepoint axis is logarithmic.

The differences between injury methods also increase variability between studies. The injury was conducted frequently with cold instrument surgery. A total of 32 out of 36 studies reported various types of cold instrument surgery, with 26 of those using forceps such as biopsy or cup forceps. Two studies applied electrocoagulation, while two others used laser microsurgery. This is in line with the current paradigm in phonomicrosurgical intervention

for benign vocal fold lesions, with a growing transition to laser use [11]. Injury methods can also contribute to variability in the injuries experienced by animals in the same study. Cold instrument surgery with forceps can lead to varying defect size between animals in the pliable vocal fold tissue [202], exacerbated by limited visibility in some endoscope systems. Unilateral injury and bilateral injury were conducted with equal frequency. Bilateral injury was found to result in high rates of animal death in several studies, possibly due to throat obstruction following excessive inflammation. Two studies creating bilateral injuries resulted in the premature death of 20 animals in a cohort of 74 [53], and 8 prematurely dead of 42 [191]. This does not consider potential underreporting of premature deaths in other studies. The candidate treatment was applied immediately following injury in 21 of the 24 treatment studies, suggesting most studies were directed toward examining the prophylactic function of their treatment.

One factor contributing to the difficulty of interstudy comparison is that most of the methods for evaluating scarring extent and treatment efficacy employed in these studies require sacrifice of the animal, the exception being functional analysis by in vivo phonation in several studies. All imaging and biochemical analysis in the studies is conducted ex vivo. Incorporation of 3D virtual histology methods could serve as a step toward facilitating comparison between studies. Virtual histology methods that can be used in vivo, such as CT, MRI, and OCT/nonlinear endoscopy, could be performed multiple times within one study on the same animal. This would provide information at several timepoints, and would also give insight into the wound healing timeline for each animal, controlling for differences in injury defect size and location between animals. Virtual histology performed ex vivo, though it cannot contribute information in the time domain, can provide contextual spatial information to compare between animals and across studies. This can avoid slicing location and angle differences, and slicing-induced artifacts such as deformation.

5.2 Imaging results

This chapter reports the application of NM, CT, and MRI as virtual histology methods in studies of rabbit vocal fold injury and scarring. The animal study methods are described in Section 3.2, and results are drawn from specimens from each rabbit study.

5.2.1 Preliminary NM and CT results

The intention of the first study was to observe vocal fold scarring using nonlinear microscopy due to the label-free imaging potential for specific detection of fibrillar collagen due to its SHG emission property, and visualization of other structures such as elastin fibers and blood vessels by their intrinsic autofluorescence. Vocal fold scarring had previously been studied with SHG signal in rats [54, 208]. Previous rabbit studies had reported difficulties with slicing errors and artifacts, motivating a transition to 3D imaging, a strength of NM due to the infrared excitation wavelengths increasing penetration depth compared to visible wavelength range excitation. Solvent-based optical clearing with the uDISCO method was used to decrease scattering inside the tissue.

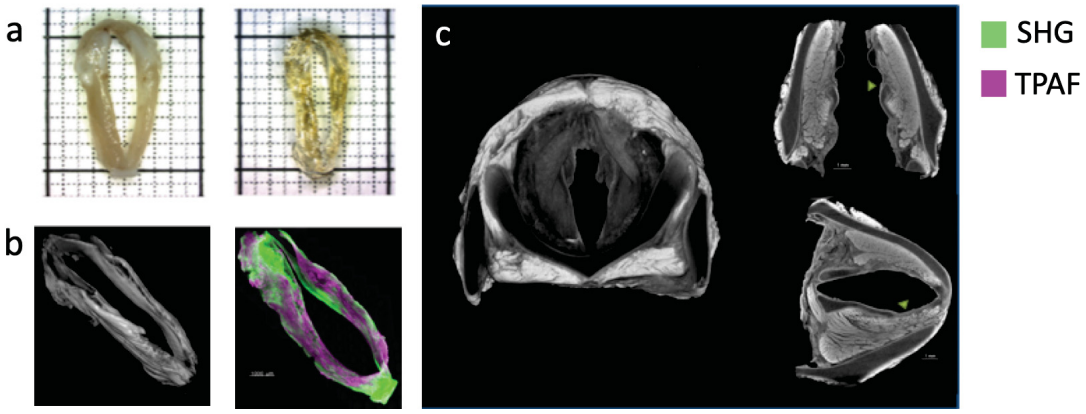

Figure 5–3: 3D imaging of rabbit vocal folds with CT and NM. (a) Dissected vocal folds before (left) and after (right) optical clearing. (b) 3D renderings of CT and NM imaging of the specimen shown above. (c) CT images of a rabbit larynx from a commercial source, clockwise from left showing a 3D view, coronal virtual slice, and transverse virtual slice. This scan was acquired at 12.4 µm resolution. The location of the vocal folds is shown with a green arrow in (c).

Figure 5–3a shows dissected fixed tissue and the same tissue rendered translucent following uDISCO optical clearing, with small scale bars corresponding to 1 mm; slight shrinkage was observed in the cleared tissue due to the dehydration steps in the clearing process. The tissue was dissected to a vertical dimension of 2 mm to match the working distance of the XLPLN25XWMP2 objective available on the FV1200MPE system.

Nonlinear microscopy was conducted on optically cleared samples, resulting in images of SHG and autofluorescence, shown in Figure 5–3b. High-resolution CT was also used on one of the samples to investigate feasibility of visualizing structure of interest, shown in Figure 5–3c. The preliminary imaging results from one specimen were presented in [21] to share the demonstrated feasibility of using NM prefaced by optical clearing for virtual histological investigation of rabbit vocal folds. There was, however, no scarring readily identifiable in these images for rabbits from saline-injected control nor from hydrogel-injected treatment groups, with no qualitatively obvious difference apparent between the injured right and uninjured left vocal folds. The degradation of signal quality with depth with nonlinear imaging due to insufficient correction with the water immersion objective for the refractive index of the immersion solvent BABB-D, approximately 1.56 [209], contributed to difficulty in qualitatively and quantitatively comparing the left and right vocal folds.

One potential explanation for the lack of evident scarring was that the modified microflap surgery technique may not have sufficiently disrupted the lamina propria, resulting in complete healing by the sacrifice 42 days post surgery regardless of treatment method. Complete wound healing with adequate tissue remodeling for the conventional microflap has been demonstrated at the two-week timepoint with H&E histology [199]. Another potential explanation was that the dissection size had resulted in the resection of injured areas of the tissues. To investigate the dissection method, an undissected, PTA stained rabbit larynx obtained from a commercial source was imaged with CT, with resulting images shown in Figure 5–3d. Qualitative observation of vocal fold size and morphology in this specimen suggested

that to guarantee the preservation of the vocal folds in their entirety, the dissection sample size must be increased beyond 2 mm.

To evaluate the applicability of NM and CT for virtual histology of vocal fold scarring, structures of interest were observed with the two methods, and the visualization obtained was compared with H&E standard histology images. Coronal virtual slices through vocal fold and adjoining cartilage as seen in NM and CT, compared with an H&E slice through vocal fold, are shown in Figure 5–4 for comparison. Both NM and CT revealed vocal fold lamina propria and the vocalis muscle, with the low fibrous density in the lamina propria and muscle fascicle morphology comparable to that shown in the H&E image. The SHG signal shows the higher concentration of fibrous collagen in the cartilage than the vocal fold. The stratified squamous epithelial layer is well delineated in the CT images and in the two-photon autofluorescence NM signal. The CT scan had isotropic resolution, so coronal virtual slices have the same resolution as transverse virtual slices. NM however was limited in vertical, or z-axis, resolution optically and in terms of scan time, resulting in lower resolution of coronal virtual slices due to the orientation of the tissue in scanning.

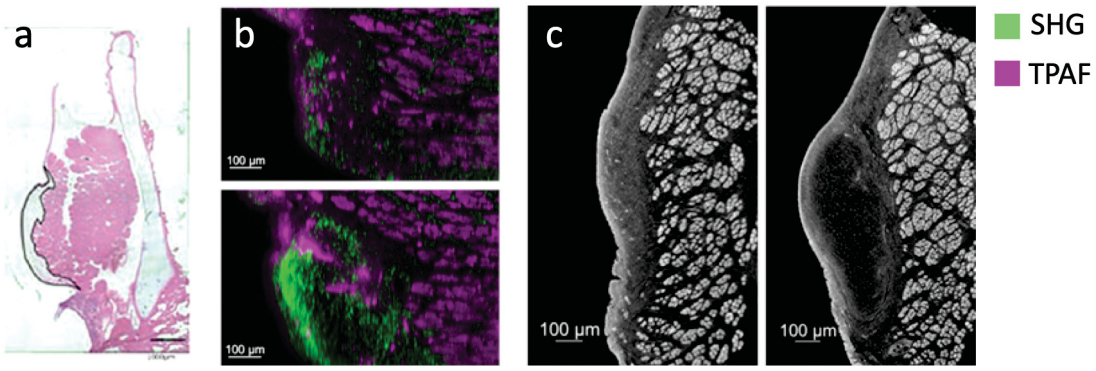

Figure 5–4: Coronal vocal fold slices from histology, NM, and CT. (a) H&E staining of a rabbit vocal fold, with lamina propria outlined in black. (b) Virtual slice from NM acquired at 640 nm (x,y) by 5 µm z resolution. Top image is sliced through vocal fold, bottom image sliced through cartilage. (c) CT at 800 nm voxel size. Left image represents vocal fold and right image represents cartilage.

The vocal fold lamina propria, cartilage, and muscle can also be observed with transverse virtual sections, with NM performing optimally in lateral resolution. These structures are

shown in Figure 5–5. The epithelial layer; collagen fibers in the lamina propria, cartilage, and muscle layer; blood cells within blood vessels; chondrocytes in the cartilage; and the striation of muscle are qualitatively identifiable in the NM images. Some fibrous structures are visible in the CT images as well, but they are not readily identifiable with the absorption-based signal. The epithelium, muscle fascicles, cartilage chondrocytes, and blood vessels can also be observed in the CT images. Each technique showed strengths and limitations: CT had the advantage of isotropic resolution and faster scanning time for equal area than NM, and NM provided specific label-free structural information at a resolution approaching the diffraction limit in the imaging plane.

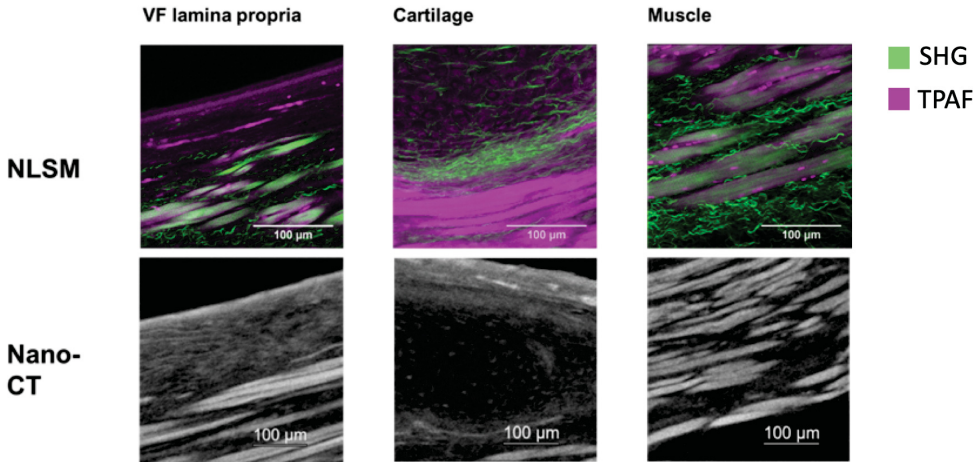

Figure 5–5: Representative images of laryngeal tissue structures visualized with NM and CT. In the NM images, resolution down to 248 nm is attained in (x,y). In the CT images, resolution down to 800 nm is attained in (x,y,z).

Functional analysis

Animals in this study were designated for either investigation of vibratory function with ex vivo phonation, or for nonlinear microscopy imaging to investigate microstructural changes in scarring. One of the specimens preserved following functional analysis was stained with PTA and underwent CT as well, to attempt to visualize differences between the left injured and right control vocal folds. The image is shown in Figure 5–6; no defects were visible in a still image extracted from the high-speed video recording, nor on the CT image virtual slices.

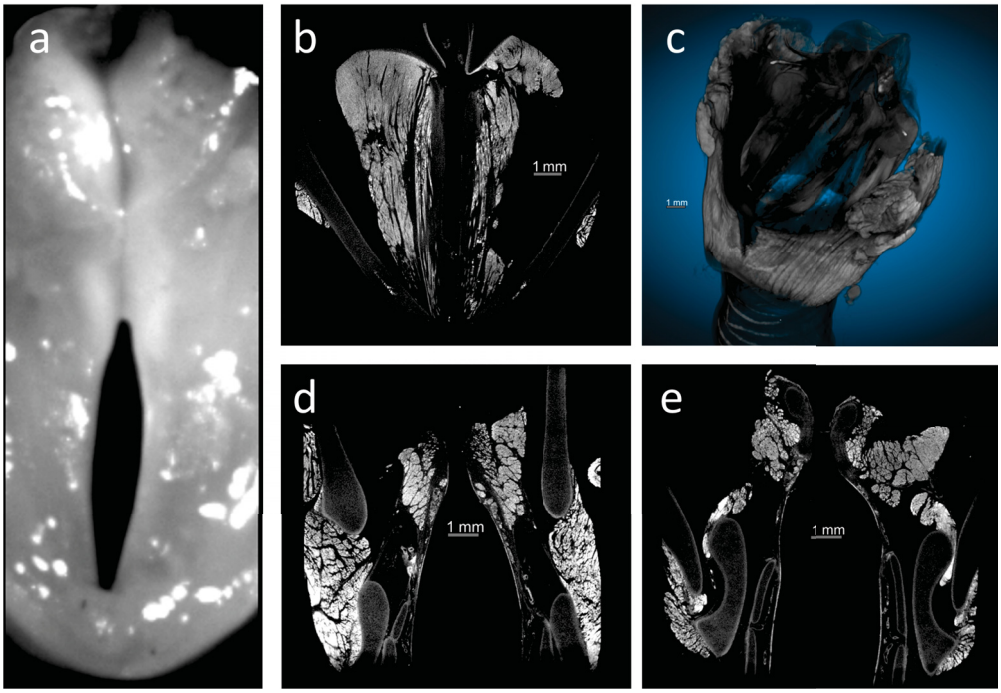

Figure 5–6: Illustration of the function anatomy dissection structure. This rabbit was treated with dexamethasone, a corticosteroid. (a) Still from a high-speed video acquisition, courtesy of Lei Xi Christina Chen. (b) Transverse view. (c) 3D view. (d) Coronal view through vocal fold location. (e) Coronal view through the arytenoid cartilages.

5.2.2 Injury timepoint study MRI and CT results

Preliminary qualitative results with NM and CT showed that these modalities were capable of detecting structures of interest for studies of vocal fold injury and scarring, including fiber architecture, epithelial integrity, and blood vessels. The reason that scarring locations were not clearly identified remained unclear. Potential factors included dissection protocol, injury method, and sacrifice timepoint; the cause could also be multifold, comprising several factors. To obtain a better understanding of the scarring phenotype to expect and look for in NM and CT analysis, an injury timepoint study was designed. MRI and CT were chosen as imaging methods to use prior to dissection for NM, due to their accommodation of larger sample sizes. The images acquired from these methods could then be used to inform dissection into a sample size appropriate for NM. The additional motivation for using MRI and CT was as an ex vivo test for potential future development of an in vivo imaging protocol

to use in vocal fold scarring studies. In vivo imaging capability would mean that animals could be imaged with the same method multiple times within one study, contributing longitudinal wound healing and remodeling results. It could also mitigate the problems caused by differences in injury severity and individual wound healing capability between animals, and facilitate comparison between studies. MRI had previously been used for in vivo determination of acute vocal fold injury and ex vivo determination of vocal fold scar in rats [104].

The sacrifice timepoints were set based on closely related studies chosen within the vocal fold wound healing and scarring literature. The injury method used was surgical excision with microcup forceps. One rabbit was sacrificed at the late inflammation stage of 3 days; one rabbit was sacrificed at the early remodeling stage of 10 days; and a third rabbit was sacrificed at the 39 day timepoint for mature scar formation and comparison with the images acquired in the previous animal study in which all rabbits were sacrificed at 42 days.

Figure 5–7 summarizes MRI and CT results of the three excised rabbit larynges prior to dissection for NM. The rabbit sacrificed at 3 days following surgery showed inflammation on the MRI scan, with a large defect from the injury. For this rabbit, in surgery the injured vocal fold location was not successfully removed, and the large mass seen is possibly the remaining flap of tissue that can be seen in the endoscopy video still. The rabbit sacrificed at 10 days post surgery had evidence of reepithelialization, a surgical excision defect, and possible swelling. The rabbit sacrificed at 39 days post surgery showed a mature deficiency scar. Contraction of the injury location resulted in the sharp triangular coronal shape of the left vocal fold as compared to the healthy, rounded right vocal fold.

MRI samples were imaged in PBS, which provided sufficient contrast with the soft tissue, though better contrast could be achieved with immersion in an MR-inert solution. The highest resolution attempted for MRI of the samples was 100 µm isotropically, with the 300 µm scan not providing sufficient visualization of the defect, and the 200 µm resolution sufficient to clearly identify inflammation and deficiency. Cartilage, muscle, and soft tissue,

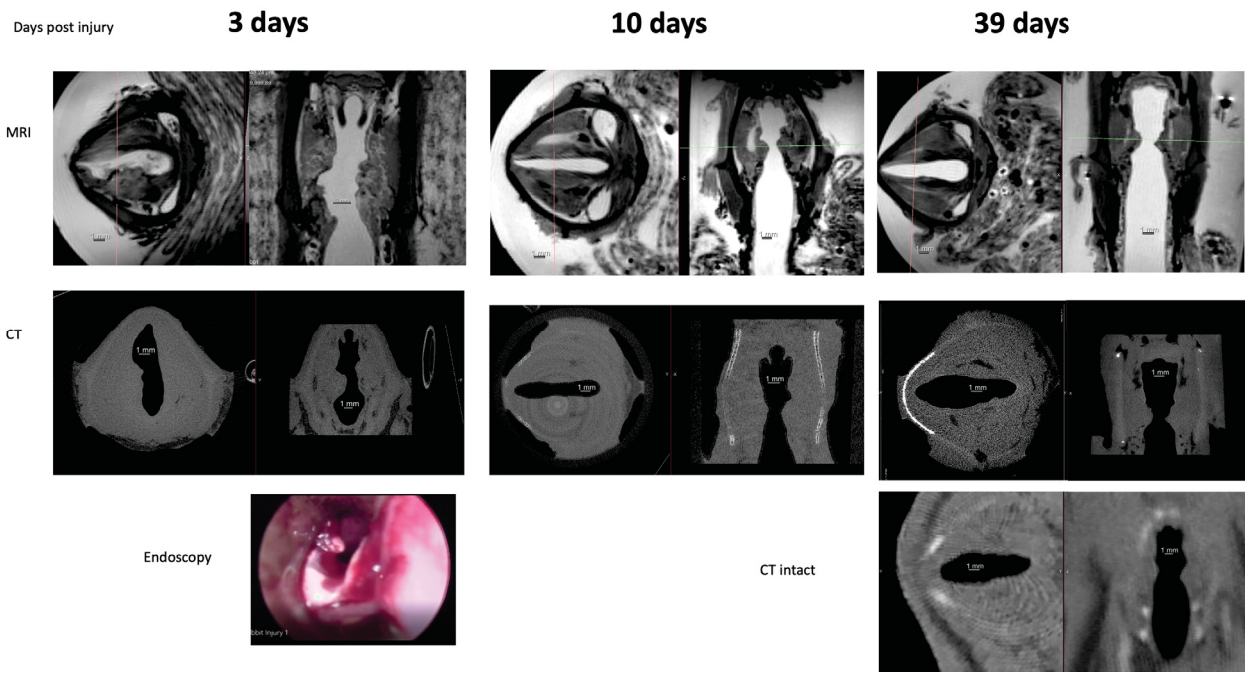

Figure 5–7: MRI and CT of rabbits sacrificed at different timepoints. At day 3, inflammation was observed with MRI at the location of the deficiency. At day 10, the asymmetry of the vocal folds is visible with both MRI and CT. At day 39, the mature scar with increased density is seen with MRI. The scarred vocal fold has a triangular shape in the coronal view, compared to the rounded healthy vocal fold. The defect shape is visible in the excised larynx CT as well as the intact rabbit CT, though for the intact animal higher resolution scanning may be desired.

and signs of reepithelialization can all be identified on the 200 µm MRI scan. Identifying reepithelization is an important feature, as some low viscosity or slow-thickening injectable treatments may need to await reepithelialization to ensure the material remains within the tissue rather than leaking out.

MRI and absorption CT were both able to identify the injury in ex vivo dissected samples, and MRI allowed identification of features of interest for vocal fold scarring. The information extractable from MRI motivates future in vivo trials to evaluate the feasibility in vivo MRI longitudinally within a rabbit vocal fold injury and treatment study. Because CT is a lower-cost method and often is more accessible than MRI, absorption CT may also be considered as a method to identify gross features such as the size of a defect or inflammation; injection of a contrast agent may also improve the acquired images. Image registration with

previously obtained higher-quality CT or MRI images, of the same animal or others, could also help with identification of features or understanding changes in pathological states.

5.2.3 MRI image processing

Image registration was used to evaluate defect formation in MRI images. Defect size can be evaluated by comparison to the uninjured vocal fold on the same animal. The image registration result for the rabbit sacrificed at 39 days is shown in Figure 5–8a. The registration was performed with a resulting sum of squared differences of 0.024, with qualitatively accurate fit evaluated using the laryngeal cartilages as anatomical landmarks. The deficiency is visually well defined in the registered image.

The MRI scans of the injured vocal folds also provided an opportunity for creating 3D prints of the intact larynx prior to dissection for NM. The 3D printed larynx of the same rabbit is shown in Figure 5–8c, in comparison with a coronal virtual slice shown in Figure 5–8b. 3D printing of these models was completed only after dissection for NM in this study. Creation of such models prior to dissection could provide additional planning opportunities for dissection, and with the selection an appropriate printing material the model could be used to practice dissection.

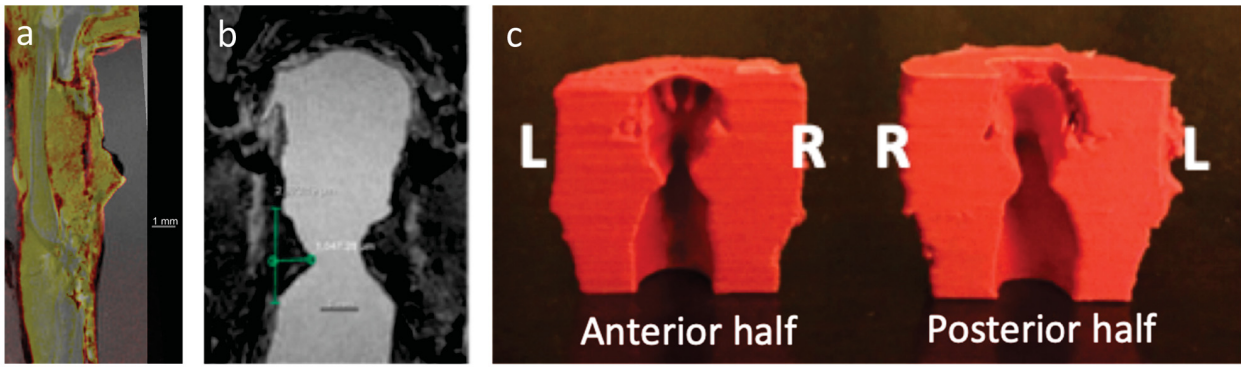

Figure 5–8: MRI image processing. (a) Image registration between the left and right vocal folds of the rabbit sacrificed at 39 days, with the healthy vocal fold shown in greyscale and the scarred vocal fold overlaid with the Fire lookup table. (b) A coronal view of the vocal folds. (c) 3D printed model. The segmented area was created by intensity thresholding followed by manual correction. The resulting mesh was then smoothed, converted to G-code, and printed with the Prusa i3 MK3 in PLA material. The scar defect can be seen in the shape of the left vocal fold.

5.2.4 Injury timepoint study NM results

In light of the MRI and CT results demonstrating that the size of the rabbit true vocal folds were larger than 2 mm in the coronal dimension, a different microscope and objective were chosen for continuing studies of the vocal folds to accomodate a larger dissected sample. The XLSPLN255XGMP glycerol-immersion objective on the FVMPE-RS system had an 8 mm working distance, and offered refractive index correction closer to the refractive index of the BABB-D clearing solution.

A preliminary scan on a healthy rabbit larynx showed promise of using this system, shown in Figure 5–10. The FVMPE-RS system available however had only an epi-illumination configuration, collecting only backward directed two-photon autofluorescence and SHG. Due to the forward directionality of SHG, this resulted in low SHG with minimal signal acquired as depth increased. To collect forward emission of SHG, a mirror was introduced under the sample. Glass slides and cover slips were sputter coated with aluminum to reflect the SHG and autofluorescence signals into the objective [117], resulting in dramatic signal improvement of SHG as shown in Figure 5–9 for a human skin tissue control slide.

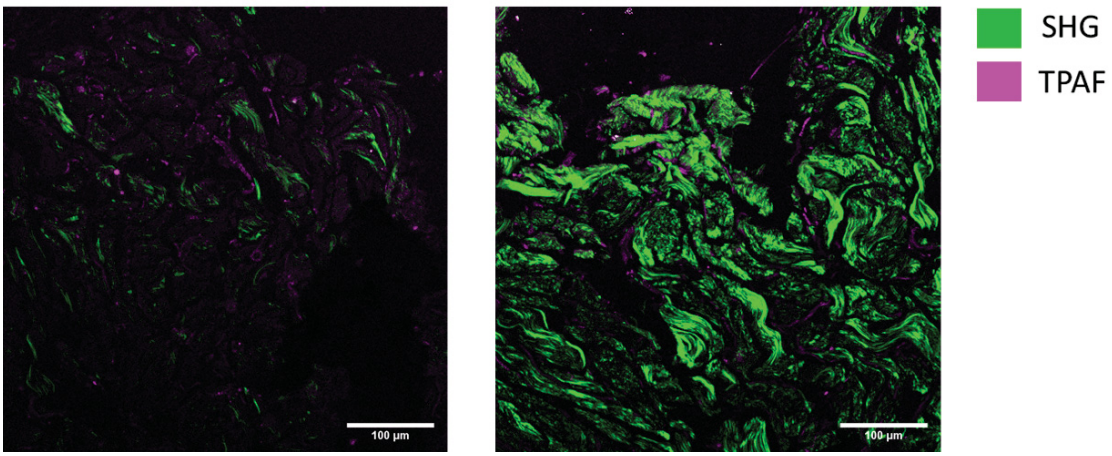

Figure 5–9: Images of a human skin tissue control slide (Tissue-Trol, Sigma-Aldrich), without (left) and with (right) an aluminum-coated coverglass below the imaging location. The autofluorescence signal increased moderately by a factor of 1.1, while the SHG signal increased by a factor of 3.0.

In sample preparation for NM imaging, the objective was to dissect the samples to the smallest size possible while ensuring vocal folds were fully intact. Figure 5–10 shows the dissection and optical clearing results for the three rabbits. The vocal folds of the rabbit sacrificed at 10 days were cut in dissection due to not accounting for the diagonal spread of the vocal folds in the coronal place. This resulted in two 3-4 mm slices containing vocal fold structures. The rabbits sacrificed at 3 and 39 days were successfully dissected with vocal folds remaining intact. These two samples were conservatively dissected to thicknesses approximating 6 mm. The samples before and after uDISCO optical clearing are shown in Figure 5–10. The full thickness samples decreased in opacity, which is especially apparent in thinner locations in the sample. They were, however, not sufficiently clear to make optical sectioning and signal acquisition through the whole sample realistic on the multiphoton setup. The half-thickness rabbit 2 sample showed extremely good clearing, resulting in a translucent specimen with minimal scattering throughout the sample.

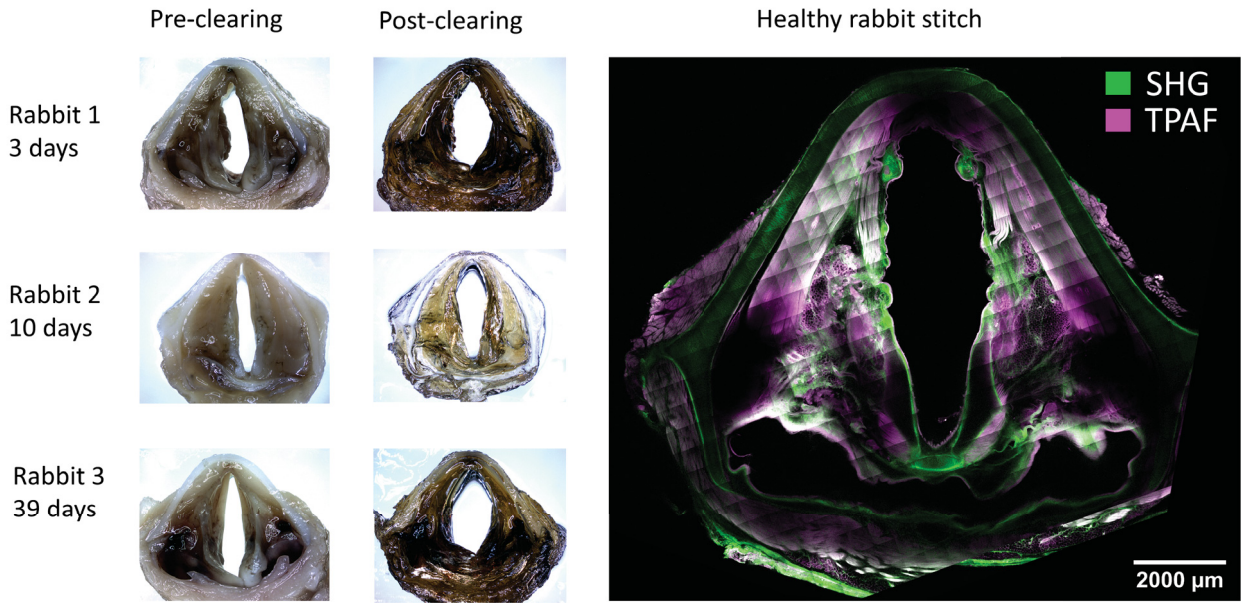

Figure 5–10: Results from optical clearing for the rabbits sacrificed at 3, 10, and 39 days. The mucosa can be observed in the pre-clearing images, while in the post-clearing images is greatly retracted due to dehydration. The right image shows a stitched image at one height, above the true vocal folds, in a healthy rabbit larynx showing the distribution of tissues within the sample.

The anisotropic shrinkage induced by dehydration prior to immersion in BABB-D solution can be clearly seen in all three samples. The glottis appears much larger in the cleared tissue due to shrinkage of the water-rich vocal fold tissue. This morphological change increases the difficulty of identifying soft tissue structures. Tissue structures visualized in the rabbit sacrificed 39 days post injury are shown in Figure 5–11. A candidate scar location was identified using the scarring hallmarks of tissue contraction and collagen disorganization. The loss of signal with increasing penetration depth, however, meant that signal was not clear through the entirety of the lamina propria. To improve this, the sample will first be reimaged upside down, and the images will be combined through image fusion to improve signal. If this is not sufficient to identify scar and obtain sufficient data for quantitative analysis of collagen morphology and organization, the sample will need to be altered more dramatically. This could include clearing with a different optical clearing method that will allow deeper penetration, or sample slicing into several smaller sections.

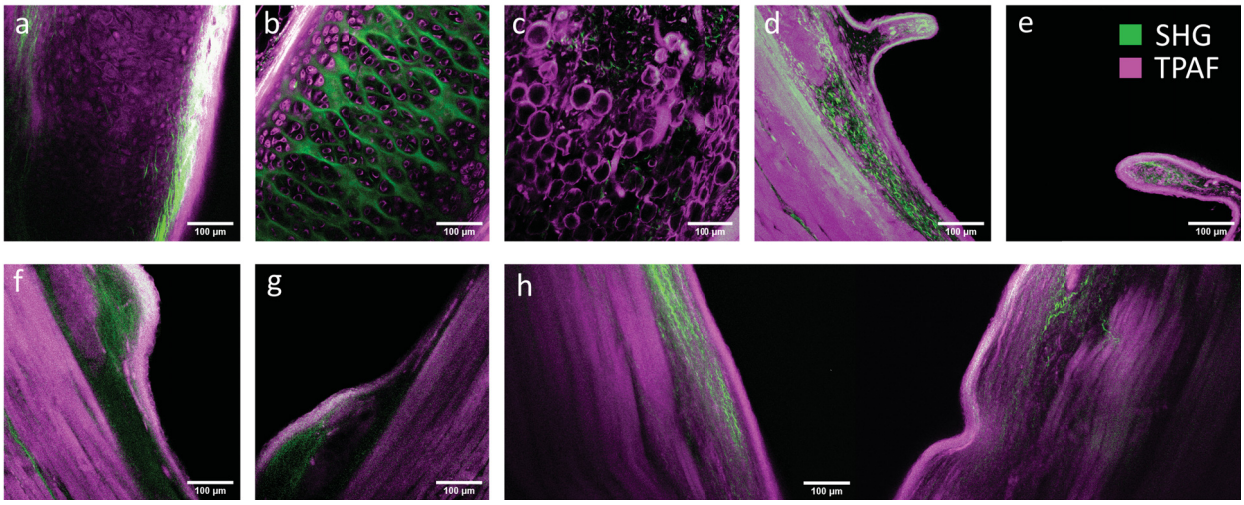

Figure 5–11: Features of interest in NM scans of the rabbit sacrificed at 39 days. The x,y pixel size was 994 nm, and then z pixel size was 50 µm. (a) Elastic cartilage structure of the arytenoid cartilage. (b) Hyaline cartilage structure of the thyroid cartilage. (c) Fat tissue. Planar outfoldings in the right (d) and left (e) vocal folds. Gland tissue located above the right (f) and left (g) vocal folds. (h) Transverse view of the vocal folds, right then left clockwise. There is a potential scar location seen in the injured vocal fold, with signs of collagen disorganization and tissue contraction.

5.2.5 Quantitative fiber analysis

A main advantage of using NM to study scarring is the specific label-free observation of fibrillar collagen due to its SHG emission. Given sufficient signal and resolution, the multiphoton autofluorescence of elastic fibers can be observed concurrently. In scarring, the disorganization of collagen and elastin fibers is predicted, as well as increases in collagen and decreases in elastin. The application of quantitative fiber analysis methods is desired to increase efficiency and objectivity in analysis of NM images. One challenge for extracting quantitative information from NM images of intact tissue is that increased scattering with increasing depth leads to decreases in signal strength and quality. This decrease is not easily corrected or compensated for because of variations in tissue thickness and opacity throughout the tissue. This motivates the use of methods that do not rely on intensity, and instead use morphometry to quantify fiber amount and organization. Such morphometric methods decrease bias induced by differences in signal strength in addition to providing information on fiber organization.

Three morphometric analysis methods were selected for application on simulated and real images: two ensemble methods (ICS, Fourier analysis) and one fiber extraction and fitting methods (CT-FIRE). Simulated images were created with linear and wavy collagen fibers to evaluate the impacts of fiber morphology on the analysis outcomes. Images of linear fibers were used as a first control for the analysis due to the easily interpretable power spectral density and spatial autocorrelations of such images. In addition, analysis of linear fibers can be applicable for collagen gels are formed in vitro, as the resulting fibers are largely linear. To closer approximate the collagen fiber morphology seen in SHG vocal fold tissue images, wavy collagen fibers were simulated using a sine function. The crimping of collagen fibers in the vocal folds is evident in 5–5. Collagen fiber crimping helps the tissue handle mechanical stress, as the tissue can straighten out under tensile stress without stretching or breaking the fibers. Both line and wave simulations allowed definition of fiber length distribution, orientation distribution, and thickness distribution. The wavy fibers had additional input

parameters defining sine wave amplitude and period. Analysis was performed on a real SHG image obtained from the tunica media layer of the aorta wall, and on simulated line and wave images meant to approximate the orientation distribution of the real image.

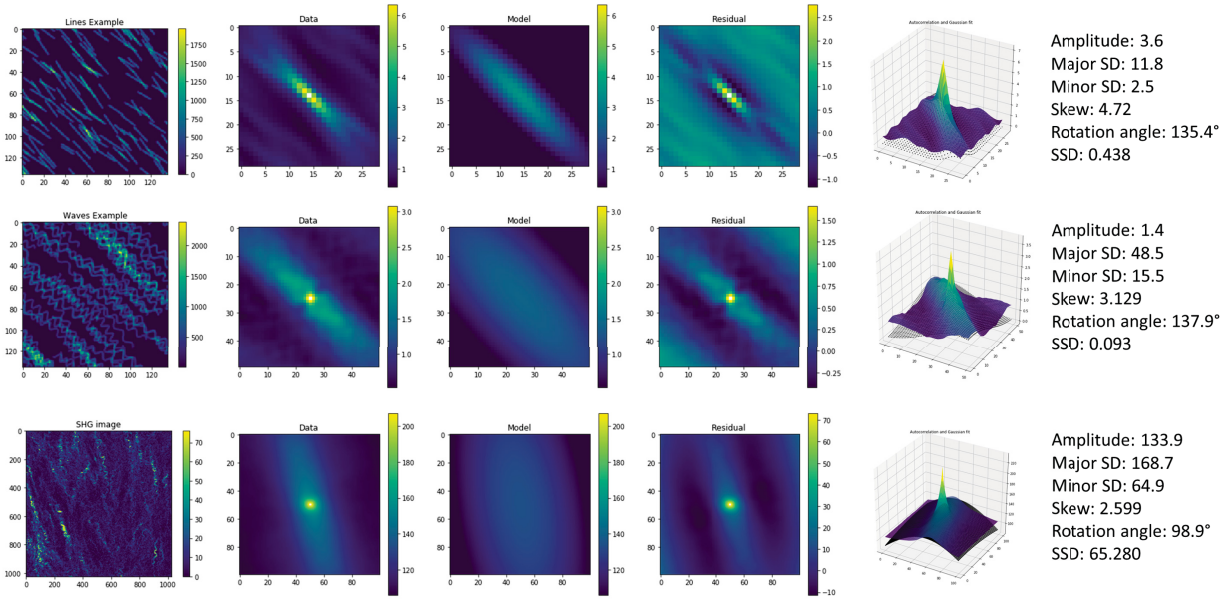

Figure 5–12: Spatial image correlation spectroscopy analysis demonstrated on simulated line and wave images with orientation uniformly distributed between 120-150 degrees, and a real image of tissue from the media layer of the aorta. The aortic tissue sample is shown courtesy of Meisam Asgari. The autocorrelation function was cropped and fit with a 2D elliptical Gaussian function. The 3D plot shows the fitting of the cropped image autocorrelation function (surface) with the Gaussian (points).

Figure 5–12 shows the results from spatial ICS analysis. The spatial autocorrelation function was taken of each image, and cropped at the center to facilitate fitting at low spatial lag. The noise-containing zero lag value at the center was maxed for fitting. The 2D elliptical Gaussian fit performed well for the image of lines, but broadened for the wave simulated and real images. This broadening could result in the underestimation of the skew, which can be normalized to an image with known parameters as a measure of fiber length. The broadening of the autocorrelation, likely related to the period and amplitude of the waves, has to be considered when analyzing images from real tissue. The orientation was successfully recapitulated for both simulated images, and a realistic orientation value was obtained for the real image as well.

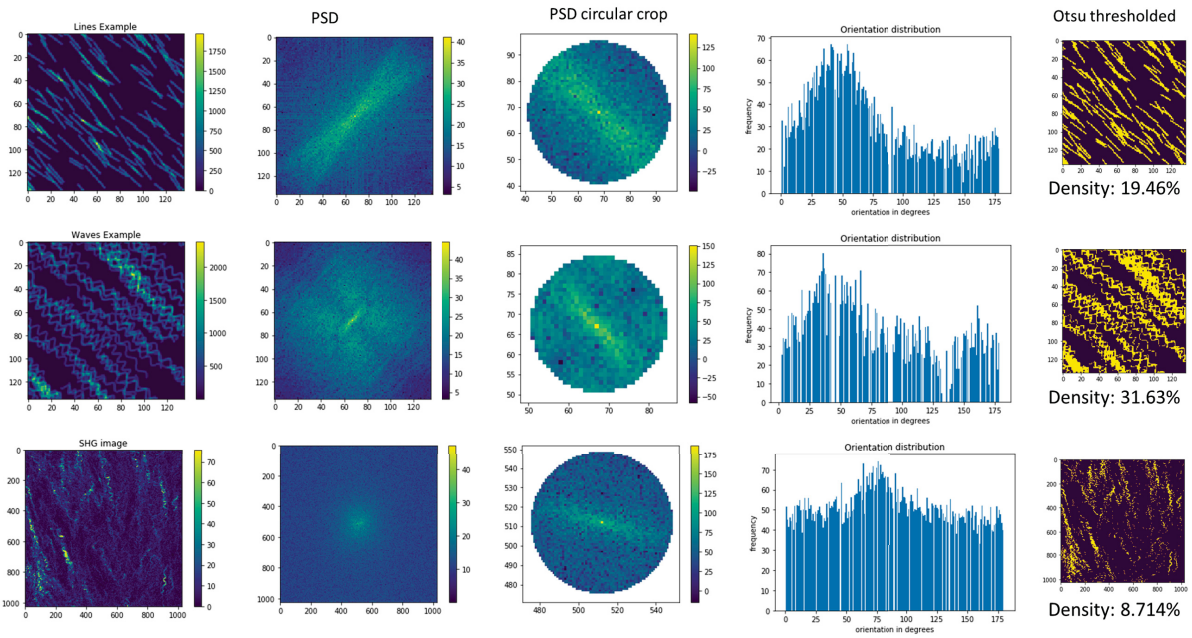

Figure 5–13: Fourier power spectral analysis demonstrated on simulated line and wave images, and a real image of tissue from the media layer of the aorta. The power spectral density (PSD) of the image was taken and cropped circularly at the center. The orientation distribution histograms shown are median-subtracted for improved visualization. The images processed with Otsu thresholding provide an estimate of fiber density.

Figure 5–13 shows results obtained from analyzing the power spectral density (PSD) of the simulated and real images. Qualitative observation of the PSD for the simulated line image shows broadening resulting from the distribution of orientations. The PSD for the simulated wave image shows increased spectral density in a winged orientation perpendicular to the assigned fiber orientations, suggesting that the period and amplitude of the waves could be extracted by analyzing the distribution off of the preferred orientation axis. The PSD of the real image more closely resembles that of the linear fibers, potentially suggesting that the wave period and amplitude are not sufficiently uniform in this image to observe the perpendicular enrichment in the power spectrum. The PSD images were cropped circularly at the center to ensure all orientations would be compared equally following their transformation into polar coordinates. The resulting orientation distributions provided similar results to that obtained from ICS with a 90° offset, which is expected as they are Fourier transform pairs. In addition, the orientation distribution histogram provided an estimation

of anistropy; flatter histograms following median subtraction correspond to more anisotropic images. Otsu thresholding was included in the Fourier analysis protocol due to its inclusion in the motivating paper [160], though it is not specific to this method. Binary thresholding provided an estimation of density in each of the images, corresponding to the percentage of pixels preserved following the thresholding function.

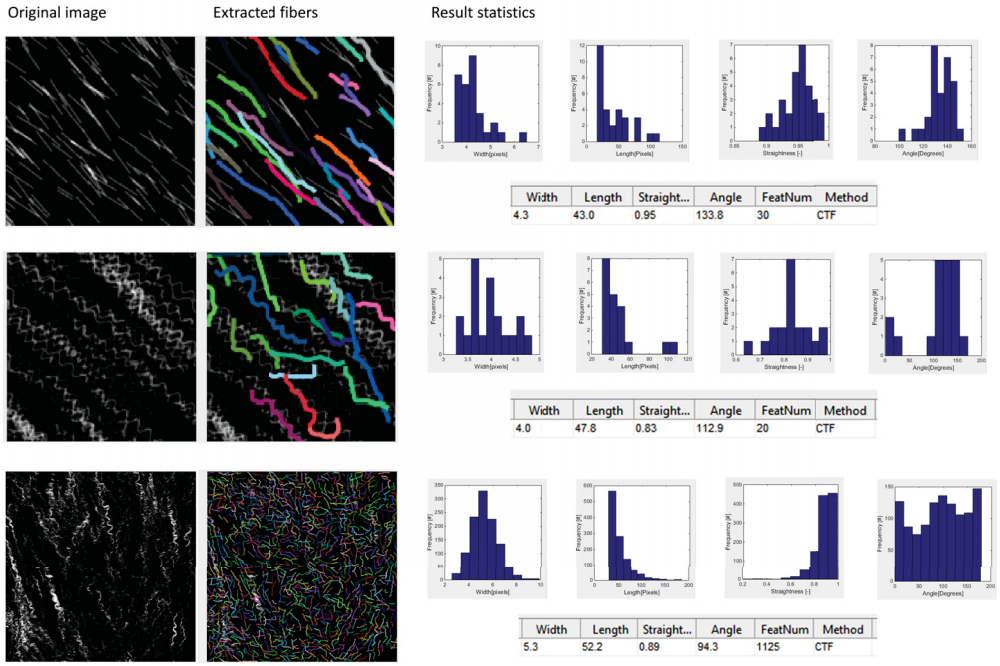

Figure 5–14: CT-FIRE analysis demonstrated on simulated line and wave images, and a real image of tissue from the media layer of the aorta. The images of fibers, and the fibers as found by CT-FIRE, are shown. Histograms summarize the distribution of length, width, straightness, and angle for the extracted fibers. The average value of each of those parameters is also shown.

Figure 5–14 shows results from CT-FIRE analysis. The extracted fibers are shown in colors, and the distributions of length, width, straightness, and angles of these extracted fibers are shown in histogram form. The average orientation was well captured for the simulated line and real images. The morphology of the linear fibers was fit well in terms of straightness and alignment, but the method suffered with recapitulating the crimped fibers in the simulated wavy fiber and real images. The results evaluated the promise of ICS, Fourier analysis, and CT-FIRE for simulated and real test images. However, to quantitatively

analyze the changes in collagen and elastin distribution in scarring in the rabbit vocal fold injury experiment, better quality images will need to be obtained in scarred and unscarred vocal fold lamina propria. Improved visualization can be obtained via different mechanisms, whether by improving clearing, using image fusion of the image from each direction, finer dissection, or slicing the sample for smaller 3D volumes or 2D analysis.

CHAPTER 6
Discussion

The motivation of this work was to contribute to imaging investigations of laryngeal structure using constrast-enhanced absorption-based CT imaging, and evaluate MRI, CT, NM, and accompanying image analysis methods for application to a rabbit vocal fold injury and scarring study. In Chapter 4, CT images were acquired to visualize laryngeal structures in human, rabbit, guinea pig, and rat specimens, and preliminary image processing was attempted to demonstrate feasibility of creating 3D computational models incorporating soft tissue features. In Chapter 5, MRI, CT, and NM were used to visualize rabbit vocal fold structure, and MRI and CT probed wound healing over time in a rabbit vocal fold scarring model.

For CT imaging, PTA staining provided sufficient absorption contrast enhancement to observe soft tissue structure in the human and animal larynges imaged. The creation of anatomical atlases from additional specimens with different traits would allow patient scans to be compared with atlases that have similar traits such as age or sex, reducing bias introduced by the preferential use of specimens of certain demographics [210] and increasing the specificity of comparison results. In terms of model building, the absorption images acquired were of appropriate quality for segmentation and 3D mesh creation, as evaluated by results shown in this work for manual segmentation of cartilages from subsampled images, and automated segmentation of a thickness of 50 CT slices. To improve the segmentation results, more accurate training segmentation is required, in addition to additional computation resources and the application of data reduction methods such as autoencoder models. The CT images of rabbit larynges provided information to the injury study, informing better understanding of the anatomy and required dissection size to preserve the full vocal folds.

The rabbit vocal fold injury imaging project showed feasibility of MRI, CT, and NM for studies of vocal fold scarring. The preliminary investigations demonstrated acquisition of NM images in optically cleared rabbit vocal fold tissue, though importantly lacking any findings of scarring. The following study, with three rabbits sacrificed at different timepoints in the wound healing process, showed the development of scar at 39 days as seen with MRI and CT. The information acquired with MRI and CT illustrated the utility of applying techniques compatible with large sample sizes prior to dissection. The MRI of rabbit larynges exhibited soft tissue feature visualization without any contrast enhancement, motivating future investigations of its in vivo application for rabbit vocal fold injury studies. The MRI was also used for 3D printing, showing that it can be applied for dissection planning. Because a larger dissection size than originally anticipated was required, the dissected sample was bigger than the working distance available on the forward detection NM system available. This required the use of a different microscope only equipped with backward detection, greatly reducing SHG signal observed. An aluminum-coated mirror slide however greatly improved the signal obtained by SHG and allowed imaging deeper within the sample. The uDISCO dehydration and solvent immersion-based optical clearing method was selected for its shrinkage properties as well as its fluorescence preservation. The shrinking of tissues was anticipated to decrease the scanning time required. This optical clearing method, however, had unanticipated consequences, as the dehydration of NM samples led to anisotropic tissue shrinkage. This shrinkage deformed the vocal folds and complicated the localization of the area of interest during image acquisition and analysis. Improvement of the sample preparation and imaging protocol will be required to obtain useful NM images, localize scarring, and apply fiber analysis methods. This study however has so far shown the use of applying MRI as a first ex vivo approach, demonstrated scar formation at the 39 day time point with MRI, and shown the potential of NM for visualizing features of interest given adequate signal and resolution. This study also evaluated analysis methods, showing that image registration can be used on MRI images to compare the injured and uninjured

vocal folds. It also showed in simulation and real images that ICS, Fourier analysis, and CT-FIRE can provide useful information for NM analysis with morphological metrics useful for analyzing scarring hallmarks.

Another important consideration in these studies was the type of injury done in the animal model. Differences in injury method cause disparate wound healing timelines and outcomes. Each type of injury also has its own level of precision and replicability achievable in injury size and severity. The injury method used in the first study was a modified microflap technique. The conventional vocal fold microflap elevation does not leave a scar in rabbits [199], which motivated incorporating additional tissue disruption. This modified microflap approach had the advantage of being similar to the microflap method often used in human phonosurgery, and compared to excision injuries is preferred for injectable treatments as they can be introduced into the lamina propria and remain within the tissue without flowing out. This surgery method is, however, not yet fully tested, as there was no scar observed in the samples – this could be a function of the surgery method, dissection method, or other causes. It may be however favorable to develop an injury method that is more damaging and does not heal quickly, as the purpose is to evaluate treatments for scarring. In the injury timepoint study, the injury method used was a microcup forceps biopsy to ensure that sufficient tissue disruption occurred. This excision method is, however, not very replicable, because the vocal fold tissue is pliable, and is torn in the excision process unless the forceps are sharp enough to cut the vocal folds reliably. Another option to consider is applying laser microsurgery to the lamina propria for repeatable wound creation [202]. This, however, creates a thermal injury. Cold instrument surgery is still often used clinically, and the wound healing responses are likely different between the two injury types, meaning they may require different treatment approaches. The development of a replicable cold instrument surgical injury method may thus still be required to evaluate wound healing and treatment intervention efficacy for scarring inflicted by cold instruments and more generally mechanical traumas.

Table 6–1 shows a comparison of the approximate resolution and contrast mechanism obtained from the imaging modalities discussed in this work. Resolution varies between systems. This information can be used to help select the appropriate imaging modalities when designing a new study.

Table 6–1: Imaging methods comparison

Imaging method	**Resolution**	**Contrast**
CT	0.8-150 µm	density, atomic number
MRI	100 µm	spin relaxation
confocal microscopy	0.2-1 µm	fluorescence
NM	0.2-1 µm	autofluorescence, harmonic generation
OCT	1 mm	refractive index
ultrasound	1 mm	acoustic impedance

Overall the objective of obtaining laryngeal anatomy images was met, with some progress toward creating computational models achieved. More work will, however, be required to create usable models incorporating soft-tissue information. This work also evaluated MRI, CT, and NM as methods for studies of rabbit vocal fold injury. It showed that MRI provided imaging of wound healing and scar formation, and that NM could provide useful, quantitative information but requires careful consideration in the processes of sample preparation and microscopy setup.

6.1 Recommendations for future work

Various short-term and long-term avenues of further study emerge from these projects and other works ongoing in the fields of laryngeal structure and modeling, and treatment development for vocal fold scarring. For the creation of improved models, automated segmentation can be applied with additional computational resources and increased amounts of manually segmented training data to feed the segmentation networks. Image quality could be improved by using a synchrotron x-ray source, though such facilities are currently limited in availability. Phase contrast imaging would also provide soft tissue structure visualization without the requirement of staining; stained samples imaged with phase contrast could provide additional information as well. Absorption CT contrast, however, still provides useful

information, as x-ray attenuation can be related to the density of a material using scans at multiple energies with calibration measurements of the Compton scattering coefficient and the energy weighting ratio of the system [211, 212]. Density can also be measured with phase contrast imaging by introducing phase and analyzer gratings into the system [213]. This could be applied for example to 3D printing, as the materials used to print can take into account the measured density values extracted from the CT images. Additional information could also be extracted by integrating information obtained from CT, MRI, and NM information with image fusion for true multimodality imaging. This could incorporate gross structure from CT down to the collagen distribution from NM. Combined with rheology to obtain the mechanical properties of the tissues, such images could provide information for 3D bioprinting with soft materials exhibiting mechanical properties and organization similar to tissue. Such advances may make it possible to improve in vitro models of vocal fold scarring with spatial and biomechanical information [55], as well as inform 3D bioprinting and tissue engineering of the larynx. Such models would include cells such as vocal fold fibroblasts, and matrices for cells to inhabit and interact with. This will work toward a transition in which in vitro models may be more similar to human physiology than laboratory animals because of the differences in microstructure between species. These types of imaging and analysis approaches would also improve computational flow structure acoustic interaction models, as they would contribute a realistic response of the tissue to applied forces. As more powerful computational resources become available, this type of analysis would become feasible.

This work also motivates contributions to methodology in vocal fold injury that are conducted ex vivo, following sacrifice. First, vocal fold injury visualization was demonstrated with MRI in the rabbit model. Images from MRI could be used for planning and practicing dissection with 3D printed models. Image registration could compare the healthy and injured vocal folds in the same specimen, or facilitate comparison between specimens. Contrast enhancement with gadolinium for MRI imaging potentially would improve the signal and information acquired. Imaging with stained or phase contrast CT could also provide

microstructural information. An interesting approach to test would be stain reversal of PTA and iodine stains, to see if sufficient stain reversal can be achieved for successful optical clearing and NM. Other emerging methods include dual-energy CT, which uses energy discriminating x-ray detectors to visualize multiple targets, and improving contrast as both density and atomic number of the tissue can be characterized [214]. The use of NM remains appealing because of it observation of fibrillar collagen and elastin. It could also be applied in conjunction with optical clearing to observe human vocal fold samples and evaluate their microstructure. One consideration is the optical clearing method used for studying rabbit vocal folds. The uDISCO solvent-based method is advantageous in terms of sample shrinkage for faster imaging time, smaller resultant sample size, and fluorescence preservation. The anisotropic shrinkage of vocal fold tissue, however, results in deformations that complicate image interpretation. Human vocal folds are larger and easier to identify and specifically dissect than rabbit and other rodent vocal folds, meaning that uDISCO may be an appropriate method for such studies. For rabbit vocal folds, water-based clearing methods could be evaluated instead, or intermodal image registration of the deformed, cleared tissue NM images to MRI or CT images of unprocessed tissue can be attempted to restore the physiological morphology. Other optical clearing methods may also result in greater opacity decrease than uDISCO, which would provide additional improvement as it would mitigate the loss of signal with increasing depth. Nonlinear light sheet microscopy, rather than point laser-scanning microscopy, would provide faster scanning to obtain more location information in a shorter amount of time. Innovative methods such as expansion microscopy could also be used to get better definition of small parts [215]. With appropriate signal obtained from SHG and autofluorescence, it will be possible to use ICS, Fourier analysis, CT-FIRE, and wave fitting to analyze the NM images and obtain information on collagen and elastin distributions. The analysis methods can also be elaborated. For example, the period and amplitude could potentially be estimated using the power spectral density of wavy images. Additional preprocessing could improve analysis results, and would be useful for images that

contain structures other than lamina propria, for example muscle fibers, to remove the impact of those signals. With high-resolution 3D information it will also be advantageous to implement 3D versions of ICS, Fourier analysis, CT-FIRE, and wave fitting techniques to characterize fibers not oriented in the plane of the 2D images or virtual sections.

Another important research direction for studies of vocal fold scarring is the development of techniques and protocols for in vivo vocal fold injury visualization. In vivo analysis would decrease the number of animals required in a study to reach statistical significance as the variability problem would be minimized. It would also allow each wound to be followed over time, mitigating the uncertainties introduced by differential injury severity between animals. Promising results were delivered with MRI in ex vivo scans, motivating a trial of its use for in vivo analysis of rabbit vocal fold injury and scarring. Contrast enhancement with gadolinium could be introduced if sufficient resolution is not obtained in a reasonable amount of time due to movement artifacts. It is also often easier to access a CT, motivating trials of using contrast enhanced absorption CT or phase contrast CT if available to visualize injury and scarring. The NM results acquired so far show clear SHG signal from fibrillar collagen, motivating its use for in vivo scar imaging. Improvement of NM endoscopy methods, and the advent of commerical NM endoscopes, will mean that information will be acquired on extracellular matrix components such as collagen and elastin in situ. The observation of the uppermost layer, the superior lamina propria, would already provide useful information due to its importance in the vibratory function of the vocal folds. With the advent of adaptive optics, it may become possible to obtain useful information from greater depths in the tissue as well [216]. Technological development to improve imaging and analysis methods will provide higher resolution volumetric information from multiple modalities that can be combined by image fusion, facilitate the creation of highly realistic computational and bioprinted models, and decrease the number of animals required in studies of vocal fold scarring by improving feasibility of monitoring scar formation and wound healing in live animals.

References

[1] Amir K Miri. Mechanical characterization of vocal fold tissue: a review study. *Journal of Voice*, 28(6):657–667, 2014.

[2] Jon B Suzuki and Randolph R Resnik. Wound dehiscence: Incision line opening. In *Misch's Avoiding Complications in Oral Implantology*, pages 402–439. Elsevier, 2018.

[3] Mioko Fukahori, Shun-ichi Chitose, Kiminori Sato, Shintaro Sueyoshi, Takashi Kurita, Hirohito Umeno, Yu Monden, and Ryoji Yamakawa. Regeneration of vocal fold mucosa using tissue-engineered structures with oral mucosal cells. *PloS one*, 11(1):e0146151, 2016.

[4] Tomáš Gregor, Petra Kochová, Lada Eberlová, Lukáš Nedorost, Eva Prosecká, Václav Liška, Hynek Mírka, David Kachlík, Ivan Pirner, Petr Zimmermann, et al. Correlating micro-ct imaging with quantitative histology. In *Injury and skeletal biomechanics*. IntechOpen, 2012.

[5] Bettina Weigelin, Gert-Jan Bakker, and Peter Friedl. Third harmonic generation microscopy of cells and tissue organization. *J Cell Sci*, 129(2):245–255, 2016.

[6] Olaf Ronneberger, Philipp Fischer, and Thomas Brox. U-net: Convolutional networks for biomedical image segmentation. In *International Conference on Medical image computing and computer-assisted intervention*, pages 234–241. Springer, 2015.

[7] Sylvia Krischke, Susan Weigelt, Ulrich Hoppe, Volker Köllner, Michael Klotz, Ulrich Eysholdt, and Frank Rosanowski. Quality of life in dysphonic patients. *Journal of Voice*, 19(1):132–137, 2005.

[8] Regina Helena Garcia Martins, Henrique Abrantes do Amaral, Elaine Lara Mendes Tavares, Maira Garcia Martins, Tatiana Maria Gonçalves, and Norimar Hernandes Dias. Voice disorders: etiology and diagnosis. *Journal of voice*, 30(6):761–e1, 2016.

[9] Katherine Verdolini and Lorraine O Ramig. Occupational risks for voice problems. *Logopedics Phoniatrics Vocology*, 26(1):37–46, 2001.

[10] Nelson R Williams. Occupational groups at risk of voice disorders: a review of the literature. *Occupational medicine*, 53(7):456–460, 2003.

[11] Robert T Sataloff and Christopher J Hartnick. *Sataloff's Comprehensive Textbook of Otolaryngology: Laryngology*, volume 6. JP Medical Ltd, 2016.

[12] Jennifer K Hansen and Susan L Thibeault. Current understanding and review of the literature: vocal fold scarring. *Journal of Voice*, 20(1):110–120, 2006.

[13] Jacqui Allen. Cause of vocal fold scar. *Current opinion in otolaryngology & head and neck surgery*, 18(6):475–480, 2010.

[14] Shigeru Hirano. Current treatment of vocal fold scarring. *Current opinion in otolaryngology & head and neck surgery*, 13(3):143–147, 2005.

[15] M Graupp, S Bachna-Rotter, C Gerstenberger, G Friedrich, E Fröhlich-Sorger, K Kiesler, and M Gugatschka. The unsolved chapter of vocal fold scars and how tissue engineering could help us solve the problem. *European Archives of Oto-Rhino-Laryngology*, 273(9):2279–2284, 2016.

[16] C Gaelyn Garrett, John R Coleman, and Lou Reinisch. Comparative histology and vibration of the vocal folds: implications for experimental studies in microlaryngeal surgery. *The Laryngoscope*, 110(5):814–824, 2000.

[17] Diane M Bless and Nathan V Welham. Characterization of vocal fold scar formation, prophylaxis and treatment using animal models. *Current opinion in otolaryngology & head and neck surgery*, 18(6):481, 2010.

[18] Michael Senter-Zapata, Kunal Patel, Pinky A Bautista, Molly Griffin, James Michaelson, and Yukako Yagi. The role of micro-ct in 3d histology imaging. *Pathobiology*, 83(2-3):140–147, 2016.

[19] Warren R Zipfel, Rebecca M Williams, Richard Christie, Alexander Yu Nikitin, Bradley T Hyman, and Watt W Webb. Live tissue intrinsic emission microscopy using multiphoton-excited native fluorescence and second harmonic generation. *Proceedings of the National Academy of Sciences*, 100(12):7075–7080, 2003.

[20] Shigeru Hirano, Sachiko Minamiguchi, Masaru Yamashita, Tsunehisa Ohno, Shin-ichi Kanemaru, and Morimasa Kitamura. Histologic characterization of human scarred vocal folds. *Journal of Voice*, 23(4):399–407, 2009.

[21] Alexei Kazarine, Ksenia Kolosova, Angelica A Gopal, Huijie Wang, Rui Tahara, Almoaidbellah Rammal, Karen Kost, Luc Mongeau, Nicole YK Li-Jessen, and Paul W Wiseman. Multimodal virtual histology of rabbit vocal folds by nonlinear microscopy and nano computed tomography. *Biomedical Optics Express*, 10(3):1151–1164, 2019.

[22] Amir K Miri, Umakanta Tripathy, Luc Mongeau, and Paul W Wiseman. Nonlinear laser scanning microscopy of human vocal folds. *The Laryngoscope*, 122(2):356–363, 2012.

[23] J Manoharan Prakash. Whats special in a child's larynx? *Journal of pharmacy & bioallied sciences*, 7(Suppl 1):S55, 2015.

[24] Hideto Saigusa. Comparative anatomy of the larynx and related structures. *Japan Med. Assoc. J*, 54:241–247, 2011.

[25] Yutaka Toya, Napaporn Riabroy, Christopher R Davis, Yo Kishimoto, Sherry A Tanumihardjo, Diane M Bless, and Nathan V Welham. Interspecies comparison of stellate

cell-containing macula flavae and vitamin a storage in vocal fold mucosa. *Journal of anatomy*, 225(3):298–305, 2014.

[26] Allison L Maytag, Mark J Robitaille, Adam L Rieves, James Madsen, Benjamin L Smith, and Jack J Jiang. Use of the rabbit larynx in an excised larynx setup. *Journal of Voice*, 27(1):24–28, 2013.

[27] Tomoko Tateya, Jin Ho Sohn, Ichiro Tateya, and Diane M Bless. Histologic characterization of rat vocal fold scarring. *Annals of Otology, Rhinology & Laryngology*, 114(3):183–191, 2005.

[28] Abir K Bhattacharyya and Nupur Kapoor Nerurkar. *Laryngology*. Thieme, 2014.

[29] MP Fried and M Tan. Clinical laryngology: The essentials. *The Journal of Laryngology & Otology*, 129:110, 2015.

[30] Kiminori Sato, Minoru Hirano, Shigejiro Kurita, and Kensuke Kiyokawa. Distribution of elastic cartilage in the arytenoids and its physiologic significance. *Annals of Otology, Rhinology & Laryngology*, 99(5):363–368, 1990.

[31] Sharon S Tang, Vidisha Mohad, Madhu Gowda, and Susan L Thibeault. Insights into the role of collagen in vocal fold health and disease. *Journal of Voice*, 31(5):520–527, 2017.

[32] Tomoko Tateya, Ichiro Tateya, and Diane M Bless. Collagen subtypes in human vocal folds. *Annals of Otology, Rhinology & Laryngology*, 115(6):469–476, 2006.

[33] Jaime Moore and Susan Thibeault. Insights into the role of elastin in vocal fold health and disease. *Journal of Voice*, 26(3):269–275, 2012.

[34] Roger W Chan, Steven D Gray, and Ingo R Titze. The importance of hyaluronic acid in vocal fold biomechanics. *Otolaryngology-Head and Neck Surgery*, 124(6):607–614, 2001.

[35] Steven D Gray, Ingo R Titze, Roger Chan, and Thomas Hale Hammond. Vocal fold proteoglycans and their influence on biomechanics. *The Laryngoscope*, 109(6):845–854, 1999.

[36] Keiko Ishikawa and Susan Thibeault. Voice rest versus exercise: a review of the literature. *Journal of voice*, 24(4):379–387, 2010.

[37] Ryan C Branski, Katherine Verdolini, Vlad Sandulache, Clark A Rosen, and Patricia A Hebda. Vocal fold wound healing: a review for clinicians. *Journal of voice*, 20(3):432–442, 2006.

[38] Susan L Thibeault, Steven D Gray, Diane M Bless, Roger W Chan, and Charles N Ford. Histologic and rheologic characterization of vocal fold scarring. *Journal of Voice*, 16(1):96–104, 2002.

[39] Bernard Rousseau, Shigeru Hirano, Troy D Scheidt, Nathan V Welham, Susan L Thibeault, Roger W Chan, and Diane M Bless. Characterization of vocal fold scarring in a canine model. *The Laryngoscope*, 113(4):620–627, 2003.

[40] Michael S Benninger, David Alessi, Sanford Archer, Robert Bastian, Charles Ford, James Koufman, Robert T Sataloff, Joseph R Spiegel, and Peak Woo. Vocal fold scarring: current concepts and management. *Otolaryngology—head and neck surgery*, 115(5):474–482, 1996.

[41] Xinxin Liu, Tanaya Walimbe, William Pierre Schrock, Wei Zheng, and M Preeti Sivasankar. Acute nanoparticle exposure to vocal folds: A laboratory study. *Journal of Voice*, 31(6):662–668, 2017.

[42] Mark S Courey, C Gaelyn Garrett, and Robert H Ossoff. Medial microflap for excision of benign vocal fold lesions. *The Laryngoscope*, 107(3):340–344, 1997.

[43] Clark A Rosen. Vocal fold scar: evaluation and treatment. *Otolaryngologic Clinics of North America*, 33(5):1081–1086, 2000.

[44] Stellan Hertegård, Åke Dahlqvist, Claude Laurent, Assunta Borzacchiello, and Luigi Ambrosio. Viscoelastic properties of rabbit vocal folds after augmentation. *Otolaryngology–Head and Neck Surgery*, 128(3):401–406, 2003.

[45] Dinesh K Chhetri and Abie H Mendelsohn. Hyaluronic acid for the treatment of vocal fold scars. *Current opinion in otolaryngology & head and neck surgery*, 18(6):498–502, 2010.

[46] Tanaya Walimbe, Alyssa Panitch, and Preeti M Sivasankar. A review of hyaluronic acid and hyaluronic acid-based hydrogels for vocal fold tissue engineering. *Journal of Voice*, 31(4):416–423, 2017.

[47] L Hallen, C Johansson, and C Laurent. Cross-linked hyaluronan (hylan b gel): a new injectable remedy for treatment of vocal fold insufficiency-an animal study. *Acta Oto-Laryngologica*, 119(1):107–111, 1999.

[48] A Mattei, J Magalon, B Bertrand, C Philandrianos, J Veran, and A Giovanni. Cell therapy and vocal fold scarring. *European annals of otorhinolaryngology, head and neck diseases*, 134(5):339–345, 2017.

[49] Haruka Kodama, Yoshihiko Kumai, Kohei Nishimoto, Yutaka Toya, Satoru Miyamaru, Shinobu Furushima, and Eiji Yumoto. The ferret as a surgical model for vocal fold scar creation and treatment. *Annals of Otology, Rhinology & Laryngology*, 127(3):146–154, 2018.

[50] Gayle Woodson. Developing a porcine model for study of vocal fold scar. *Journal of Voice*, 26(6):706–710, 2012.

[51] Tsunehisa Ohno, Shigeru Hirano, Shin-ichi Kanemaru, Masaru Yamashita, Hiroo Umeda, Atsushi Suehiro, Yoshihiro Tamura, Tatsuo Nakamura, Juichi Ito, and Yasuhiko Tabata. Drug delivery system of hepatocyte growth factor for the treatment of vocal fold scarring in a canine model. *Annals of Otology, Rhinology & Laryngology*, 116(10):762–769, 2007.

[52] Diane M Bless, Nathan V Welham, Shigeru Hirano, Hiromi Nagai, Douglas W Montequin, Bernard Rousseau, and Charles N Ford. Growth factor therapy for vocal fold scarring in a canine model. *Annals of Otology, Rhinology & Laryngology*, 113(10):777–785, 2004.

[53] Angelou Valerie, Kalodimou Vassiliki, Messini Irini, Psychalakis Nikolaos, Eleftheria Karampela, and Papalois Apostolos. Adipose-derived mesenchymal stem cells in the regeneration of vocal folds: a study on a chronic vocal fold scar. *Stem cells international*, 2016, 2016.

[54] Alexei Kazarine, Sarah Bouhabel, Annie H Douillette, Karen Kost, Nicole YK Li-Jessen, Luc Mongeau, and Paul W Wiseman. Multimodal imaging of vocal fold scarring in a rabbit model by multiphoton microscopy. In *Multiphoton Microscopy in the Biomedical Sciences XVII*, volume 10069, page 100692E. International Society for Optics and Photonics, 2017.

[55] M Graupp, B Rinner, MT Frisch, G Weiss, J Fuchs, M Sundl, A El-Heliebi, G Moser, LP Kamolz, M Karbiener, et al. Towards an in vitro fibrogenesis model of human vocal fold scarring. *European Archives of Oto-Rhino-Laryngology*, 275(5):1211–1218, 2018.

[56] Tsuyoshi Kojima, Joshua R Mitchell, C Gaelyn Garrett, and Bernard Rousseau. Recovery of vibratory function after vocal fold microflap in a rabbit model. *The Laryngoscope*, 124(2):481–486, 2014.

[57] Robert Hermans and Carlo Bartolozzi. *Imaging of the larynx*. Springer Verlag, 2001.

[58] Frederik G Dikkers and Peter GJ Nikkels. Benign lesions of the vocal folds: histopathology and phonotrauma. *Annals of Otology, Rhinology & Laryngology*, 104(9):698–703, 1995.

[59] Brian H Brown, Rod H Smallwood, David C Barber, PV Lawford, and DR Hose. *Medical physics and biomedical engineering*. CRC Press, 2017.

[60] Tim D Hewitson and Ian A Darby. *Histology protocols*. Springer, 2010.

[61] Andrew H Fischer, Kenneth A Jacobson, Jack Rose, and Rolf Zeller. Hematoxylin and eosin staining of tissue and cell sections. *Cold Spring Harbor Protocols*, 2008(5):pdb–prot4986, 2008.

[62] Travis L Shiba, Jordan Hardy, Georg Luegmair, Zhaoyan Zhang, and Jennifer L Long. Tissue-engineered vocal fold mucosa implantation in rabbits. *Otolaryngology–Head and Neck Surgery*, 154(4):679–688, 2016.

[63] Bengt Svensson, R Srinivasa Nagubothu, Jessica Cedervall, Katarina Le Blanc, Lars Ährlund-Richter, Anna Tolf, and Stellan Hertegård. Injection of human mesenchymal stem cells improves healing of scarred vocal folds: analysis using a xenograft model. *The Laryngoscope*, 120(7):1370–1375, 2010.

[64] Guillaume De Bonnecaze, Benoit Chaput, Virginie Woisard, Emmanuelle Uro-Coste, Pascal Swider, Sebastien Vergez, Elie Serrano, Louis Casteilla, and Valerie Planat-Benard. Adipose stromal cells improve healing of vocal fold scar: Morphological and functional evidences. *The Laryngoscope*, 126(8):E278–E285, 2016.

[65] Ryan C Branski, Katherine Verdolini, Clark A Rosen, and Patricia A Hebda. Acute vocal fold wound healing in a rabbit model. *Annals of Otology, Rhinology & Laryngology*, 114(1):19–24, 2005.

[66] Rebecca CK Maunsell, Leandro L de Freitas, Albina Altemani, and Agrício N Crespo. Histologic comparison of vocal fold microflap healing with sutures and glue. *The Laryngoscope*, 123(7):1709–1716, 2013.

[67] Andréa M Campagnolo, Domingos Hiroshi Tsuji, Luiz Ubirajara Sennes, Rui Imamura, and Paulo HN Saldiva. Histologic study of acute vocal fold wound healing after corticosteroid injection in a rabbit model. *Annals of Otology, Rhinology & Laryngology*, 119(2):133–139, 2010.

[68] JA Ramos-Vara. Technical aspects of immunohistochemistry. *Veterinary pathology*, 42(4):405–426, 2005.

[69] Susan L Thibeault, Bernard Rousseau, Nathan V Welham, Shigeru Hirano, and Diane M Bless. Hyaluronan levels in acute vocal fold scar. *The Laryngoscope*, 114(4):760–764, 2004.

[70] Jonas Albers, S Pacilé, M Andrea Markus, M Wiart, G Vande Velde, G Tromba, and Christian Dullin. X-ray-based 3d virtual histology—adding the next dimension to histological analysis. *Molecular Imaging and Biology*, pages 1–10, 2018.

[71] Christian Dullin, Roser Ufartes, Emanuel Larsson, Sabine Martin, Marcio Lazzarini, Giuliana Tromba, Jeannine Missbach-Guentner, Diana Pinkert-Leetsch, Dörthe M Katschinski, and Frauke Alves. μct of ex-vivo stained mouse hearts and embryos enables a precise match between 3d virtual histology, classical histology and immunochemistry. *PloS one*, 12(2):e0170597, 2017.

[72] Jonas Albers, M Andrea Markus, Frauke Alves, and Christian Dullin. X-ray based virtual histology allows guided sectioning of heavy ion stained murine lungs for histological analysis. *Scientific reports*, 8(1):7712, 2018.

[73] Fuminari Tatsugami, Toru Higaki, Masao Kiguchi, So Tsushima, Akira Taniguchi, Yoko Kaichi, Takuji Yamagami, and Kazuo Awai. Measurement of electron density

and effective atomic number by dual-energy scan using a 320-detector computed tomography scanner with raw data-based analysis: a phantom study. *Journal of computer assisted tomography*, 38(6):824–827, 2014.

[74] Joel D Boerckel, Devon E Mason, Anna M McDermott, and Eben Alsberg. Microcomputed tomography: approaches and applications in bioengineering. *Stem cell research & therapy*, 5(6):144, 2014.

[75] Anton Du Plessis, Chris Broeckhoven, Anina Guelpa, and Stephan Gerhard Le Roux. Laboratory x-ray micro-computed tomography: a user guideline for biological samples. *GigaScience*, 6(6):gix027, 2017.

[76] H Labriet, C Nemoz, M Renier, P Berkvens, T Brochard, R Cassagne, H Elleaume, F Estève, C Verry, J Balosso, et al. Significant dose reduction using synchrotron radiation computed tomography: first clinical case and application to high resolution ct exams. *Scientific reports*, 8(1):12491, 2018.

[77] Ryuta Mizutani and Yoshio Suzuki. X-ray microtomography in biology. *Micron*, 43(2-3):104–115, 2012.

[78] Tom Shearer, Robert S Bradley, L Araida Hidalgo-Bastida, Michael J Sherratt, and Sarah H Cartmell. Three-dimensional visualisation of soft biological structures by x-ray computed micro-tomography. *J Cell Sci*, 129(13):2483–2492, 2016.

[79] Nicolau Beckmann, Igor A Kaltashov, and Albert D Windhorst. In vivo imaging in pharmacological research. *Frontiers in pharmacology*, 7:511, 2017.

[80] Jeffrey R Ashton, Jennifer L West, and Cristian T Badea. In vivo small animal micro-ct using nanoparticle contrast agents. *Frontiers in pharmacology*, 6:256, 2015.

[81] Inger Havsteen, Anders Ohlhues, Kristoffer H Madsen, Janus Damm Nybing, Hanne Christensen, and Anders Christensen. Are movement artifacts in magnetic resonance imaging a real problem?—a narrative review. *Frontiers in neurology*, 8:232, 2017.

[82] Marcelo Saldias, Marco Guzman, Gonzalo Miranda, and Anne-Maria Laukkanen. A computerized tomography study of vocal tract setting in hyperfunctional dysphonia and in belting. *Journal of Voice*, 2018.

[83] F Unteregger, P Wagner, F Honegger, S Potthast, S Zwicky, and C Storck. Changes in vocal fold morphology during singing over two octaves. *Journal of Voice*, 2018.

[84] Thomas Rodt, Christian von Falck, Sabine Dettmer, Roman Halter, Regina Maus, Kjetil Ask, Martin Kolb, Jack Gauldie, Florian Länger, Ludwig Hoy, et al. Micro-computed tomography of pulmonary fibrosis in mice induced by adenoviral gene transfer of biologically active transforming growth factor-β1. *Respiratory research*, 11(1):181, 2010.

[85] Ibrahim Fatih Cengiz, Joaquim Miguel Oliveira, and Rui L Reis. Micro-ct–a digital 3d microstructural voyage into scaffolds: a systematic review of the reported methods and results. *Biomaterials research*, 22(1):26, 2018.

[86] Frank Neues and Matthias Epple. X-ray microcomputer tomography for the study of biomineralized endo-and exoskeletons of animals. *Chemical Reviews*, 108(11):4734–4741, 2008.

[87] P Joy Dunmore-Buyze, Elsbeth Tate, Fu-li Xiang, Sarah A Detombe, Zengxuan Nong, J Geoffrey Pickering, and Maria Drangova. Three-dimensional imaging of the mouse heart and vasculature using micro-ct and whole-body perfusion of iodine or phosphotungstic acid. *Contrast media & molecular imaging*, 9(5):383–390, 2014.

[88] Richard Balint, Tristan Lowe, and Tom Shearer. Optimal contrast agent staining of ligaments and tendons for x-ray computed tomography. *PloS one*, 11(4):e0153552, 2016.

[89] Brian D Metscher. Microct for developmental biology: A versatile tool for high-contrast 3d imaging at histological resolutions. *Developmental dynamics: an official publication of the American Association of Anatomists*, 238(3):632–640, 2009.

[90] Brian D Metscher. X-ray microtomographic imaging of intact vertebrate embryos. *Cold Spring Harbor Protocols*, 2011(12):pdb–prot067033, 2011.

[91] Brian D Metscher. Microct for comparative morphology: simple staining methods allow high-contrast 3d imaging of diverse non-mineralized animal tissues. *BMC physiology*, 9(1):11, 2009.

[92] Gordon L Paterson, Dan Sykes, Sarah Faulwetter, Reece Merk, Farah Ahmed, Lawrence E Hawkins, John Dinley, Alexander D Ball, and Christos Arvanitidis. The pros and cons of using micro-computed tomography in gross and micro-anatomical assessments of polychaetous annelids. *Mem Mus Victoria*, 71:237–46, 2014.

[93] H Schmidbaur, K Keklikoglou, BD Metscher, and S Faulwetter. Exploring methods to remove iodine and phosphotungstic acid stains from zoological specimens. *Bruker microCT User Mtg Abstracts*, 21:1–8, 2015.

[94] Ying Chen, Gufa Lin, Yungchung Chen, Alex Fok, and Jonathan MW Slack. Micro-computed tomography for visualizing limb skeletal regeneration in young xenopus frogs. *The Anatomical Record: Advances in Integrative Anatomy and Evolutionary Biology*, 295(10):1562–1565, 2012.

[95] Lucy A Walton, Robert S Bradley, Philip J Withers, Victoria L Newton, Rachel EB Watson, Clare Austin, and Michael J Sherratt. Morphological characterisation of unstained and intact tissue micro-architecture by x-ray computed micro-and nano-tomography. *Scientific reports*, 5:10074, 2015.

[96] Guang-Hong Chen, Joseph Zambelli, Nicholas Bevins, Zhihua Qi, and Ke Li. X-ray phase sensitive imaging methods: basic physical principles and potential medical applications. *Current medical imaging reviews*, 6(2):90–99, 2010.

[97] Lucie Bailly, Thibaud Cochereau, Laurent Orgéas, Nathalie Henrich Bernardoni, Sabine Rolland Du Roscoat, Anne McLeer-Florin, Yohann Robert, Xavier Laval, Tanguy Laurencin, Philippe Chaffanjon, et al. 3d multiscale imaging of human vocal folds using synchrotron x-ray microtomography in phase retrieval mode. *Scientific reports*, 8(1):14003, 2018.

[98] Zhi-Pei Liang and Paul C Lauterbur. *Principles of magnetic resonance imaging: a signal processing perspective*. SPIE Optical Engineering Press, 2000.

[99] Christopher M Collins. *Electromagnetics in magnetic resonance imaging: physical principles, related applications, and ongoing developments*. Morgan & Claypool Publishers, 2016.

[100] Thomas F Budinger and Mark D Bird. Mri and mrs of the human brain at magnetic fields of 14 t to 20 t: Technical feasibility, safety, and neuroscience horizons. *NeuroImage*, 168:509–531, 2018.

[101] Vadim Kuperman. *Magnetic resonance imaging: physical principles and applications*. Elsevier, 2000.

[102] Carolyn K Novaleski, Tsuyoshi Kojima, Siyuan Chang, Haoxiang Luo, Carla V Valenzuela, and Bernard Rousseau. Nonstimulated rabbit phonation model: Cricothyroid approximation. *The Laryngoscope*, 126(7):1589–1594, 2016.

[103] Victoria LM Herrera, Jason C Viereck, Gerardo Lopez-Guerra, Yoshihiko Kumai, James Kobler, Sandeep Karajanagi, Hyoungshin Park, Robert Hillman, and Steven M Zeitels. 11.7 tesla magnetic resonance microimaging of laryngeal tissue architecture. *The Laryngoscope*, 119(11):2187–2194, 2009.

[104] Ayami Ohno Kishimoto, Yo Kishimoto, David L Young, Jinjin Zhang, Ian J Rowland, and Nathan V Welham. High and ultrahigh-field magnetic resonance imaging of naïve, injured, and scarred vocal fold mucosae in rats. *Disease models & mechanisms*, pages dmm–026526, 2016.

[105] Juan Eugenio Iglesias, Shauna Crampsie, Catherine Strand, Mohamed Tachrount, David L Thomas, and Janice L Holton. Effect of fluorinert on the histological properties of formalin-fixed human brain tissue. *Journal of Neuropathology & Experimental Neurology*, 77(12):1085–1090, 2018.

[106] Steven Oleson, Kun-Han Lu, Zhongming Liu, Abigail C Durkes, and M Preeti Sivasankar. Proton density–weighted laryngeal magnetic resonance imaging in systemically dehydrated rats. *The Laryngoscope*, 128(6):E222–E227, 2018.

[107] Harald T Lutz. Basics of ultrasound. *Manual of Diagnostic Ultrasound in Infectious Tropical Diseases, Springer Science & Business Media, Newyork*, pages 1–19, 2006.

[108] Julina Ongkasuwan, Danielle Devore, Sarah Hollas, Jeremy Jones, and Brandon Tran. Laryngeal ultrasound and pediatric vocal fold nodules. *The Laryngoscope*, 127(3):676–678, 2017.

[109] Maheer M Masood, Benjamin Huang, Allie Goins, and Trevor G Hackman. Anatomic factors affecting the use of ultrasound to predict vocal fold motion: A pilot study. *American journal of otolaryngology*, 39(4):413–417, 2018.

[110] Marek Dedecjus, Zbigniew Adamczewski, Jan Brzeziński, and Andrzej Lewiński. Real-time, high-resolution ultrasonography of the vocal folds—a prospective pilot study in patients before and after thyroidectomy. *Langenbeck's archives of surgery*, 395(7):859–864, 2010.

[111] Javier Adur, Hernandes F Carvalho, Carlos L Cesar, and Víctor H Casco. Nonlinear microscopy techniques: principles and biomedical applications. In *Microscopy and Analysis*. InTech, 2016.

[112] Brian Herman. Fluorescence microscopy. *Current protocols in cell biology*, (1):4–2, 1998.

[113] Michael J Sanderson, Ian Smith, Ian Parker, and Martin D Bootman. Fluorescence microscopy. *Cold Spring Harbor Protocols*, 2014(10):pdb–top071795, 2014.

[114] Richard KP Benninger and David W Piston. Two-photon excitation microscopy for the study of living cells and tissues. *Current protocols in cell biology*, 59(1):4–11, 2013.

[115] Thai V Truong, Willy Supatto, David S Koos, John M Choi, and Scott E Fraser. Deep and fast live imaging with two-photon scanned light-sheet microscopy. *Nature methods*, 8(9):757, 2011.

[116] Paul Campagnola. Second harmonic generation imaging microscopy: applications to diseases diagnostics, 2011.

[117] Markus Rehberg, Fritz Krombach, Ulrich Pohl, and Steffen Dietzel. Signal improvement in multiphoton microscopy by reflection with simple mirrors near the sample. *Journal of biomedical optics*, 15(2):026017, 2010.

[118] R Gauderon, PB Lukins, and CJR Sheppard. Simultaneous multichannel nonlinear imaging: combined two-photon excited fluorescence and second-harmonic generation microscopy. *Micron*, 32(7):685–689, 2001.

[119] Chi Zhang, Delong Zhang, and Ji-Xin Cheng. Coherent raman scattering microscopy in biology and medicine. *Annual review of biomedical engineering*, 17:415–445, 2015.

[120] Adam M Hanninen, Richard C Prince, Raul Ramos, Maksim V Plikus, and Eric O Potma. High-resolution infrared imaging of biological samples with third-order sum-frequency generation microscopy. *Biomedical optics express*, 9(10):4807–4817, 2018.

[121] Mathias Strupler, Romain Deterre, Nadir Goulamhoussen, Fouzi Benboujja, Christopher J Hartnick, and Caroline Boudoux. Nonlinear microscopy of the vocal folds. In *Biomedical Optics in Otorhinolaryngology*, pages 511–528. Springer, 2016.

[122] Erin E. Devine, Yuming Liu, Adib Keikhosravi, Kevin W. Elicieri, and Jack J. Jiang. Quantitative second harmonic generation imaging of leporine, canine, and porcine vocal fold collagen. *The Laryngoscope*, 00(2019):1–8, Jan 2019.

[123] Junichi Kaneshiro, Yasushi Okada, Tomohiro Shima, Mika Tsujii, Katsumi Imada, Taro Ichimura, and Tomonobu M Watanabe. Second harmonic generation polarization microscopy as a tool for protein structure analysis. *bioRxiv*, page 338137, 2018.

[124] Douglas S Richardson and Jeff W Lichtman. Clarifying tissue clearing. *Cell*, 162(2):246–257, 2015.

[125] Etsuo A Susaki, Kazuki Tainaka, Dimitri Perrin, Hiroko Yukinaga, Akihiro Kuno, and Hiroki R Ueda. Advanced cubic protocols for whole-brain and whole-body clearing and imaging. *Nature protocols*, 10(11):1709, 2015.

[126] Tingting Yu, Yisong Qi, Jingtan Zhu, Jianyi Xu, Hui Gong, Qingming Luo, and Dan Zhu. Elevated-temperature-induced acceleration of pact clearing process of mouse brain tissue. *Scientific reports*, 7:38848, 2017.

[127] Chenchen Pan, Ruiyao Cai, Francesca Paola Quacquarelli, Alireza Ghasemigharagoz, Athanasios Lourbopoulos, Paweł Matryba, Nikolaus Plesnila, Martin Dichgans, Farida Hellal, and Ali Ertürk. Shrinkage-mediated imaging of entire organs and organisms using udisco. *Nature methods*, 13(10):859–867, 2016.

[128] Yisong Qi, Tingting Yu, Jianyi Xu, Peng Wan, Yilin Ma, Jingtan Zhu, Yusha Li, Hui Gong, Qingming Luo, and Dan Zhu. Fdisco: Advanced solvent-based clearing method for imaging whole organs. *Science Advances*, 5(1):eaau8355, 2019.

[129] Shuguang Guo, River L Hutchison, Ryan Patrick Jackson, Anu Kohli, Tristan Sharp, Elizabeth Orwin, Richard Campbell Haskell, Zhongping Chen, and Brian Jet-Fei Wong. Office-based optical coherence tomographic imaging of human vocal cords. *Journal of biomedical optics*, 11(3):030501, 2006.

[130] James A Burns, Ki Hean Kim, James B Kobler, Johannes F deBoer, Gerardo Lopez-Guerra, and Steven M Zeitels. Real-time tracking of vocal fold injections with optical coherence tomography. *The Laryngoscope*, 119(11):2182–2186, 2009.

[131] Fouzi Benboujja and Christopher Hartnick. Clinical and surgical implications of intra-operative optical coherence tomography imaging for benign pediatric vocal fold lesions. *International journal of pediatric otorhinolaryngology*, 114:111–119, 2018.

[132] James A Burns. Optical coherence tomography: imaging the larynx. *Current opinion in otolaryngology & head and neck surgery*, 20(6):477–481, 2012.

[133] Anahita Nourmahnad, Fouzi Benboujja, and Christopher J Hartnick. Intraoperative imaging of pediatric unilateral vocal fold paralysis using optical coherence tomography. *International Journal of Pediatric Otorhinolaryngology*, 2019.

[134] Ki Hean Kim, James A Burns, Jonathan J Bernstein, Gopi N Maguluri, B Hyle Park, and Johannes F de Boer. In vivo 3d human vocal fold imaging with polarization sensitive optical coherence tomography and a mems scanning catheter. *Optics express*, 18(14):14644–14653, 2010.

[135] David R Rivera, Christopher M Brown, Dimitre G Ouzounov, Ina Pavlova, Demirhan Kobat, Watt W Webb, and Chris Xu. Compact and flexible raster scanning multiphoton endoscope capable of imaging unstained tissue. *Proceedings of the National Academy of Sciences*, 2011.

[136] Guillaume Ducourthial, Pierre Leclerc, Tigran Mansuryan, Marc Fabert, Julien Brevier, Rémi Habert, Flavie Braud, Renaud Batrin, Christine Vever-Bizet, Geneviève Bourg-Heckly, et al. Development of a real-time flexible multiphoton microendoscope for label-free imaging in a live animal. *Scientific reports*, 5:18303, 2015.

[137] Lin Huang. *Miniature multiphoton endoscopy using frequency-doubled Er-doped fiber laser*. PhD thesis, University of British Columbia, 2018.

[138] Lisa Gottesfeld Brown. A survey of image registration techniques. *ACM computing surveys (CSUR)*, 24(4):325–376, 1992.

[139] J Michael Fitzpatrick, Derek LG Hill, Calvin R Maurer, et al. Image registration. *Handbook of medical imaging*, 2:447–513, 2000.

[140] Frederik Maes, Dirk Loeckx, Dirk Vandermeulen, and Paul Suetens. Image registration using mutual information. In *Handbook of Biomedical Imaging*, pages 295–308. Springer, 2015.

[141] Graeme P Penney, Jürgen Weese, John A Little, Paul Desmedt, Derek LG Hill, et al. A comparison of similarity measures for use in 2-d-3-d medical image registration. *IEEE transactions on medical imaging*, 17(4):586–595, 1998.

[142] Alex Pappachen James and Belur V Dasarathy. Medical image fusion: A survey of the state of the art. *Information Fusion*, 19:4–19, 2014.

[143] Hani Bakhshaee, Christina Moro, Karen Kost, and Luc Mongeau. Three-dimensional reconstruction of human vocal folds and standard laryngeal cartilages using computed tomography scan data. *Journal of Voice*, 27(6):769–777, 2013.

[144] Ivo Klepacek, Daniel Jirak, Miroslava Duskova Smrckova, Olga Janouskova, and Tomas Vampola. The human vocal fold layers. their delineation inside vocal fold as a background to create 3d digital and synthetic glottal model. *Journal of Voice*, 30(5):529–537, 2016.

[145] Kiminori Sato. *Functional Histoanatomy of the Human Larynx*. Springer, 2018.

[146] Paul A Yushkevich, Joseph Piven, Heather Cody Hazlett, Rachel Gimpel Smith, Sean Ho, James C Gee, and Guido Gerig. User-guided 3d active contour segmentation of anatomical structures: significantly improved efficiency and reliability. *Neuroimage*, 31(3):1116–1128, 2006.

[147] Steve Pieper, Michael Halle, and Ron Kikinis. 3d slicer. In *2004 2nd IEEE international symposium on biomedical imaging: nano to macro (IEEE Cat No. 04EX821)*, pages 632–635. IEEE, 2004.

[148] Yann LeCun, Yoshua Bengio, and Geoffrey Hinton. Deep learning. *nature*, 521(7553):436, 2015.

[149] Ladislav Rampasek and Anna Goldenberg. Tensorflow: Biology's gateway to deep learning? *Cell systems*, 2(1):12–14, 2016.

[150] Martín Abadi, Paul Barham, Jianmin Chen, Zhifeng Chen, Andy Davis, Jeffrey Dean, Matthieu Devin, Sanjay Ghemawat, Geoffrey Irving, Michael Isard, et al. Tensorflow: A system for large-scale machine learning. In *12th {USENIX} Symposium on Operating Systems Design and Implementation ({OSDI} 16)*, pages 265–283, 2016.

[151] Özgün Çiçek, Ahmed Abdulkadir, Soeren S Lienkamp, Thomas Brox, and Olaf Ronneberger. 3d u-net: learning dense volumetric segmentation from sparse annotation. In *International Conference on Medical Image Computing and Computer-Assisted Intervention*, pages 424–432. Springer, 2016.

[152] Chet C Xu, Ang Gao, and Song Zhang. An investigation of left–right vocal fold symmetry in rheological and histological properties. *The Laryngoscope*, 2018.

[153] M Kürşat Gökcan, D Funda Kurtuluş, Evren Üstüner, Elif Özyürek, G Gökçen Kesici, S Ceyhan Erdem, Gürsel Dursun, and Cemil Yağci. A computational study on the characteristics of airflow in bilateral abductor vocal fold immobility. *The Laryngoscope*, 120(9):1808–1818, 2010.

[154] Weili Jiang, Xudong Zheng, and Qian Xue. computational modeling of fluid–structure–acoustics interaction during voice production. *Frontiers in bioengineering and biotechnology*, 5:7, 2017.

[155] Cheng Zhong, Hai-Yang Xie, Lin Zhou, Xiao Xu, and Shu-Sen Zheng. Human hepatocytes loaded in 3d bioprinting generate mini-liver. *Hepatobiliary & Pancreatic Diseases International*, 15(5):512–518, 2016.

[156] Andrew Squelch. 3d printing and medical imaging. *Journal of medical radiation sciences*, 65(3):171–172, 2018.

[157] Nongping Zhong and Xia Zhao. 3d printing for clinical application in otorhinolaryngology. *European Archives of Oto-Rhino-Laryngology*, 274(12):4079–4089, 2017.

[158] W Eric L Grimson, RJFA Kikinis, Ferenc A Jolesz, and PM Black. Image-guided surgery. *Scientific American*, 280(6):54–61, 1999.

[159] Fabian Rengier, Amit Mehndiratta, Hendrik Von Tengg-Kobligk, Christian M Zechmann, Roland Unterhinninghofen, H-U Kauczor, and Frederik L Giesel. 3d printing based on imaging data: review of medical applications. *International journal of computer assisted radiology and surgery*, 5(4):335–341, 2010.

[160] Murat Yildirim, Kyle P Quinn, James B Kobler, Steven M Zeitels, Irene Georgakoudi, and Adela Ben-Yakar. Quantitative differentiation of normal and scarred tissues using second-harmonic generation microscopy. *Scanning*, 38(6):684–693, 2016.

[161] Nick Merna, Claire Robertson, Anh La, and Steven C George. Optical imaging predicts mechanical properties during decellularization of cardiac tissue. *Tissue Engineering Part C: Methods*, 19(10):802–809, 2013.

[162] Niles O Petersen, Pia L Höddelius, Paul W Wiseman, Olle Seger, and KE Magnusson. Quantitation of membrane receptor distributions by image correlation spectroscopy: concept and application. *Biophysical journal*, 65(3):1135–1146, 1993.

[163] Paul W Wiseman. Image correlation spectroscopy: principles and applications. *Cold Spring Harbor Protocols*, 2015(4):pdb–top086124, 2015.

[164] Rik Paesen, Kathleen Sanen, Nick Smisdom, Luc Michiels, and Marcel Ameloot. Polarization second harmonic generation by image correlation spectroscopy on collagen type i hydrogels. *Acta biomaterialia*, 10(5):2036–2042, 2014.

[165] Sadiq Mohammed Mir, Brenda Baggett, and Urs Utzinger. The efficacy of image correlation spectroscopy for characterization of the extracellular matrix. *Biomedical optics express*, 3(2):215–224, 2012.

[166] Christopher B Raub, Jay Unruh, Vinod Suresh, Tatiana Krasieva, Tore Lindmo, Enrico Gratton, Bruce J Tromberg, and Steven C George. Image correlation spectroscopy of multiphoton images correlates with collagen mechanical properties. *Biophysical journal*, 94(6):2361–2373, 2008.

[167] Claire Robertson and Steven C George. Theory and practical recommendations for autocorrelation-based image correlation spectroscopy. *Journal of biomedical optics*, 17(8):080801, 2012.

[168] Kathleen Sanen, Rik Paesen, Sander Luyck, James Phillips, Ivo Lambrichts, Wendy Martens, and Marcel Ameloot. Label-free mapping of microstructural organisation

in self-aligning cellular collagen hydrogels using image correlation spectroscopy. *Acta biomaterialia*, 30:258–264, 2016.

[169] Raghu Ambekar Ramachandra Rao, Monal R Mehta, and Kimani C Toussaint. Fourier transform-second-harmonic generation imaging of biological tissues. *Optics express*, 17(17):14534–14542, 2009.

[170] Paolo Matteini, Fulvio Ratto, Francesca Rossi, Riccardo Cicchi, Chiara Stringari, Dimitrios Kapsokalyvas, Francesco S Pavone, and Roberto Pini. Photothermally-induced disordered patterns of corneal collagen revealed by shg imaging. *Optics express*, 17(6):4868–4878, 2009.

[171] Jeremy S Bredfeldt, Yuming Liu, Carolyn A Pehlke, Matthew W Conklin, Joseph M Szulczewski, David R Inman, Patricia J Keely, Robert D Nowak, Thomas R Mackie, and Kevin W Eliceiri. Computational segmentation of collagen fibers from second-harmonic generation images of breast cancer. *Journal of biomedical optics*, 19(1):016007, 2014.

[172] Yuming Liu, Adib Keikhosravi, Guneet S Mehta, Cole R Drifka, and Kevin W Eliceiri. Methods for quantifying fibrillar collagen alignment. In *Fibrosis*, pages 429–451. Springer, 2017.

[173] Jean-Luc Starck, Emmanuel J Candès, and David L Donoho. The curvelet transform for image denoising. *IEEE Transactions on image processing*, 11(6):670–684, 2002.

[174] Shi-Wei Chu, Shih-Peng Tai, Ming-Che Chan, Chi-Kuang Sun, I-Ching Hsiao, Chi-Hung Lin, Yung-Chih Chen, and Bai-Ling Lin. Thickness dependence of optical second harmonic generation in collagen fibrils. *Optics express*, 15(19):12005–12010, 2007.

[175] Marie-Andrée Houle, Charles-André Couture, Stéphane Bancelin, Jarno Van der Kolk, Etienne Auger, Cameron Brown, Konstantin Popov, Lora Ramunno, and François Légaré. Analysis of forward and backward second harmonic generation images to probe the nanoscale structure of collagen within bone and cartilage. *Journal of biophotonics*, 8(11-12):993–1001, 2015.

[176] Klaus-D Wolff, Marco Kesting, Thomas Mücke, Andrea Rau, and Frank Hölzle. Thiel embalming technique: a valuable method for microvascular exercise and teaching of flap raising. *Microsurgery: Official Journal of the International Microsurgical Society and the European Federation of Societies for Microsurgery*, 28(4):273–278, 2008.

[177] Desmond PJ Barton, D Ceri Davies, Vishy Mahadevan, Lee Dennis, Tania Adib, Satvinder Mudan, Aslam Sohaib, and Harold Ellis. Dissection of soft-preserved cadavers in the training of gynaecological oncologists: report of the first uk workshop. *Gynecologic oncology*, 113(3):352–356, 2009.

[178] Johannes Schindelin, Ignacio Arganda-Carreras, Erwin Frise, Verena Kaynig, Mark Longair, Tobias Pietzsch, Stephan Preibisch, Curtis Rueden, Stephan Saalfeld, Benjamin Schmid, et al. Fiji: an open-source platform for biological-image analysis. *Nature methods*, 9(7):676, 2012.

[179] Curtis T Rueden, Johannes Schindelin, Mark C Hiner, Barry E DeZonia, Alison E Walter, Ellen T Arena, and Kevin W Eliceiri. Imagej2: Imagej for the next generation of scientific image data. *BMC bioinformatics*, 18(1):529, 2017.

[180] Lorenzo F Ochoa, Alexander Kholodnykh, Paula Villarreal, Bing Tian, Rahul Pal, Alexander N Freiberg, Allan R Brasier, Massoud Motamedi, and Gracie Vargas. Imaging of murine whole lung fibrosis by large scale 3d microscopy aided by tissue optical clearing. *Scientific reports*, 8(1):13348, 2018.

[181] Claire Robertson, Kenji Ikemura, Tatiana B Krasieva, and Steven C George. Multiscale analysis of collagen microstructure with generalized image correlation spectroscopy and the detection of tissue prestress. *Biomaterials*, 34(26):6127–6132, 2013.

[182] Mikhail V Svistushkin, Svetlana L Kotova, Anatoly B Shekhter, Valery M Svistushkin, Anastasia A Akovantseva, Anastasia A Frolova, Alexey L Fayzullin, Svetlana V Starostina, Evgeny A Bezrukov, Roman B Sukhanov, et al. Collagen fibrillar structures in vocal fold scarring and repair using stem cell therapy: a detailed histological, immunohistochemical and atomic force microscopy study. *Journal of microscopy*, 2019.

[183] Shigeru Hirano, Susan Thibeault, Charles N Ford, Diane M Bless, and Shin-Ichi Kanemaru. Hepatocyte growth factor and its receptor c-met in rat and rabbit vocal folds. *Annals of Otology, Rhinology & Laryngology*, 111(8):661–666, 2002.

[184] Susan L Thibeault, Patrick J VanGroll, Kevin J Kriesel, Roger W Chan, Diane M Bless, Tatsutoshi Suzuki, and Charles N Ford. Treatment of vocal fold scarring: rheological and histological measures of homologous collagen matrix. *Annals of Otology, Rhinology & Laryngology*, 111(10):884–889, 2002.

[185] Susan L Thibeault, Diane M Bless, and Steven D Gray. Interstitial protein alterations in rabbit vocal fold with scar. *Journal of Voice*, 17(3):377–383, 2003.

[186] Bernard Rousseau, Shigeru Hirano, Roger W Chan, Nathan V Welham, Susan L Thibeault, Charles N Ford, and Diane M Bless. Characterization of chronic vocal fold scarring in a rabbit model. *Journal of Voice*, 18(1):116–124, 2004.

[187] Shigeru Hirano, Diane M Bless, Bernard Rousseau, Nathan Welham, Douglas Montequin, Roger W Chan, and Charles N Ford. Prevention of vocal fold scarring by topical injection of hepatocyte growth factor in a rabbit model. *The Laryngoscope*, 114(3):548–556, 2004.

[188] Ryan C Branski, Clark A Rosen, Katherine Verdolini, and Patricia A Hebda. Biochemical markers associated with acute vocal fold wound healing: a rabbit model. *Journal of Voice*, 19(2):283–289, 2005.

[189] Jennifer K Hansen, Susan L Thibeault, Jennifer F Walsh, Xiao Zheng Shu, and Glenn D Prestwich. In vivo engineering of the vocal fold extracellular matrix with injectable hyaluronic acid hydrogels: early effects on tissue repair and biomechanics in a rabbit model. *Annals of Otology, Rhinology & Laryngology*, 114(9):662–670, 2005.

[190] Suzy Duflo, Susan L Thibeault, Wenhua Li, Xiao Zheng Shu, and Glenn Prestwich. Effect of a synthetic extracellular matrix on vocal fold lamina propria gene expression in early wound healing. *Tissue engineering*, 12(11):3201–3207, 2006.

[191] Suzy Duflo, Susan L Thibeault, Wenhua Li, Xiao Zheng Shu, and Glenn D Prestwich. Vocal fold tissue repair in vivo using a synthetic extracellular matrix. *Tissue engineering*, 12(8):2171–2180, 2006.

[192] Jessica Cedervall, Lars Ährlund-Richter, Bengt Svensson, Kristina Forsgren, Franz HJ Maurer, Daniela Vidovska, and Stellan Hertegård. Injection of embryonic stem cells into scarred rabbit vocal folds enhances healing and improves viscoelasticity: short-term results. *The Laryngoscope*, 117(11):2075–2081, 2007.

[193] Bernard Rousseau, Ping Jiang Ge, Tsunehisa Ohno, Lesley C French, and Susan L Thibeault. Extracellular matrix gene expression after vocal fold injury in a rabbit model. *Annals of Otology, Rhinology & Laryngology*, 117(8):598–603, 2008.

[194] Susan L Thibeault and Suzy Duflo. Inflammatory cytokine responses to synthetic extracellular matrix injection to the vocal fold lamina propria. *Annals of Otology, Rhinology & Laryngology*, 117(3):221–226, 2008.

[195] Susan L Thibeault, Sarah A Klemuk, Marshall E Smith, Cecilia Leugers, and Glenn Prestwich. In vivo comparison of biomimetic approaches for tissue regeneration of the scarred vocal fold. *Tissue Engineering Part A*, 15(7):1481–1487, 2008.

[196] Ozgur Akdogan, Adin Selcuk, Ibrahim Ozcan, Kürsat Murat Ozcan, Seren Gulsen Giray, Huseyin Dere, and Candan Ozogul. Activation of vocal fold healing with topical vitamin a in rabbits. *Acta oto-laryngologica*, 129(2):220–224, 2009.

[197] S Hertegård, J Cedervall, B Svensson, K Forsberg, F HJ Maurer, Daniela Vidovska, Petri Olivius, L Ährlund-Richter, and K Le Blanc. Viscoelastic and histologic properties in scarred rabbit vocal folds after mesenchymal stem cell injection. *The Laryngoscope*, 116(7):1248–1254, 2009.

[198] Susan L Thibeault, Sarah A Klemuk, Xia Chen, and Beatriz H Quinchia Johnson. In vivo engineering of the vocal fold ecm with injectable ha hydrogels—late effects on tissue repair and biomechanics in a rabbit model. *Journal of Voice*, 25(2):249–253, 2011.

[199] Atsushi Suehiro, Jonathan M Bock, Joseph E Hall, C Gaelyn Garrett, and Bernard Rousseau. Feasibility and acute healing of vocal fold microflap incisions in a rabbit model. *The Laryngoscope*, 122(3):600–605, 2012.

[200] Young-Mo Kim, TacGhee Yi, Jeong-Seok Choi, Songyi Lee, Yun Ho Jang, Chul-Ho Kim, Sun U Song, and Jae-Yol Lim. Bone marrow-derived clonal mesenchymal stem cells as a source of cell therapy for promoting vocal fold wound healing. *Annals of Otology, Rhinology & Laryngology*, 122(2):121–130, 2013.

[201] Jae Won Choi, Ju Kyeong Park, Jae Won Chang, Moon Suk Kim, Yoo Seob Shin, Chul-Ho Kim, et al. Small intestine submucosa and mesenchymal stem cells composite gel for scarless vocal fold regeneration. *Biomaterials*, 35(18):4911–4918, 2014.

[202] Ted Mau, Mindy Du, and Chet C Xu. A rabbit vocal fold laser scarring model for testing lamina propria tissue-engineering therapies. *The Laryngoscope*, 124(10):2321–2326, 2014.

[203] Bengt Svensson, Srinivasa R Nagubothu, Christoffer Nord, Jessica Cedervall, Isabell Hultman, Lars Ährlund-Richter, Anna Tolf, and Stellan Hertegård. Stem cell therapy in injured vocal folds: a three-month xenograft analysis of human embryonic stem cells. *BioMed Research International*, 2015, 2015.

[204] Michael J Pitman, Takashi Kurita, Maria E Powell, Emily E Kimball, Masanobu Mizuta, Siyuan Chang, C Gaelyn Garrett, and Bernard Rousseau. Vibratory function and healing outcomes after small intestinal submucosa biomaterial implantation for chronic vocal fold scar. *The Laryngoscope*, 128(4):901–908, 2018.

[205] Helena Hotz Arroyo-Ramos, Larissa Neri, Marilia Wellichan Mancini, Amaro Nunes Duarte Neto, Thais Mauad, and Rui Imamura. Effects of diode laser setting for laryngeal surgery in a rabbit model. *European Archives of Oto-Rhino-Laryngology*, pages 1–8, 2019.

[206] Renee E King, Hang Kuen Lau, Haiyan Zhang, Ishnoor Sidhu, Michael B Christensen, Eric W Fowler, Linqing Li, Xinqiao Jia, Kristi L Kiick, and Susan L Thibeault. Biocompatibility and viscoelastic properties of injectable resilin-like polypeptide and hyaluronan hybrid hydrogels in rabbit vocal folds. *Regenerative Engineering and Translational Medicine*, pages 1–14, 2019.

[207] Srinivasa Rao Nagubothu, Rachael V Sugars, Nikolce Tudzarovski, Anton Törnqvist Andrén, Matteo Bottai, Lindsay C Davies, Stellan Hertegård, and Katarina Le Blanc. Mesenchymal stromal cells modulate tissue repair responses within the injured vocal fold. *The Laryngoscope*, 2019.

[208] Hossein K Heris, Amir K Miri, Nageswara R Ghattamaneni, Nicole YK Li, Susan L Thibeault, Paul W Wiseman, and Luc Mongeau. Microstructural and mechanical characterization of scarred vocal folds. *Journal of biomechanics*, 48(4):708–711, 2015.

[209] Klaus Becker, Nina Jährling, Saiedeh Saghafi, Reto Weiler, and Hans-Ulrich Dodt. Chemical clearing and dehydration of gfp expressing mouse brains. *PloS one*, 7(3):e33916, 2012.

[210] Zainab Farzal, Elizabeth D Stephenson, Lauren A Kilpatrick, Brent A Senior, and Adam M Zanation. Sex bias: Is it pervasive in otolaryngology clinical research? *The Laryngoscope*, 2018.

[211] Shivangi Kelkar, Carol J Boushey, and Martin Okos. A method to determine the density of foods using x-ray imaging. *Journal of food engineering*, 159:36–41, 2015.

[212] BJ Heismann, J Leppert, and K Stierstorfer. Density and atomic number measurements with spectral x-ray attenuation method. *Journal of applied physics*, 94(3):2073–2079, 2003.

[213] Regine Gradl, Irene Zanette, Maite Ruiz-Yaniz, Martin Dierolf, Alexander Rack, Paul Zaslansky, and Franz Pfeiffer. Mass density measurement of mineralized tissue with grating-based x-ray phase tomography. *PloS one*, 11(12):e0167797, 2016.

[214] S Handschuh, CJ Beisser, B Ruthensteiner, and BD Metscher. Microscopic dual-energy ct (microdect): a flexible tool for multichannel ex vivo 3d imaging of biological specimens. *Journal of microscopy*, 267(1):3–26, 2017.

[215] Fei Chen, Paul W Tillberg, and Edward S Boyden. Expansion microscopy. *Science*, 347(6221):543–548, 2015.

[216] Martin J Booth. Adaptive optical microscopy: the ongoing quest for a perfect image. *Light: Science & Applications*, 3(4):e165, 2014.